Feasibility study of three-dimensional patient-specific simulation of glenohumeral range of motion.

Auteur : Dirick, Thomas
Promoteur(s) : Schwartz, Cédric
Faculté : Faculté des Sciences appliquées
Diplôme : Master en ingénieur civil biomédical, à finalité spécialisée
Année académique : 2024-2025
URI/URL : http://hdl.handle.net/2268.2/23345

UNIVERSITE DE LIEGE
FACULTE DES SCIENCES APPLIQUEES

Feasibility study of three-dimensional patient-specific simulation of glenohumeral range of motion.

Dirick Thomas

Thesis presented to obtain the degree of :
Master of Science in Biomedical Engineering

Thesis supervisors :
VAN CLEYNENBREUGEL Tim (Replasia)
MEYNEN Alexander (Replasia)
SCHWARTZ Cédric (ULiege)

Academic year: **2024 - 2025**

Acknowledgments

I would first like to thank Alexander Meynen, my daily supervisor at Replasia, for his constant help, technical guidance, and availability throughout the entire project. His support played a key role in every stage of this thesis.

I also thank Tim Van Cleynenbreugel for offering me the opportunity to work on this subject and for his valuable input and direction during the project.

I am sincerely grateful to Prof. Cédric Schwartz, my academic supervisor, for agreeing to supervise this thesis despite it falling outside his usual research topics and involving a new collaboration with Replasia. His trust, openness, and feedback were greatly appreciated.

I also wish to thank the members of the jury, Prof. Davide Ruffoni and Prof. Olivier Bruls, for their time and for evaluating my work.

Finally, I thank my friends and family for their encouragement and support during the more intense phases of this journey.

Abstract

Shoulder instability is a common clinical problem, especially in patients with bone defects like Hill-Sachs or bony Bankart lesions. Today, most preoperative tools are made for shoulder replacements and do not help evaluate joint stability in patients who need bone-preserving surgeries. This thesis aims to fill that gap by developing a patient-specific simulation tool that estimates the range of motion (ROM) of the glenohumeral joint using 3D computed tomography (CT) scans of the scapula and humerus.

The main goal is to identify which joint configurations are stable and which are not, using a set of anatomical constraints. The simulation works in two steps: first, it samples possible positions in a wide area, and then it uses a binary search to refine the boundaries of the valid space. Several constraints are used to evaluate each position, including bone collision, glenoid coverage, distances between bones, and tuberosity orientation.

The method was tested on five different patients. Results showed that bone defects, especially glenoid bone loss, reduced the amount of valid movement. Among the constraints, glenoid coverage was the most common reason for rejecting a joint position, followed by acromiohumeral and coracohumeral distances.

Finally, a clinical application is presented to evaluate whether Hill-Sachs lesions engage within the computed range of motion. The results indicate that the risk of engagement depends more on the location of the defect than on its size. Notably, some engagements were observed even in near-neutral arm positions, not only at the boundaries of the ROM.

In conclusion, this feasibility study presents an approach for simulating glenohumeral motion using patient-specific CT data. While the tool provides an initial framework for exploring joint stability, its current limitations prevent clinical application. Further work is required to determine whether these limitations can be overcome in future developments.

Contents

List of Figures

List of Tables

Acronyms

AA	angulus acromialis.
AABB	axis-aligned bounding boxes.
AHD	acromiohumeral distance.
AI	angulus inferior.
BBL	bony Bankart lesion.
BVH	bounding volume hierarchy.
CHD	coracohumeral distance.
CoR	center of rotation.
COV	glenoid coverage.
CT	computed tomography.
EL	lateral epicondyle.
EM	medial epicondyle.
FCL	`Flexible Collision Library`.
GC	glenoid center.
GH	glenohumeral.
GT	greater tuberosity.
GTC	glenoid track concept.
HA	humeral shaft axis.
HSA	hemi-shoulder arthroplasty.
HSD	Hill-Sachs defect.
ISB	International Society of Biomechanics.
LT	lesser tuberosity.
MRI	magnetic resonance imaging.
OBB	oriented bounding boxes.
PCA	principal component analysis.
ROM	range of motion.
RSA	reverse shoulder arthroplasty.
TS	trigonum spinae.
TSA	total shoulder arthroplasty.

Introduction

Shoulder mobility is essential for daily activities, but this same mobility makes the joint vulnerable to dislocation and bone defects. These issues often arise after trauma or repetitive strain, and they can lead to significant pain and functional limitations. In such cases, clinicians must determine whether surgical intervention is necessary, and if so, which procedure is the most appropriate.

Despite advances in image-based planning and personalized medicine, there is currently no universal, accessible tool for evaluating shoulder joint engagement outside of arthroplasty. Most existing software focuses on total shoulder replacement, helping surgeons align and position implants. However, these tools are not designed to evaluate bone-preserving procedures. In many clinical cases (such as those involving HSD or BBL) the decision to operate depends on whether the lesion will engage during normal shoulder movement. This is a biomechanical question that current planning programs often cannot answer reliably. As a result, clinicians must rely on visual inspection and simplified thresholds, which may not fully reflect the patient's specific anatomy. Previous research has proposed advanced solutions using MRI , optoelectronic tracking, or musculoskeletal models [1], but these approaches are often too expensive or time-consuming for routine clinical use. A constraint-based simulation tool could help determine whether a lesion requires surgery, especially in cases where clinical decisions remain unclear [2].

This thesis introduces a patient-specific simulation framework to evaluate the ROM of the gleno-humeral joint under anatomical constraints. The input consists of segmented 3D reconstructions of the scapula and humerus obtained from CT data. These bone models are anatomically aligned relative to one another to define a neutral joint configuration and enable consistent motion simulations. The joint's solution space is explored using a hybrid strategy: a coarse sampling phase identifies broad regions of feasible motion, and a binary search then refines the boundaries where anatomical constraints begin to fail. These constraints include bone-to-bone collisions, insufficient glenoid coverage, and violations of key bony distances. The result is an envelope of the joint's biomechanical limits.

In addition to computing the solution space, the framework is used to demonstrate a possible clinical application. A post-processing analysis is conducted to check whether HSD engage during valid motion, based on the previously computed ROM envelope. This example shows how the framework could help assess risk factors in bone-preserving surgical planning.

This study focuses on the technical development and feasibility testing of the proposed framework. The approach is applied to a selection of patient-specific anatomical models to evaluate its ability to capture meaningful joint behavior. The following chapters present the current state of the art, the core objectives, the methodology developed, the results obtained, and an example of clinical application based on HSD engagement.

Chapter 1

Literature Review

The shoulder is the most mobile joint complex in the human body but also the most frequently dislocated, accounting for nearly 50% of all major joint dislocations [3]. This exceptional mobility is made possible by the anatomical configuration of the GH joint, where the humeral head articulates with the shallow glenoid cavity of the scapula, offering minimal osseous constraint [4]. Given its central role in shoulder kinematics and its vulnerability to instability, the GH joint is the primary focus of this thesis.

1.1 Anatomy

The shoulder complex includes three bones: the humerus, scapula, and clavicle, which together support a wide range of arm movements. The GH joint, as the main articulation, enables multiplanar motion but is inherently unstable due to its limited bony congruence [5]. Its stability depends on the integrated function of the joint capsule, labrum, ligaments, rotator cuff muscles, and neuromuscular control mechanisms.

1.1.1 Bony Structures and Key Landmarks

The humerus (see Figure 1.1) plays a central role in shoulder function. Its humeral head is spherical and articulates with the glenoid fossa of the scapula. The greater tuberosity, located laterally, serves as an attachment site for the supraspinatus, infraspinatus, and teres minor, whereas the lesser tuberosity, located more medially, is the insertion point for the subscapularis. Between these tuberosities lies the bicipital groove, where the tendon of the long head of the biceps brachii passes through, contributing to anterior shoulder stability. Distally, the lateral and medial epicondyles provide anchorage for forearm muscles [6], [7].

The scapula (see Figure 1.1), a large triangular bone, forms the posterior foundation of the shoulder joint. Several scapular landmarks serve as important anatomical reference points. The trigonum spinae (TS), located at the root of the scapular spine, corresponds to the midpoint of the triangular surface on the medial border of the scapula. The angulus inferior (AI) defines the lower border of the scapula. The angulus acromialis (AA), defined as the most laterodorsal point of the scapula, is located near the base of the acromion, which articulates with the clavicle at the acromioclavicular joint. Anteriorly, the coracoid process (processus coracoideus) extends forward and serves as the attachment site for the coracobrachialis, pectoralis minor, and the short head of the biceps brachii [6], [7].

At the core of shoulder articulation lies the glenoid fossa, a concave structure that interacts with the humeral head. The glenoid has an inverted pear shape, with greater width in its inferior portion. It is covered by articular cartilage, which is thickest at the periphery, optimizing load distribution. The glenoid

labrum, a fibrocartilaginous ring, increases the depth of the glenoid cavity, enhancing joint stability and reducing humeral head translation [7].

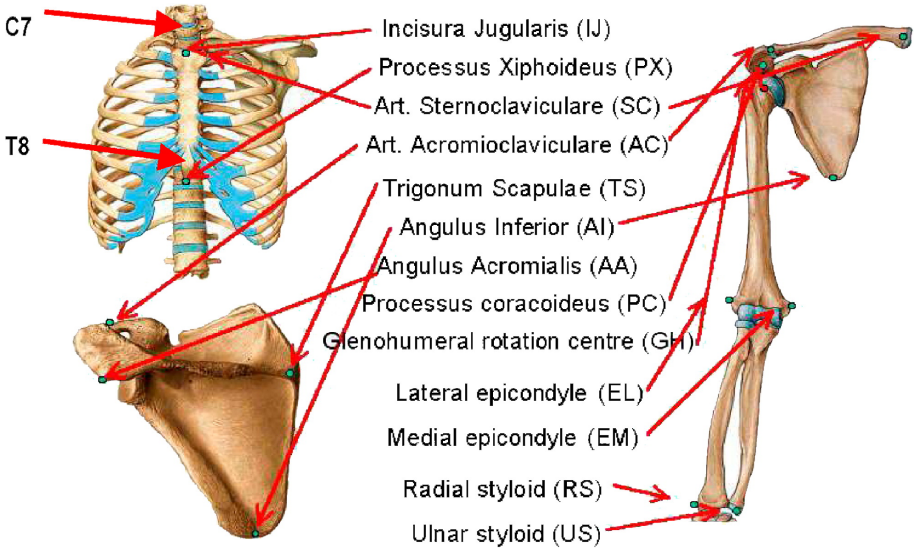

Figure 1.1: Bony landmarks of the thorax, clavicle, scapula, and humerus [6].

1.1.2 Soft Tissues and Muscular Contributions

Soft tissue structures surrounding the shoulder joint facilitate joint motion and dynamic stability. The rotator cuff, consisting of the supraspinatus, infraspinatus, subscapularis, and teres minor, is primarily responsible for dynamic control of the humeral head within the glenoid fossa [4]. These muscles work synergistically to compress the humeral head against the glenoid, minimizing excessive translation during movement [5].

Additional muscles include the deltoid, which generates force for arm elevation, and the scapular stabilizers, such as the trapezius, serratus anterior, and rhomboids, which ensure coordinated scapular movement. The biceps brachii, particularly the long head, plays a secondary role in stabilizing the humeral head, particularly in resisting anterior displacement [4].

1.1.3 Stability Mechanisms of the Shoulder

The stability of the GH joint is maintained by a combination of osseous configuration, passive stabilizing structures, and dynamic stability. The osseous architecture of the humeral head and glenoid provides intrinsic stability, but due to the shallow nature of the glenoid, its contribution is limited. The glenoid labrum increases socket depth and improves joint congruency, reducing the risk of dislocation [4], [7], [8].

Passive stability is further reinforced by the joint capsule and the GH ligaments which act to restrict excessive translation of the humeral head. Additionally, these structures maintain a negative intra-articular pressure, which provides a suction effect that supports joint coherence during rest and motion [4], [7].

Unlike passive stabilizers, dynamic stability relies on neuromuscular control. The rotator cuff muscles actively compress the humeral head into the glenoid, ensuring proper articulation. In addition, scapular stabilizers, such as the trapezius, serratus anterior, and levator scapulae, maintain optimal shoulder mechanics [4], [5].

The combination of these stability mechanisms allows the shoulder joint to achieve high mobility while maintaining functional stability. Disruptions in osseous alignment, soft tissue integrity, or neuromuscular

coordination can lead to instability, subluxation, or dislocation [5].

1.2 Shoulder Range of Motion

The shoulder complex provides six degrees of freedom, with the GH joint contributing the majority of rotational capacity. While shoulder motion arises from a combination of glenohumeral, scapulothoracic, acromioclavicular, and sternoclavicular joint movements, the GH joint plays the dominant role in achieving large ranges of motion in all three anatomical planes [4].

In the sagittal plane, shoulder flexion refers to forward elevation of the arm. It typically reaches a range of 180°. In contrast, shoulder extension describes backward movement of the arm and has a normal range of 45-60°.

In the frontal plane, abduction corresponds to a movement away from the midline. This motion has an average range of 150°. Adduction, which returns the arm toward the body, is more constrained due to physical contact and capsular limitations.

Rotations about the longitudinal axis of the humerus occur in the transverse plane. Internal rotation, which turns the humerus medially toward the trunk, exhibits an normal range of 70-90°. External rotation, turning the humerus away from the midline, with a normal range of 90°.

These large angular excursions are facilitated by a coordinated interaction between the GH and scapulothoracic joints, especially during arm elevation. This interaction is known as the scapulohumeral rhythm, where motion beyond 90° of elevation typically follows a 2:1 ratio (two degrees of GH rotation for every degree of scapular upward rotation) [5]. This synergy is essential for preserving shoulder stability, optimizing muscle force generation, and avoiding impingement. Alterations in this rhythm, known as scapular dyskinesis, are frequently observed in pathological conditions such as rotator cuff disease or impingement syndrome [9].

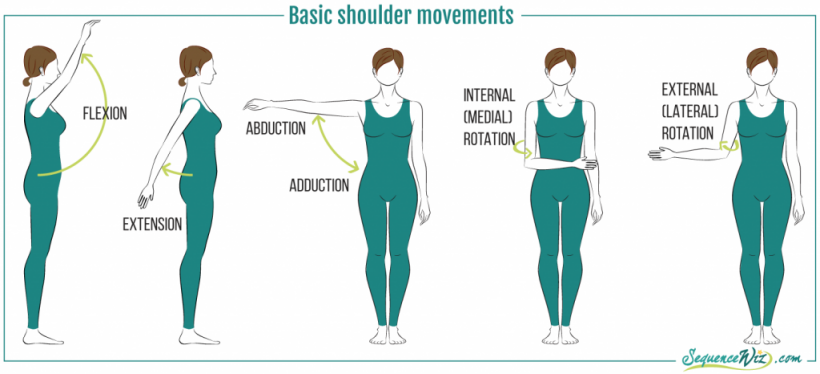

Figure 1.2: Description of the different movements of the shoulder. From left to right: flexion, extension, abduction/adduction, internal rotation, and external rotation. Retrieved from: `https://sequencewiz.org/wp-content/uploads/2016/03/Shouldermotions.png`

1.3 Glenohumeral luxations

Dislocations often occur following traumatic events or due to intrinsic joint instability. Dislocations can be classified according to their cause, direction, severity, and recurrence [3]. Traumatic dislocations are often due to sports injuries, falls, or motor vehicle accidents, while atraumatic instability is associated with hyperlaxity [10].

Dislocation often presents with acute pain, limited ROM, and visible deformity. It may be complete or partial (subluxation), depending on whether the humeral head fully disengages from the glenoid [10].

The incidence of shoulder dislocations is highest among young, physically active individuals, particularly males between the ages of 21 and 30, due to their greater involvement in high-risk activities. However, in older patients, dislocations are often accompanied by rotator cuff injuries, making management and recovery more complex [11].

Shoulder dislocations are categorized based on the direction of humeral displacement, with anterior dislocations being the most prevalent, accounting for approximately 97% of cases. This type occurs when the humeral head is forced forward out of the glenoid cavity, typically due to a combination of external rotation and abduction. Posterior dislocations, which comprise approximately 2-4% of cases, are often associated with seizures, electrocution, or direct posterior forces applied to the shoulder. Inferior dislocations are rare but clinically significant, as they are often associated with neurovascular compromise due to excessive downward displacement of the humeral head [3].

The severity of a dislocation depends on the extent of soft tissue damage and the frequency of recurrence. Acute first-time dislocations may involve minimal structural injury if quickly reduced, while recurrent dislocations frequently result in progressive damage to the labrum, joint capsule, and GH ligaments, further predisposing the joint to instability [10]. The long-term consequences of recurrent dislocations include chronic pain, decreased functional capacity, and an increased risk of osteoarthritis.

1.4 Possible injuries

Glenohumeral dislocations frequently result in damage to soft tissue, bone, and neurovascular structures. The extent of injury varies depending on the dislocation mechanism, the degree of displacement, and the presence of recurrent instability.

Among soft tissue injuries, labral Bankart lesions (anteroinferior labral tears) are closely associated with anterior dislocations and contribute significantly to recurrent instability. These lesions are reported in approximately 90% of patients experiencing a first-time anterior dislocation [10], [12]. Rotator cuff tears are also common, particularly in older patients, where up to one-third of dislocations involve tendon injury [13]. Ligamentous damage, especially to the inferior GH ligament complex, can further compromise stability.

Bony defects are also frequently observed following dislocation. On the glenoid side, repeated anterior dislocations may lead to attritional bone loss or fractures, including BBL defined as fractures of the anteroinferior glenoid rim. These bony lesions are found in approximately 20% to 30% of first-time dislocations and up to 50% of recurrent cases [14], [15]. On the humeral side, HSD result from compression of the humeral head against the glenoid rim [16]. HSD associated with humeral bone loss are observed in approximately 38% to 88% of patients with recurrent shoulder instability [14]. These defects, especially when large or engaging, significantly increase the likelihood of redislocation. Illustrations of a Bankart lesion and a HSD are shown in Figure 1.3.

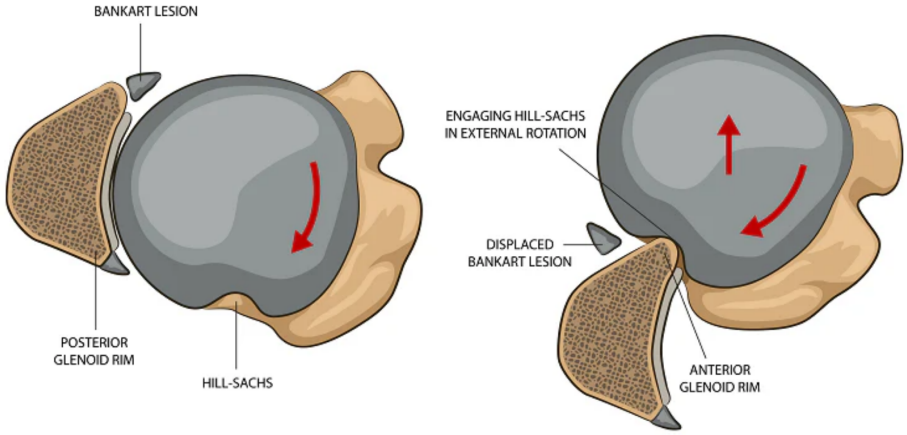

Figure 1.3: Common osseous and soft tissue injuries following anterior shoulder dislocation. The image shows a Bankart lesion and a Hill-Sachs defect in the rest (left) and engaging (right) positions. Image source: `https://shoulderphysio.co.nz/shoulder-injuries/shoulder-dislocation-pathology/`

Recurrent instability also predisposes the shoulder to post-traumatic osteoarthritis, particularly in patients with repeated episodes of dislocation or subluxation. Progressive cartilage damage and bony remodeling can lead to chronic pain, stiffness, and reduced CT over time [14].

Neurological injuries, such as axillary nerve damage, can lead to motor and sensory deficits, and although rare, vascular injuries like axillary artery damage may occur, particularly in older individuals [11].

Assessment of these injuries relies on medical imaging. X-rays are routinely performed to confirm dislocation and identify associated fractures, while CT scans are preferred for evaluating bone defects and are considered the gold standard for evaluating osseous integrity. MRI and MR arthrography are more often used for soft tissue evaluation [14], [16].

Quantifying bone loss is essential in determining the need for surgical intervention. Methods include linear measurements (e.g., Griffith index), surface-based estimations (e.g., Pico and Sugaya methods), and statistical shape modeling to reconstruct native glenoid anatomy [17]. Similarly, HSD are evaluated based on their depth and angulation, which influence the likelihood of engagement with the glenoid rim during movement [18].

Determining whether a HSD is engaging is crucial in selecting the appropriate treatment approach. The off-track/on-track concept, described by Di Giacomo et al., compares the lesion's width to the glenoid track, which represents the contact area between the glenoid and humeral head during movement [16]. If the lesion extends beyond the glenoid track, it is considered off-track, increasing the risk of engagement and redislocation.

However, recent studies indicate that the glenoid track concept (GTC) alone is insufficient to predict Bankart repair failures. In a study of failed arthroscopic Bankart repairs, it was found that 15% of shoulders with "on-track" lesions still experienced recurrent instability [19].

1.5 Current solutions

The management of GH instability depends on the extent of soft tissue and bone damage, recurrence risk, and patient-specific factors such as age, activity level, and functional requirements. Treatment strategies range from conservative therapy to complex surgical interventions designed to restore stability and joint function [13], [14].

Non-surgical treatment is generally indicated in cases of low-grade instability without significant bone loss. Rehabilitation focuses on strengthening the rotator cuff and scapular stabilizers, enhancing proprioception, and avoiding high-risk activities. This approach may also serve as a postoperative adjunct following surgical stabilization [13].

When soft tissue stabilization is required, particularly in cases of recurrent anterior instability without significant bone loss, arthroscopic Bankart repair is the standard surgical approach (Figure 1.4b). This technique involves reattachment of the detached anteroinferior labrum and capsule to the glenoid rim, restoring the normal tension of the inferior GH ligament complex. Bankart repair is most effective in patients with isolated soft tissue injury, especially younger individuals and athletes [13], [14].

When soft tissue repairs are insufficient, particularly in the presence of glenoid bone loss exceeding 15–20%, surgical procedures that restore bony support become necessary. Among these, the Latarjet procedure (Figure 1.4a) is the most widely used. It involves transferring the coracoid process to the anterior glenoid rim, providing both static stability through bone augmentation and dynamic stability via the conjoined tendon sling effect [20]. This dual mechanism makes it especially effective in young, active patients. However, the procedure is technically demanding and poses challenges for revision surgery. It has also been associated with reduced postoperative CT and an increased risk of GH osteoarthritis over time [21]. In acute cases involving glenoid rim fractures, open reduction and internal fixation (ORIF) may be performed to anatomically restore the glenoid surface and preserve joint congruency [14].

Humeral head defects, such as HSD, are managed based on size and engagement risk. Small non-engaging lesions may be treated with Remplissage (Figure 1.4b), while moderate defects may require HemiCAP resurfacing (Figure 1.4c) or osteochondral allografting, particularly in younger patients. In severe cases (»40% bone loss), prosthetic solutions such as HSA (Figure 1.5b) are considered, especially when the glenoid remains intact [14].

Arthroplasty is indicated when instability is associated with advanced joint degradation, massive rotator cuff tears, or extensive bipolar bone loss. In patients with preserved rotator cuff function, TSA (Figure 1.5a) can restore CT and reduce pain. When the rotator cuff is deficient or irreparable, RSA (Figure 1.5c) becomes the preferred option. RSA reverses the ball-and-socket orientation, allowing the deltoid muscle to substitute for deficient cuff function. It is particularly useful in elderly patients and those with complex instability patterns or revision cases [2], [22].

1.5.1 Surgical Planning and Patient-Specific Considerations

Despite technological advancements, current surgical planning software is primarily designed for implant alignment, with limited capability for evaluating classic surgical procedures [2]. Many clinicians have noted the lack of a universal planning tool for assessing defect engagement and surgical necessity beyond prosthetic-based reconstruction. Although patient-specific planning software has been explored, such as optoelectronic systems combined with MRI, these remain impractical for routine clinical use due to cost and technical limitations [1].

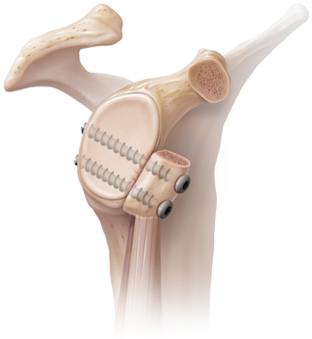

(a) Latarjet procedure

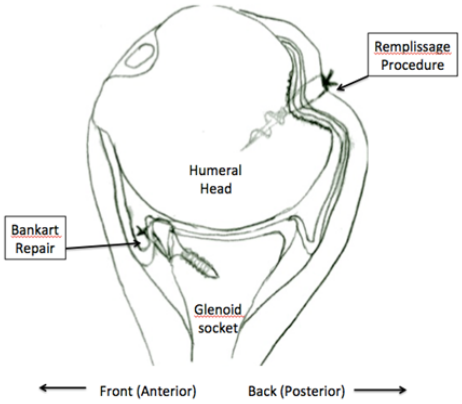

(b) Remplissage + Bankart repair

(c) HemiCAP resurfacing

Figure 1.4: Surgical techniques for GH stabilization. (a) Latarjet procedure involves coracoid transfer for anterior bony support. (b) Remplissage combined with Bankart repair addresses engaging Hill-Sachs lesions. (c) HemiCAP resurfacing is used to restore the articular surface in moderate humeral head defects. Image sources (from left to right): `https://www.arthrex.com/shoulder/latarjet-coracoid-process-transfer-for-glenoid-deficiency`, `https://bostonshoulderinstitute.com/treatment-of-recurrent-anterior-shoulder-instability/remplissage/`, and `https://www.orthobullets.com/shoulder-and-elbow/3077/shoulder-resurfacing`

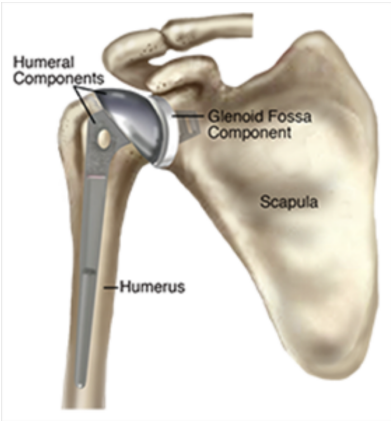

(a) Total shoulder arthroplasty (TSA)

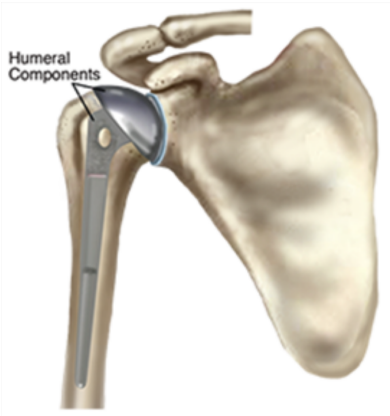

(b) Hemiarthroplasty (HSA)

(c) Reverse shoulder arthroplasty (RSA)

Figure 1.5: Types of shoulder arthroplasty. (a) TSA preserves anatomical joint structure and requires intact rotator cuff function. (b) HSA replaces only the humeral head and is used when the glenoid is preserved. (c) RSA reverses joint anatomy to allow deltoid compensation in cases of rotator cuff deficiency. Illustration retrieve from: `https://www.choosept.com/guide/physical-therapy-guide-total-shoulder-arthroplasty-replacement`

Chapter 2

Objectives

Based on the motivation introduced in the first chapter, this work addresses a gap in shoulder planning tools for bone-preserving procedures. The goal of this thesis is to develop and evaluate a patient-specific framework for simulating glenohumeral joint ROM under clinically meaningful constraints. In clinical practice, the ability to determine whether a bone defect compromises joint stability could significantly improve surgical decision-making.

To achieve this, several methodological challenges must be addressed.

The first requirement is to define what constitutes an invalid joint configuration. While many positions fall within the mechanical limits of the shoulder, some are clinically unacceptable due to bone contact, insufficient glenoid coverage (COV), or violation of critical inter-bony distances such as the acromio-humeral and coraco-humeral gaps. These constraints are essential for filtering the raw configuration space into a clinically interpretable solution space. Their formulation and implementation are presented in Section 3.1.

Before simulating joint motion, patient-specific 3D models must be aligned to define a consistent neutral pose. This alignment is performed between the scapula and humerus using anatomical landmarks and conventions from the ISB. The initialization process is described in Section 3.2.

Exploration of the configuration space must then be performed efficiently. Exhaustive evaluation of all possible positions is computationally prohibitive. To address this, a hybrid search strategy is employed. It combines a coarse scan to identify the global structure of the solution space with binary refinement at the boundaries, where motion becomes limited by constraints. This algorithmic approach is described in Section 3.3.

To support clinical usability, the simulation framework must also be computationally efficient. A number of strategies are introduced to reduce execution time while preserving spatial and clinical accuracy. These include early stopping, adaptive sampling, and filtering of redundant calculations. The optimization techniques are described in Section 3.5.

Once valid configurations have been identified, the results must be presented in a way that supports interpretation by both clinicians and engineers. Three complementary visualization strategies are proposed: (i) global maps of valid positions, (ii) constraint sensitivity visualizations, and (iii) anatomical projections of feasible motion. These views are designed to support both clinical insight and technical refinement. They are described in Section 3.6.

The following chapters implement and apply this methodology. Chapter 4 presents the results obtained on a set of patient-specific models. Chapter 5 interprets these results in a clinical and technical context. Chapter 6 then illustrates a possible post-processing application involving HSD engagement. The thesis concludes in Chapter 7, where future perspectives and possible extensions are discussed.

Chapter 3

Method

This chapter introduces a numerical approach to estimate the GH joint's ROM using 3D models reconstructed from CT scans. The goal is to simulate humeral movements and identify joint positions that remain anatomically valid throughout motion. By combining anatomical alignment and a rotation-based exploration of movement, the method aims to reconstruct a motion space that reflects the joint's ROM. To ensure anatomical plausibility, the simulated positions are evaluated using dedicated constraints, which are introduced in the following section.

3.1 Criteria for Identifying Invalid Positions

To determine which humeral positions are anatomically acceptable, a set of exclusion criteria must be applied. These criteria act as filters, removing poses that would be mechanically unstable, anatomically impossible, or clinically unsafe. While the method does not explicitly simulate soft tissues, the constraints are designed to reflect the key roles of joint stability, contact avoidance, and soft tissue preservation.

Each constraint is tested both at the initial configuration and throughout the simulated ROM. The following subsections describe the conditions in detail and explain how they are computed from 3D bone geometry.

3.1.1 Bone Collision

One of the primary constraints for defining anatomically valid positions is the absence of collision between the humerus and the scapula. Collision detection is performed using the `CollisionManager` class from the `trimesh` Python library [23], which internally relies on the `Flexible Collision Library` (FCL) [24] for efficient mesh-based proximity queries.

To accelerate the process, `trimesh` preprocesses the scapula mesh into a bounding volume hierarchy (BVH) composed of axis-aligned bounding boxes (AABB). This hierarchical structure allows for efficient broad-phase collision detection by quickly discarding regions of the scapula that do not overlap with the humerus. The humerus mesh is then independently tested against this BVH using a built-in collision detection function from `trimesh`, which performs direct intersection queries without requiring a separate BVH for the humerus. If the bounding volumes of the scapula and humerus overlap, a narrow-phase triangle-triangle intersection test is performed to confirm collision. This method optimizes computational efficiency by reducing the number of necessary fine-scale intersection checks.

This pipeline provides reliable and fast collision checks which is essential for the iterative search algorithm used to estimate the ROM. The use of AABB, although less precise than more complex bounding

volumes like oriented bounding boxes (OBB), is particularly effective for CT-derived meshes where the relative orientation of bones is limited.

Resolution and Robustness of the Collision Detection

To quantify the resolution and robustness of the `CollisionManager`, a series of controlled experiments are conducted using simplified STL geometries and contact setups (illustrated in Appendix E): (1) sphere-to-face, (2) cube face-to-face, and (3) cube edge- or corner-to-face. Each test involved incrementally translating one mesh toward the other along a controlled axis until collision was first detected. A binary search algorithm with a tolerance of 10^{-7} mm is used to precisely estimate the contact threshold, i.e. the distance between the centers of the two meshes at which collision is lastly avoided.

For axis-aligned configurations, such as a sphere approaching a cube face or two cubes aligned face-to-face, the contact occurs at a center-to-center distance of exactly 1.0000 mm. This is consistent with the known geometry, where each object has a radial or half-width extent of 0.5 mm. The detection resolution, defined as the smallest distinguishable non-collision gap, is measured at approximately 5.96×10^{-8} mm. This value corresponds to the expected numerical precision limit of the FCL, which operates using single-precision floating-point (`float32`) arithmetic.

To evaluate more complex scenarios, a cube is rotated 45° around both the X and Z axes, causing a corner or edge to face the opposing object. Along the X and Y axes, the measured contact threshold is 1.3536 mm. This result closely approximates the analytical center-to-center distance of 1.3660 mm, calculated as the sum of the opposing cube's half-width (0.5 mm) and the rotated cube's corner-to-center diagonal $\left(\sqrt{3 \cdot 0.5^2} \approx 0.8660 \text{ mm}\right)$. Along the Z axis, the measured contact occurred at 1.2071 mm, which corresponds to an edge-to-face contact. In this case, the effective reach of the rotated cube is $\sqrt{0.5} \approx 0.7071$ mm, leading to an expected threshold of $0.5 + 0.7071 = 1.2071$ mm.

In all cases, the collision resolution remains consistent at 5.96×10^{-8} mm, confirming that the collision detection pipeline is both precise and reliable across a variety of geometric conditions. These findings justify the use of `CollisionManager` as a robust constraint mechanism when exploring anatomically valid joint configurations and ROM limits.

Table 3.1: Collision accuracy and resolution under different mesh configurations. All values are rounded to 4 decimal places for readability. Measurements were obtained using a binary search algorithm with a tolerance of 10^{-7} mm. The reported resolution reflects the smallest detectable gap by the collision engine. Representation of the mesh setups in Appendix E.

Tests	**Axis**	**Expected (mm)**	**Measured (mm)**	**Error (mm)**	**Resolution (mm)**
Sphere → Cube	X-Y-Z	1.0000	1.0000	0.0000	5.9605e−08
Cube (face) → Cube	X-Y-Z	1.0000	1.0000	0.0000	5.9605e−08
Cube (corner) → Cube	X-Y	1.3660	1.3536	0.0125	5.9605e−08
Cube (edge) → Cube	Z	1.2071	1.2071	4.7503e-08	5.9605e−08

3.1.2 Glenoid Coverage (COV)

The glenoid is a concave surface that articulates with approximately 33% of the humeral head, providing critical support for joint stability and enabling humeral head rotation and gliding [5]. However, in this study, the labrum, which significantly increases the glenoid's concavity, is not included in the segmentation due to

CT imaging limitations. As a result, the stabilizing effect of COV may be underestimated and thresholds need to be adapted.

To assess joint stability, a *ray-based intersection method* is used to quantify the COV of the humeral head. If the computed COV falls below a defined threshold, the corresponding position is considered unstable and excluded from the ROM analysis. The method is illustrated in Figure 3.1 and consists of the following steps:

1. **Defining anatomical regions:**
   - *Glenoid region:* The edge vertices of the glenoid fossa are manually selected to form a closed loop. These are used as ray origins.
   - *Humeral head articular surface:* The surface is extracted from the humerus mesh using a loop of points around the humeral neck and a surface segmentation tool based on topological selection (see Section 3.5).
2. **Ray-based intersection test:** Rays are cast from each glenoid vertex toward the center of the humeral head (concentric projection). A ray tracing module from the `trimesh` library is used to compute intersections between these rays and the humeral articular surface.
3. **Filtering valid intersections:** Intersections are retained only if they occur before reaching the humeral head center, ensuring that only true coverage points are considered. If fewer than four valid intersections are found, the position is considered unstable.
4. **Coverage area computation:** Valid intersection points are used to extract the corresponding sub-region of the humeral articular surface using the same topological segmentation method mentioned above. The coverage area is then defined as the surface area of this region.
5. **Coverage threshold:** The extracted coverage area is normalized by the total articular surface area of the humeral head. Due to methodological differences from previous studies, COV values computed here do not align directly with anatomical literature. As such, the threshold is set empirically based on visual inspection of stable poses across the dataset. Two thresholds are used: 15% for males and 13.5% for females, reflecting the fact that both the glenoid and humeral head surfaces are smaller in females, but do not scale down proportionally (See development in Appendix B) [25], [26].

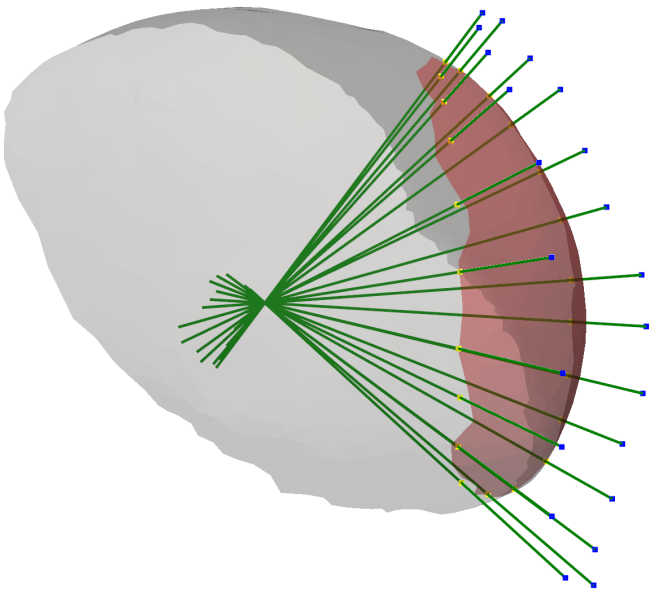

Figure 3.1: Overview of the COV computation. Rays (green) are cast from the glenoid contour (blue points) toward the center of the humeral head. Valid intersections (yellow) on the articular surface (gray) are used to define the coverage region (red), with a surface area normalized by the total articular surface to compute the COV percentage. (Patient 1 in initial pose)

While the proposed concentric projection method provides a robust and computationally efficient estimation of COV, some limitations must be acknowledged.

First, some regions of the glenoid contribute to the COV measure despite being relatively far from the humeral head's articular surface. While excluding these points may lead to an underestimation of COV, their inclusion would require additional biomechanical validation. In particular, future work should incorporate scapulohumeral rhythm models to account for dynamic scapular positioning during motion, which may bring these distant regions into more consistent contact or alignment with the humeral head. Currently, scapular motion is not modeled, limiting our ability to assess the physiological relevance of these areas.

Second, the labrum's stabilizing effect is assumed to be uniformly distributed across the glenoid. In reality, its thickness, width, and attachment vary around the rim, resulting in regionally different contributions to joint stability [8]. In this study, only CT scans were available, whereas accurate labrum segmentation typically requires MRI. As a result, the labrum could not be modeled explicitly, which may impact the accuracy of stability estimation in some cases.

Third, and most importantly, the COV metric is highly sensitive to the method used to compute it. A concentric projection method is chosen here, where rays are cast from the glenoid rim toward the center of the humeral head. This approach is favored over an orthogonal projection to a fitted glenoid plane, which tends to overestimate COV by including tangential points unlikely to reflect real contact. The underestimation introduced by the concentric projection acts as a conservative buffer in the absence of explicit bone contact modeling. However, this modeling decision directly affects the resulting COV values, making them incompatible with thresholds reported in literature, especially given the inconsistent or missing methodological descriptions in prior studies. As such, the empirical threshold of 15% (13.5% for females) was determined through extensive visual inspection of stable and unstable joint configurations. Though practical, this value has not been clinically validated and should not be interpreted as a universal anatomical constant.

Despite these limitations, the COV check remains a critical constraint in the proposed ROM estimation

framework. It ensures that simulated joint positions exhibit at least minimal anatomical containment and helps compensate for the absence of modeled soft tissue stabilizers.

3.1.3 Distance Thresholds to Prevent Impingement

The distance between certain bony structures and the humerus can be used to limit the ROM. A distance that is too small may indicate a risk of impingement involving soft tissues such as ligaments or tendons. To define meaningful thresholds, values from the literature must be considered. However, these thresholds often differ between studies. Also, they are typically defined in 2D (based on specific radiographic views) rather than in 3D. Moreover, thresholds vary in terms of their sensitivity and specificity: a higher threshold increases sensitivity (i.e., detecting more impingement-prone positions), but at the cost of decreased specificity (i.e., more false positives).

The first distance considered is the AHD. It is the shortest distance between the acromion and the closest point of the humerus. It serves as a radiological and anatomical marker to assess the subacromial space, and is commonly used to evaluate the presence of rotator cuff tears, subacromial impingement, or superior migration of the humeral head. As mentioned, several thresholds for AHD exist in the literature, and the choice of value depends on the desired sensitivity, specificity, and the clinical context (e.g., detecting partial versus complete rotator cuff tears). In the current study, the measurement is conducted in 3D, and previous work has shown that 3D assessments lead to smaller values than traditional 2D measurements [27]. To account for this dimensional difference, a correction of 1.5 mm is applied. Additionally, since multiple simultaneous constraints are applied during the ROM search, the system may be over-constrained, leading to premature locking. A lower threshold is therefore preferred, as it ensures sufficient specificity without overly restricting the solution space. As the lowest threshold reported in 2D is around 6 mm [28], a final 3D threshold of 4.5 mm is used for male patients. For females, an additional correction of 1 mm is applied to reflect typically smaller anatomical clearances[29], resulting in a final AHD threshold of 3.5 mm. These limits are typically reached during movements involving large external rotation.

The second distance considered is the CHD. Two main definitions exist in the literature. One approach defines CHD as the distance between the coracoid process and the lesser tuberosity (LT) of the humerus. This definition is often used to assess potential strain in the coraco-humeral ligament. However, strain is not the focus here. An alternative approach considers the minimum distance between the coracoid and any point on the humerus, which is more intuitive when trying to prevent impingement. This definition is adopted here. While the literature provides less information on the difference between 2D and 3D CHD measurements, it is known that 3D values tend to be slightly higher. A threshold of 8 mm is applied for male patients, consistent with a conservative limit that favors specificity over sensitivity [30]. For females, the threshold is reduced to 7 mm using a similar anatomical correction as for AHD[31]. These limits are typically reached during motions involving large internal rotation [30].

The current approach focuses on avoiding severe impingement that could lead to soft tissue damage. We decided not to use thresholds based on average values reported in healthy subjects for several reasons. First, normal distances are often defined only for specific joint positions and can vary widely across the ROM. Second, these values exhibit high standard deviations due to inter-individual anatomical variability, which complicates their use in a generalizable way. However, this variability also affects the current approach. In the absence of a personalization framework, fixed values representing the *minimum safe distance* for soft tissue clearance is considered more appropriate.

The presented method has several limitations. First, the thresholds used to detect impingement are not adapted to individual anatomies. Although fixed values were chosen to be conservative, this simplification may reduce accuracy in cases with atypical morphologies or joint mechanics.

A second limitation of this method is the use of thresholds derived from 2D measurements in a 3D

context. An alternative approach would be to project the 3D-measured distances onto clinically relevant planes to better match 2D thresholds. However, this would lose the advantage of adopting a 3D approach. Aware that 3D measurements tend to produce different values for the same pose, we chose to apply *conservative thresholds* accordingly. In future work, pure 3D-based thresholds should be investigated. Even then, the trade-off between sensitivity and specificity will remain. Due to time constraints, such an investigation is not conducted in this study.

Thirdly, while a *minimum distance threshold* is used to avoid impingement, a complementary *maximum distance threshold* could be implemented to prevent excessive soft tissue tension. However, the current constraint set and search algorithm already provide satisfactory results. Adding further constraints would increase computational cost (which, although not a central concern here, is an important consideration for practical use) and may risk over-constraining the system, potentially leading to search instability or locking. Moreover, maximum and minimum distance thresholds could conflict with each other (e.g., maximal CHD may occur during movements where minimal AHD is also reached), introducing unwanted dependencies. Since the literature does not provide strong or consistent recommendations for maximum distance thresholds, this condition was excluded from the current study. Nonetheless, it remains an interesting direction for future work.

To compute the AHD in three dimensions, multiple landmarking strategies were explored to select representative regions of the acromion. Three approaches were tested (Illustrated in Appendix D):

1. Using the entire inferior surface.
2. Selecting a refined "crest" region, defined as the subset of the surface most likely to approach the humerus.
3. Annotating a few key representative points (typically 5 to 10).

The first approach offers the highest accuracy but is computationally intensive. The third option achieves the best computational speed but is highly dependent on user selection, making it prone to inter-user variability. The second strategy, which selects a smart subset of surface points while preserving geometric fidelity, was chosen as the optimal trade-off (Figure 3.2). It offers robust accuracy across patients while significantly reducing computation time and user-dependency.

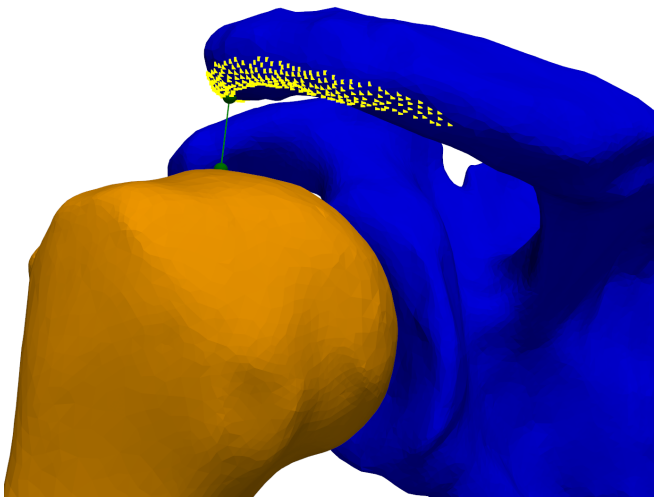

Figure 3.2: Computation of the acromiohumeral distance (AHD). The selected crest of the acromion is shown as yellow points. For each point, the nearest point on the proximal humerus (orange) is identified using a proximity query. The resulting connections (green lines) define the minimal distances between the two structures, with the shortest segment representing the AHD. (Patient 1 in initial pose)

A similar strategy is used to compute the CHD (Figure 3.3). A refined "crest" of the coracoid surface is selected to represent the anatomical region most at risk of anterior impingement. The minimum Euclidean distance between this crest region and the proximal humeral surface is then computed using a point-to-surface proximity query (from `trimesh`). For each crest point, the closest point on the humerus is identified, and the smallest of these distances is retained as the final CHD measurement.

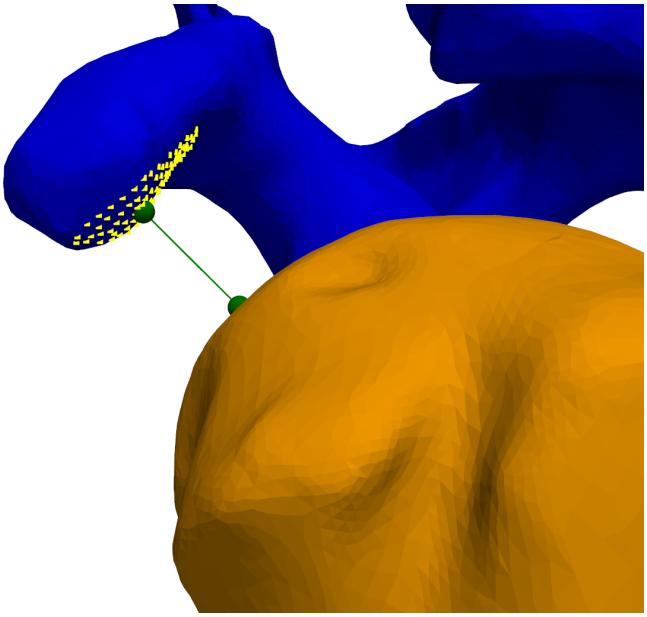

Figure 3.3: Computation of the coracohumeral distance (CHD). The selected crest of the coracoid process is shown in yellow. The nearest points on the proximal humerus (orange) are identified (green), and the shortest link (green line) represents the CHD. The scapula is shown in blue. (Patient 1 in initial pose)

Resolution and Robustness of the Proximity Query

To evaluate the reliability of this proximity-based measurement, the proximity query from `trimesh` is controlled using a set of synthetic STL geometries with analytically known contact distances (Results presented in Table 3.2). In ideal configurations involving a sphere or face-aligned cube, the method accurately returns a distance between meshes of 0 mm. However, in more challenging cases (such as when a rotated cube tip approached a flat face) an overestimation of approximately 0.0125 mm is observed. This loss of accuracy is attributed to the limited vertex resolution at sharp corners, which reduces proximity accuracy. Nevertheless, given that anatomical regions like the coracoid and acromion are broad and well-meshed, this method is considered sufficiently precise for the present use.

Table 3.2: Validation of mesh-to-mesh distance estimation using the proximity query from `trimesh`. The minimum unsigned distances between the moving and static meshes are compared to analytically expected values for known geometric setups. All values are rounded to 4 decimal places for readability. Representation of the mesh setups in Appendix E.

Tests	**Axis**	**Expected (mm)**	**Measured) (mm)**	**Error (mm)**
Sphere → Cube	X/Y/Z	4.0000	4.0000	0.0000
Cube (face) → Cube	X/Y/Z	4.0000	4.0000	0.0000
Cube (corner) → Cube	X/Y	3.6339	3.6464	0.0125
Cube (edge) → Cube	Z	3.7929	3.7929	4.4409e-16

This distance-based impingement criterion offers a method to detect potential soft tissue conflict, using only bony geometry. While simplifications were made due to the lack of scapular motion and soft tissue information, the thresholds adopted provide a conservative yet anatomically based tool for motion constraint.

3.1.4 Lesser Tuberosity Orientation Constraint

An additional anatomical constraint is applied based on the orientation of the lesser tuberosity (LT). The LT is expected to face anteriorly throughout the ROM under normal physiological conditions [32].

To apply this, the orientation of the humeral reference frame is used. Specifically, the local X_h-axis (constructed to point toward the LT during the frame definition) orientation is monitored in each tested position. If the X_h-axis rotates to a posterior-facing orientation, the position is considered anatomically implausible and invalid.

This constraint is not based on direct bony impingement but reflects a soft tissue limitation. A posterior orientation of the LT would imply excessive internal rotation or abnormal joint positioning, which could lead to increased strain on the anterior structures of the shoulder, including the subscapularis tendon, anterior capsule, and GH ligaments. While simple, this condition helps ensure that only physiologically reasonable positions are retained during ROM estimation, with negligible computational cost.

3.1.5 Conclusion

The combination of these criteria allows the exclusion of positions of the humerus that are anatomically implausible, mechanically unstable, or clinically unsafe. Each condition is based on known biomechanical or clinical principles and adapted for 3D mesh-based analysis. While simplifications are necessary due to the limitations of static CT data, the overall constraint system offers a framework for ROM analysis in the absence of dynamic soft tissue modeling.

Most implemented constraints represent indirect translations of soft tissue limitations into bony constraints, using bony landmarks or proximity-based conditions. For example, collision and COV account for mechanical stability, while minimum distance thresholds aim to avoid impingement that would otherwise affect tendons or ligaments. These criteria, while based on bony structures, are inherently motivated by soft tissue preservation.

However, one important exception is shoulder extension. This movement is primarily restricted by tension in the anterior capsule and associated soft tissues, which do not correspond to any clear or consistent bony landmarks. As a result, it is not feasible to formulate a bony constraint that adequately reflects this physiological limitation. To address this, a manual angular threshold is imposed to constrain extension during the search. While this approach introduces an arbitrary element, it reflects a necessary simplification to account for physiological restrictions that cannot be captured by bone structures alone.

A summary of the constraints and their goals is provided in Table 3.3.

Table 3.3: Summary of criteria used to classify invalid humeral positions.

Criterion	**Threshold**	**Main Risk Prevented**
Bone collision	None (binary)	Bone-to-bone contact
COV	< 15 or 13.5%	Joint instability
AHD	< 4.5 or 3.5 mm	Subacromial impingement and associated soft tissue compression
CHD	< 8 or 7 mm	Anterior impingement and associated soft tissue compression
LT orientation	Posterior-facing	Avoids excessive strain on anterior soft tissues due to abnormal humeral rotation

3.2 Initialization

To analyze GH kinematics in a reproducible and anatomically meaningful way, the bones must first be placed in a standardized configuration. This is achieved by defining anatomical reference frames for both the humerus and the scapula, which allow for consistent interpretation and simulation of joint motion across patients.

The process begins with pre-segmented CT-based 3D models of the humerus and scapula, from which key anatomical landmarks are identified. These landmarks are then used to construct local coordinate systems that reflect the native orientation of each bone. Once the reference frames are defined, the bones are aligned into a standardized pose.

This initialization step ensures that all motion simulations start from a comparable baseline, reducing variability and enabling reliable computation of the ROM.

3.2.1 Humeral Reference Frame

To establish the humeral coordinate system, various methodologies can be employed depending on the availability and integrity of anatomical structures images. Two primary approaches are considered: a distal definition (ISB-based) and a proximal definition (LT-based).

ISB-based Reference Frame

The ISB standard proposes a reference frame based on three key landmarks [6]: the CoR of the GH joint, the lateral epicondyle (EL), and the medial epicondyle (EM).

The CoR of the GH joint is usually considered to be the center of a sphere fitted to the articular surface of the humeral head [33]. To obtain the articular surface, the humeral neck points are manually selected. The submesh corresponding to the articular surface is then extracted using `vtkSelectPolyData` (Described in Section 3.5). Representation of the articular surface and obtained sphere in Figure 3.4.

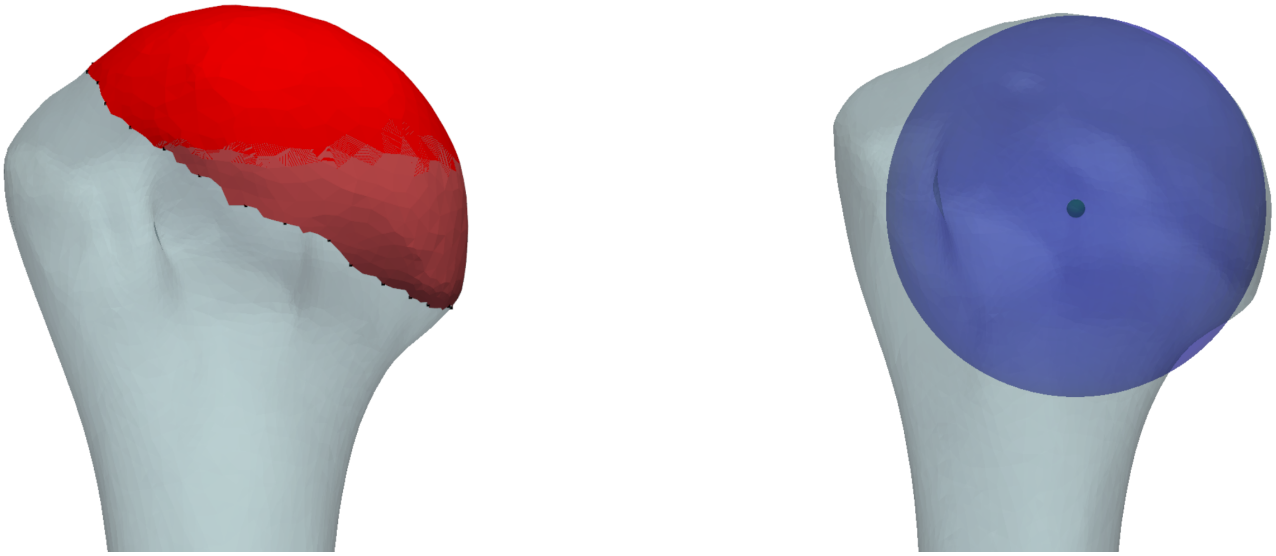

Figure 3.4: (**Left**) Extraction of the humeral head articular surface. Selected points are shown in black. The isolated articular surface (red) is segmented from the original humerus mesh (light blue). (**Right**) Sphere fitting (blue) to the articular surface enables estimation of the GH CoR (green). (Patient 1)

Using the center of a fitted sphere as the joint's CoR has limitations, particularly when incorporating translations into the system. This method assumes that the humeral head behaves as a perfect sphere and that the CoR remains stationary during motion. As noted by Ehrig et al. (2006) [34], this assumption is only reasonable if one of the two segments remains fixed during motion. In our case, since the scapula is considered static, this condition is fulfilled, making the sphere fit approach a reasonable approximation. While functional methods (such as symmetrical CoR estimation, helical axis analysis, or the minimal amplitude point method) can provide more physiologically accurate results, they require dynamic motion data, which is not available in this static CT-based context. Therefore, the sphere fit remains an appropriate and practical choice for estimating the CoR here.

The EL is manually selected as the most lateral point of the distal humerus. The EM is manually selected as the most medial point of the distal humerus.

Based on the landmark positions, the humeral reference frame is constructed as described in the ISB's recommendations [6]:

- Origin of the system (Oh): the CoR of the GH joint
- Yh: the line connecting the CoR of the GH joint and the midpoint of EL and EM, pointing to the origin
- Xh: the line perpendicular to the plane formed by EL, EM, and the CoR of GH, pointing forward (anteriorly)
- Zh: the common line perpendicular to the Yh and Xh axis, pointing laterally

The reference frame is shown in Figure 3.5.

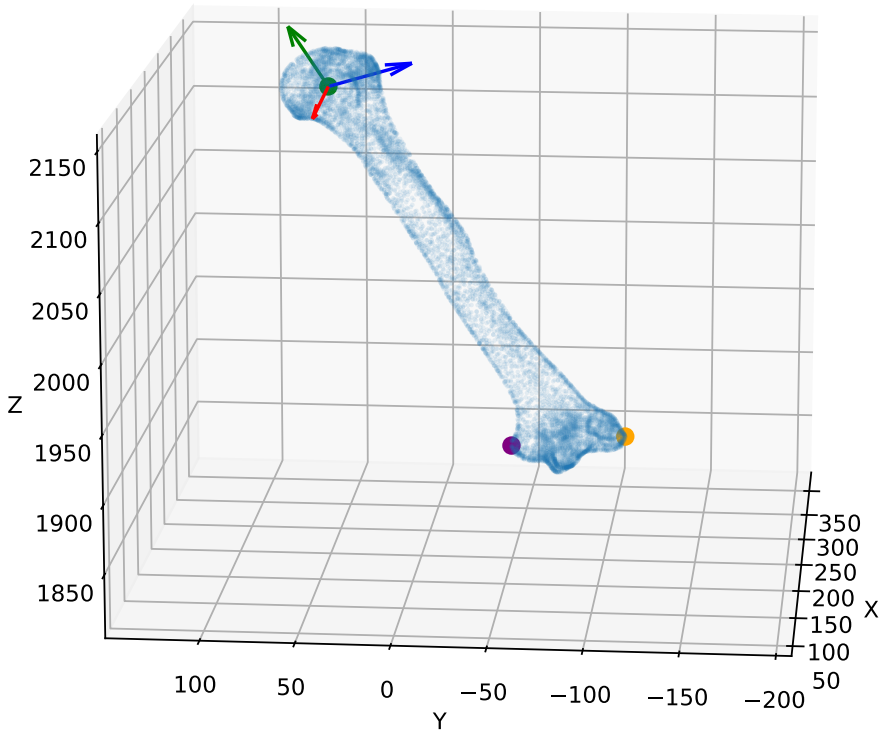

Figure 3.5: Definition of the ISB-based humeral reference frame (Xh in red, Yh in green, and Zh in blue). The origin (Oh) is the GH CoR (green), with axes constructed based on the origin, the lateral (orange) and medial (purple) epicondyles. (Patient 1)

Proximal Reference Frame

The main limitation of the ISB-based reference frame lies in the reliance on distal humeral landmarks. In practice, clinical imaging often excludes the distal humerus. Such setups are present in the dataset used in this project, requiring the study of a proximal reference system. A commonly used proximal reference is based on the three following landmarks [33]: the CoR of the GH joint, the lesser tuberosity, and the humeral shaft axis.

The CoR of the GH is determined as in the ISB-based reference frame. The LT is manually selected as the most prominent point of the tuberosity. LT is chosen for its reliability and precision. In some pathological situation (not present in this dataset) the greater tuberosity (GT) can be used when LT is too damaged. If both LT and GT are damaged, one can use the crest of the greater tuberosity [33].

The humeral shaft axis (HA) is approximated with a cylinder fit of a segment of the shaft using principal component analysis (PCA) as an initial guess and nonlinear least squares optimization to refine the fit. To account for uneven point density in the shaft mesh, a voxelization-based downsampling method is applied. Each voxel's centroid represents its region, ensuring uniform sampling while preserving the overall geometry. The quality of the fit seems not highly sensitive to the length of the shaft segment considered (same conclusion in Sulkar et al. (2021) [33]). An absurdly too small or too large segment would, of course, break the fitting. A segment length of 50 mm is selected as it is consistently present across all datasets and provides robustness and avoid effects of changes in shaft section.

The best location of the shaft segment on the whole shaft was evaluated thanks to the alignment of the obtained axis with the Yh axis of ISB-based reference frame. In conclusion, the shaft segment should be as close as possible to the humeral head without being impacted to the change of curvature of it. It

shouldn't be too far from the humeral head to avoid deep change of section of the shaft. The radius and the center of the fitted sphere is thus used to ensure that the shaft segment was outside of the humeral head while not too far from it.

A proximal reference frame can be defined as followed [33]:

- Origin (Oh): the GH CoR
- Yh: parallel to the fitted HA
- Zh: defined as the line orthogonal to the plane formed by the LT and the HA (laterally oriented)
- Xh: the cross product of the y and z axes, pointing toward the LT (anteriorly)

The reference frame is shown in Figure 3.6.

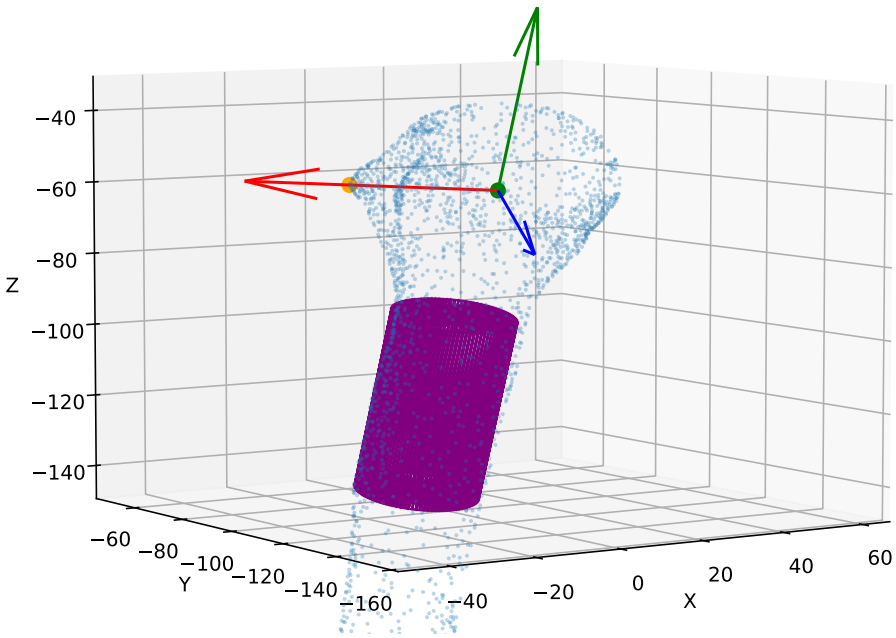

Figure 3.6: Definition of the proximal humeral reference frame (Xh in red, Yh in green, and Zh in blue). The origin (Oh) is the GH CoR (green), with axes constructed based on the origin, the lesser tuberosity (orange), and the humeral shaft axis (fitted cylinder in purple) (Patient 1)

The exact effect on the kinematics using a proximal reference frame is not entirely understood. Although absolute values may show an offset, the overall ROM remains largely unaffected. Moreover, the LT-based proximal reference frame has gained traction in recent years, facilitating comparison with other clinical and research studies. Sulkar et al. (2021) [33] has explored the definition of transformation matrices to switch between an ISB-based reference frame and a proximal reference frame.

In conclusion, even if ISB-based reference frames have been more studied and are developed for kinematics, limitations intrinsic to clinical imaging led us to choose a proximal reference frame approach to ensure that all CT-scans in the dataset could be analyzed. Even if some CT-scans in the dataset allow an ISB-based definition, we still only use LT-based reference frame to more easily compare all our results.

3.2.2 Scapular Reference Frame

As with the humerus, several methodologies exist to define a reference frame attached to the scapula. Although only one approach will be used throughout this project, multiple methods have been reviewed. This section begins by exploring these alternatives before describing the one adopted for the study.

The first definition considered is the ISB-based reference frame [6], which relies on three anatomical landmarks:

- TS: the mean point of the medial root of the scapular spine
- AA: the lateral tip of the acromion
- AI: the lowest point of the scapula

The reference frame is then defined as follows:

- Origin (Os): AA
- Zs-axis: the line connecting TS to AA, pointing toward AA
- Xs-axis: the line perpendicular to the plane formed by AI, AA, and TS, pointing anteriorly
- Ys-axis: the cross product of Xs and Zs, pointing superiorly

The use of the AA leads to a plane that does not coincide with the anatomical scapular plane, which may result in non-intuitive interpretations of the kinematics. However, the AA is more easily palpable than the GC, and, like glenoid-based methods, it reduces the risk of gimbal lock during Euler angle decomposition. The ISB reference frame also offers the advantage of being widely adopted in current literature, facilitating comparisons across studies. A final limitation lies in its reliance on distal landmarks, which may not be visible or well-resolved in all CT scans. The reference frame is shown in Figure 3.7.

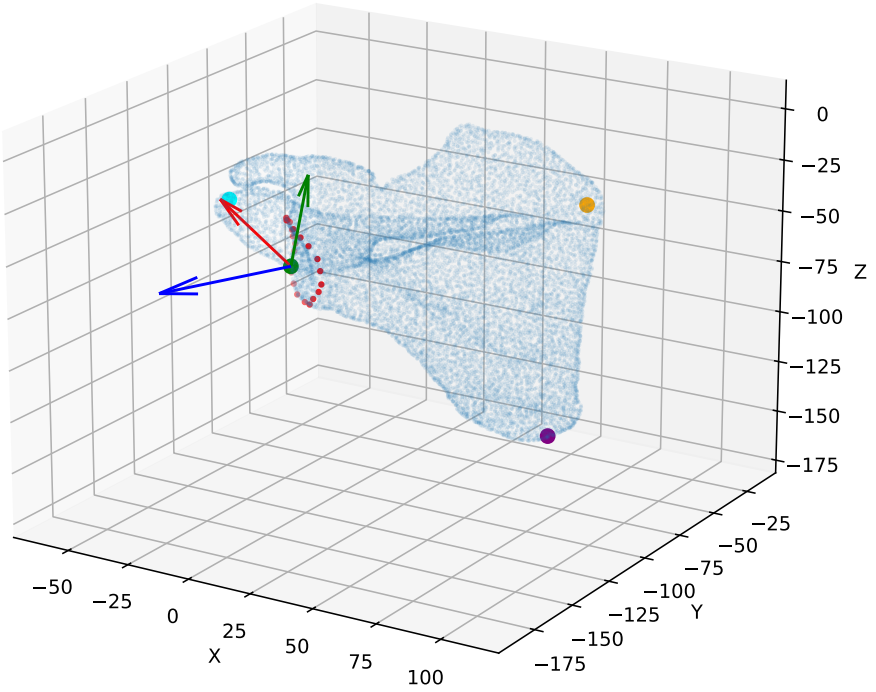

Figure 3.7: Definition of the ISB-based scapular reference frame (Xs in red, Ys in green, and Zs in blue). The origin (Oh) is the angulus acromialis (green), with axes constructed based on the origin, the trigonum spinae (orange), and the angulus inferior (purple). The glenoid region is delimited by red points. The acromio-clavicular joint is in cyan. (Patient 1)

To improve the anatomical relevance of the axes, a glenoid-based reference frame can be used. This method typically uses the trigonum spinae, the angulus inferior, and the GC as landmarks. Although this approach still depends on distal landmarks, it results in more anatomically intuitive axes, as the defined plane aligns better with the scapular plane. Moreover, it has been shown to further reduce the risk of gimbal lock compared to the ISB definition [35]. The main drawback is that the GC is not palpable, limiting the applicability of this method to imaging-based studies and preventing direct comparisons with motion capture studies using surface markers.

When the resolution of the CT scan is insufficient in the distal region, precise annotation of landmarks such as AA and AA may not be feasible. In such cases, the scapular plane can still be reconstructed using bony regions such as the supraspinatus fossa, lateral pillar, trigonum spinae, inferior angle region, and medial border. A transverse plane is then defined as orthogonal to this scapular plane, passing through the spino-glenoid notch and trigonum spinae center. In this configuration, three landmarks (the GC (as origin), spino-glenoid notch, and trigonum spinae center) are all relatively proximal and can be annotated more reliably. This method provides a better anatomical fit to the scapular plane while avoiding reliance on distal points.

To define a fully proximal frame, a glenoid-oriented reference frame may be used. In this case, only the glenoid surface is required, which is typically visible in any GH CT scan. The centroid of the glenoid surface serves as the origin, and the glenoid boundary is approximated by an ellipse. The X- and Y-axes are then aligned with the minor and major axes of this ellipse, respectively [36]. This method provides a proximal and glenoid-centered coordinate system and offers high precision in scapular kinematic tracking [35].

As with the humerus, several studies have investigated transformation matrices that allow conversion between different reference frames [37].

In the present study, scapular kinematics are not the primary focus. As such, gimbal lock and high-precision tracking are not critical considerations. Furthermore, the CT scans in our dataset consistently have sufficient resolution and field of view to allow manual annotation of all required landmarks. Considering these factors, and in order to maximize comparability with existing literature, we have chosen to use an ISB-based reference frame for all analyses. This approach is reproducible across our dataset and aligns with most current studies. However, if future work were to focus on scapular kinematics, a glenoid-oriented reference frame would likely be adopted instead.

3.2.3 Alignment

To perform a consistent determination of ROM, the meshes must first be aligned into a standardized initial configuration. In our methodology, the humerus is positioned in a neutral pose, where all local axes are aligned with the global coordinate system and all rotational angles are set to zero. In contrast, the scapula is placed in a rest position based on averaged anatomical orientation data [38]. It is important to note that while the neutral and rest positions of the humerus are relatively similar, this equivalence does not hold for the scapula. The scapular neutral pose (defined as alignment with the global axes) is not physiological and is therefore not used.

Because the humeral reference frame used in this study is proximal (LT-based), aligning it to a neutral position does not match the position it would occupy under the ISB-based definition. If this neutral configuration were translated into the ISB frame, it would correspond to a position involving notable internal rotation, slight abduction, and low flexion.

The position of the bones as seen in the original CT scans is not used as a reference for several reasons. First, it is highly dependent on the specific scanning protocol employed, which can vary significantly between institutions and cases. Second, there is no guarantee that the captured pose corresponds to a true resting state, as the level of muscular relaxation or arm support during acquisition is unknown. Third, CT scans are typically performed with the patient in a supine position, which contrasts with the standing or seated postures preferred for clinical ROM evaluations.

Instead, the alignment is performed algorithmically through successive rotations to achieve a standardized configuration. Initially, the scapular reference frame is aligned with the global coordinate system (considered to be the thoracic reference frame). Subsequently, the scapula is rotated using the Y_t–X_s–Z_s sequence as recommended by the ISB for scapular motion description [6]. The sequence of rotations applied is derived from average scapular rest angles, with values adjusted based on the patient's sex. Specifically, for male patients, the rotations applied are $-29.3°$ about the Y-axis (internal rotation), $-8.6°$ about the X-axis (upward rotation), and $10.7°$ about the Z-axis (anterior tilt). For female patients, the corresponding values are $-28.7°$ about the Y-axis, $-9.4°$ about the X-axis, and $7.0°$ about the Z-axis [38]. The sign of the Y and X rotations differs between left and right shoulders, reflecting the symmetry of anatomical structures (values provided here correspond to the left shoulder). These sex-specific differences, particularly in the anterior tilt of the scapula, are incorporated to enhance the anatomical accuracy of the initial alignment.

The rotation values are applied sequentially to both the scapula and the humerus, ensuring that each transformation maintains anatomical alignment and updates the local reference frames accordingly. Once the scapula is positioned, the humerus is rotated to align its reference frame with the global coordinate system, achieving a neutral pose. This step ensures that the humerus is in a standardized position relative to the thorax, facilitating consistent kinematic analyses across subjects. The obtained pose is shown in Figure 3.8.

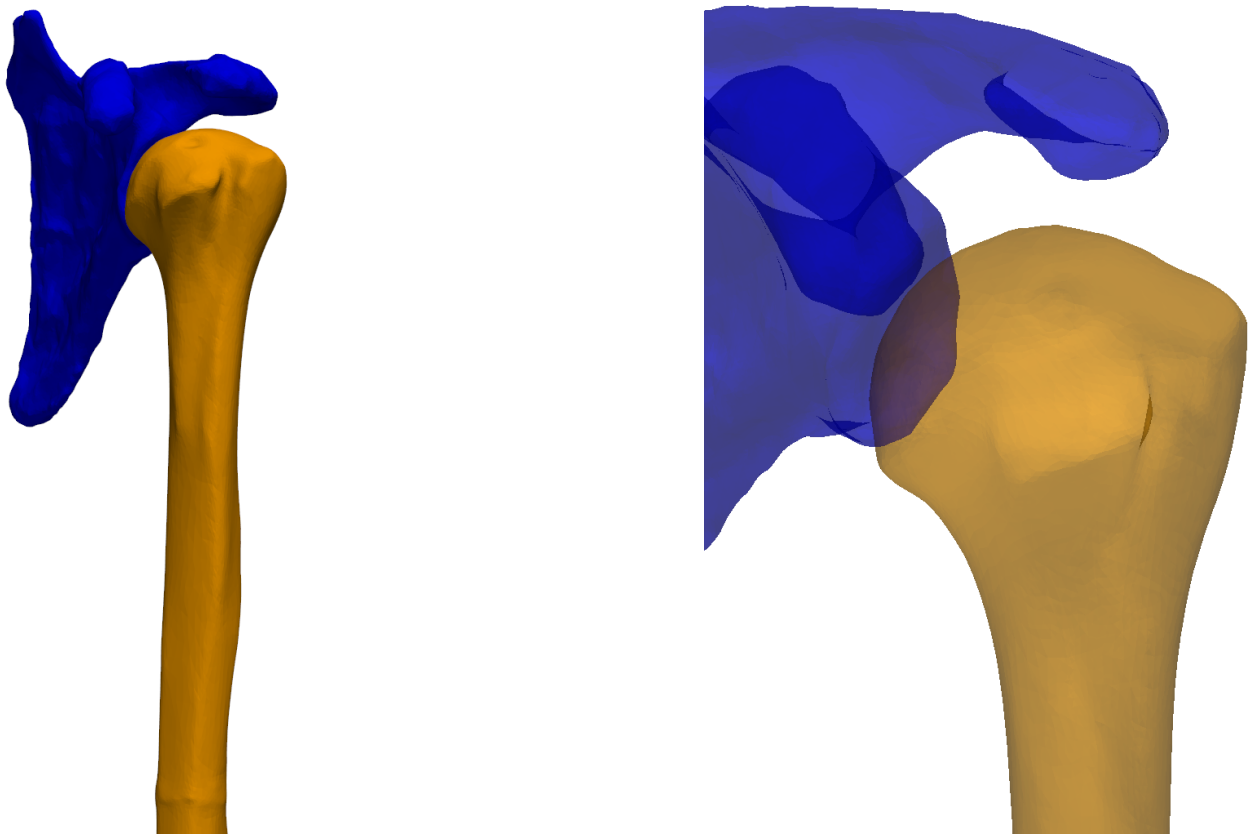

Figure 3.8: (**Left**) Standardized neutral pose of the scapula (blue) and humerus (orange) after alignment using the rotation sequence. (**Right**) Close-up view of the GH joint region, showing the joint configuration resulting from the transformation of both bone reference frames. (Patient 1)

Although these rotation values represent population averages and do not account for inter-individual variability, they offer a standardized approximation in the absence of subject-specific muscular or postural data, which could provide valuable feedback to determine a true rest position. Since soft tissue information is not available, this strategy provides a reasonable and repeatable initialization method.

It should be noted that the resulting pose is not guaranteed to be physically attainable by the patient. While using the CT scan position could, in theory, ensure physical feasibility, its variability and lack of standardization outweigh this potential benefit. In practice, if the initial pose fails to meet one or more of the kinematics conditions described in the previous section, the user is asked to manually adjust the position through transformations, and the applied rotation offsets are then registered. By consistently using the same initial pose for all patients, the resulting kinematic measurements become more comparable across the dataset.

Initial Translation

Optionally, an additional translation step can be applied to further standardize the initial configuration. This step is performed after completing the rotational alignment described above and is designed to improve the reproducibility of joint positioning across subjects. Specifically, the center of the glenoid is estimated by fitting a 2D ellipse to the glenoid region, after projecting it onto the best-fit plane. The fitted ellipse provides a robust and anatomically relevant approximation of the glenoid geometry, and its centroid is taken as the GC. The humeral head center is then translated to align it with the GC. This translation is constrained to occur within the glenoid plane, rather than along an arbitrary 3D direction.

While this translation improves standardization and comparability, it is not applied by default, as it modifies the natural spatial relationship between the scapula and humerus captured in the CT scan. This adjustment may reduce the subject-specific fidelity of the pose, particularly if passive joint alignment differs from the approximated glenoid-centered configuration. As a consequence, certain pathological configurations (such as superior humeral migration or anterior subluxation) may be artificially corrected by this translation, potentially obscuring clinically relevant deviations. Therefore, this step is considered optional and can be toggled depending on the desired trade-off between standardization and patient-specificity.

When applied, this translation is generally associated with increased COV, as well as higher values for the AHD and CHD. These effects suggest that the repositioned configuration may reflect a more stable and relaxed joint state compared to the unmodified pose. By improving these stability-related conditions, the translated position may offer a more functionally relevant baseline for evaluating the ROM. The resulting configuration is illustrated in Figure 3.9.

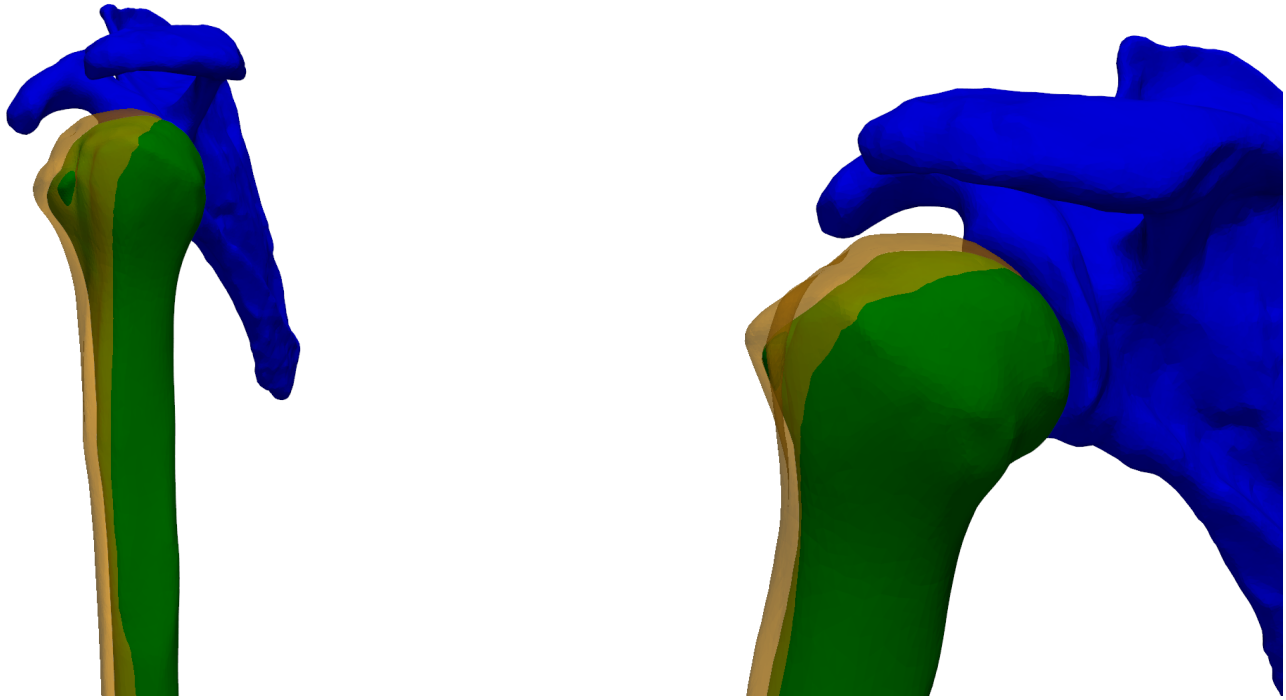

Figure 3.9: (**Left**) Standardized initial pose after applying the optional translation step, showing both the original humerus position (semi-transparent orange) and the translated position (green), aligned with the GC. (**Right**) Close-up view of the GH joint region after translation. (Patient 1)

3.2.4 Conclusion

Standardized initialization of the scapula and humerus ensures consistency across patients and enhances the reproducibility of ROM estimations. This process involves defining anatomical reference frames from 3D bone models, aligning the bones into a controlled configuration, and optionally translating the humeral head to the GC. Although the neutral pose is approximated and may not reflect the exact in vivo rest position, it provides a robust and comparable starting point for motion simulation. The use of a proximal humeral reference frame further supports consistent analysis across the dataset, particularly when distal landmarks are unavailable.

3.3 Search Algorithm

Once the bones are aligned in a standardized configuration, the next step is to explore the possible rotations of the humerus to estimate the full range of anatomically valid motion. The ROM estimation is performed through a hierarchical search algorithm that explores GH rotations around three anatomical axes, using an Euler-Cardan decomposition. These axes are referred to as the first, second, and third axes for generality. The specific decomposition order is discussed in the next section.

3.3.1 Algorithm Overview

The algorithm explores the search space using an Euler-Cardan decomposition with three nested loops corresponding to sequential rotations around the first, second, and third axes. The procedure begins with the first rotation, incrementing from 0° using a fixed step size. For each angle, the resulting humeral position is evaluated (using previously described constraints). If the position is valid, the algorithm proceeds; if it is invalid, a binary search is conducted between the current invalid angle and the last valid angle to precisely locate the boundary. After this binary search, the algorithm terminates the current branch and proceeds to the next primary rotation value. The overall logic of this algorithm is summarized in Figure 3.10.

This process is repeated for the second and third rotations, only for the configurations that result in valid positions from the previous rotation. All valid angle triplets (first, second, third axis) are recorded.

The search strategy employs uniform sampling (constant step size) within the valid ROM space and increases resolution near the invalid boundary using binary search. This hybrid approach was preferred over a direct binary search-based method that connects the origin to a boundary point, which would risk identifying non-representative boundary points due to the complex and discontinuous shape of the constraint space. In cases where the ROM space contains alternating regions of validity and invalidity, a simple binary search could converge on a boundary that does not reflect actual physical feasibility (i.e. the nearest boundary from the starting position).

The step size for the initial search was set to 10°, offering a balance between accuracy and computational efficiency.

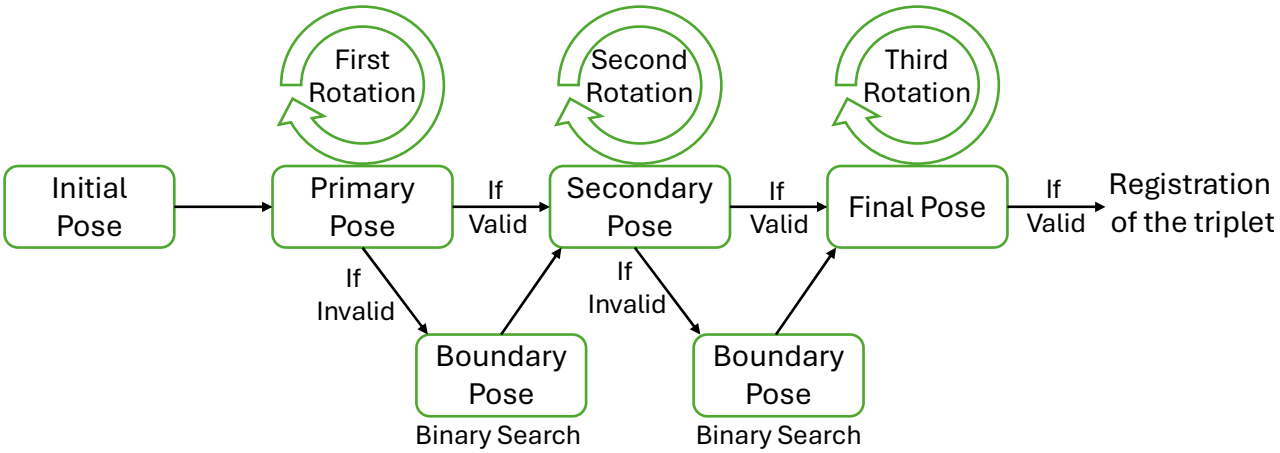

Figure 3.10: Flow diagram of the search algorithm. The algorithm begins at the initial pose and performs sequential rotations around three axes. For each rotation, it evaluates the constraints. Upon reaching an invalid configuration, the loop is terminated and a binary search is initiated to determine the boundary. Valid angle triplets are registered and used to map the feasible ROM space.

3.3.2 Algorithmic Advantages

This hierarchical search algorithm provides an efficient strategy for mapping the GH ROM. By evaluating configurations in a nested sequence of rotations, it allows early termination when constraints are violated, which avoids unnecessary computations in invalid regions.

A fixed step size of 10° is used during the coarse search phase, offering a robust trade-off between anatomical coverage and computational cost. Larger steps risk skipping over narrow invalid regions, while smaller ones significantly increase runtime. At each detected boundary, a binary search refines the transition zone with a precision of 0.5°, typically converging within eight iterations. This localized refinement ensures accurate detection of ROM limits without a full exhaustive search.

The worst-case computational complexity of the algorithm is $\mathcal{O}(n^3)$, where n is the number of steps per axis. However, early exits and the localized nature of the binary search ($\mathcal{O}(n \log n)$) reduce the practical runtime considerably. By focusing computation near critical constraint boundaries, the algorithm maintains both efficiency and anatomical precision.

3.3.3 Conclusion

This algorithm provides a computationally efficient and anatomically accurate method to estimate the humeral ROM. By combining coarse exploration with refined boundary detection, it captures constraint boundaries with high precision while limiting unnecessary computations. The approach returns a set of valid joint configurations that satisfy anatomical constraints, forming a patient-specific representation of the feasible ROM space. Its structure ensures both numerical robustness and clinical interpretability, making it well-suited for applications in joint analysis and other clinical applications.

3.4 Rotation Decomposition and Search Space

To simulate humeral motion, it is necessary to define how rotations are applied and combined. In this context, an Euler-Cardan decomposition is used to express joint motion as a sequence of three ordered rotations around anatomical axes. However, multiple decomposition orders exist, and the choice of rotation sequence can influence both the numerical behavior of the simulation and its interpretability.

This section reviews common decomposition sequences used in shoulder biomechanics and discusses the rationale behind the one selected for this study. In particular, it addresses the trade-off between avoiding singularities (such as Gimbal lock) and ensuring anatomical clarity in motion interpretation.

Several decomposition orders are used in the literature [39]:

- ISB's recommended Euler sequence: Y-X-Y
- Cardan: abduction followed by flexion and then axial: X-Z-Y
- Cardan: flexion followed by abduction and the axial: Z-X-Y
- Cardan: axial rotation followed by abduction (even though no longer a true abduction anymore) and then flexion: Y-X-Z

Two main factors influence the choice of rotation order: the risk of Gimbal lock and interpretability.

Gimbal lock refers to the loss of a degree of freedom in a rotation system when two axes become aligned. To mitigate this, the ISB recommends selecting the first axis from an external reference frame

(e.g., the scapular frame) [6]. This strategy helps to prevent alignment-induced singularities during simulation.

Interpretability is prioritized in this study, as the end users are clinicians accustomed to anatomical rather than mechanical movements. For this reason, quaternions were avoided. The selected decomposition should allow clinicians to understand and translate joint motion intuitively.

In this work, interpretability takes precedence over theoretical risks of Gimbal lock, which are less problematic in a forward kinematics context. Two decomposition sequences were studied: Ys-Xh-Zh and Yh-Xh-Zh. The first rotation being axial was found to be the most clinically meaningful. As shown in Figure 3.11, neither sequence presented missing values in the search space, suggesting that Gimbal lock did not manifest in practice.

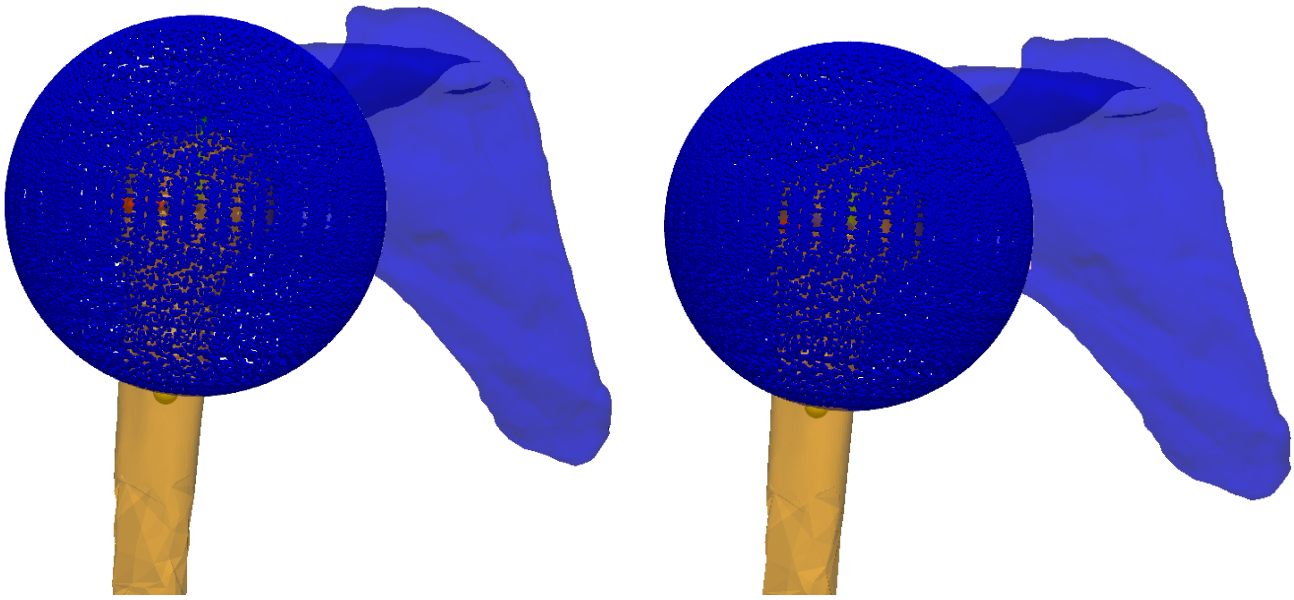

(a) **Yh-Xh-Zh** decomposition: axial rotation as the first movement.

(b) **Ys-Xh-Zh** decomposition: scapular axis as the first one.

Figure 3.11: Comparison of two Cardan decompositions applied to the GH joint. Both decompositions yield complete and continuous search spaces, indicating that Gimbal lock did not occur in practice. (Patient 1)

This reduced risk and impact of Gimbal lock can be explained by:

- In forward kinematics, even when axes align (e.g., Zh aligns with Ys/h), the resulting motion remains distinguishable since the anatomical effects differ (axial vs. flexion). Thus, even if the reference frame enters a Gimbal lock configuration (which could be problematic in inverse kinematics) the resulting 3D transformation remains mechanically meaningful.
- Cardan decomposition yields potential Gimbal lock at $X = \pm 90°$. Since $-90°$ implies extreme adduction (non-anatomical) and $+90°$ lies at the limit of abduction (excluding scapulohumeral rhythm), these extremes are rarely reached and are linked to "near boundary" positions.

Although choosing Ys as the first axis matches current biomechanical conventions, its adoption is unnecessary here, as Gimbal lock was not encountered. The Yh-Xh-Zh decomposition is retained for its interpretability. Future work could easily implement alternative orders.

3.4.1 Corrected Search Space

Since no constraint currently limits extension appropriately, the Zh values are limited to 60° in extension. This choice excludes hyperlaxity or pathological mobility but still allows representation of the normal ROM.

In addition to limiting extension (Z+) to 60°, additional constraints were applied to the other axes to restrict the exploration to physiologically plausible and clinically relevant motion ranges. These boundaries were not enforced by anatomical constraints in the model itself, but were introduced to reduce computational load and focus the analysis on functional ranges of motion:

- X is limited to $[-60°, 90°]$.
- Y is limited to $[-90°, 90°]$.
- Z is limited to $[-90°, 60°]$.

These cutoffs ensure that the ROM estimation remains focused on ranges that are biomechanically meaningful and commonly encountered in clinical contexts. The boundaries are also sign-dependent and specific to a left shoulder; adaptation to a right shoulder requires appropriate sign reversal.

The final corrected search space is presented in Figure 3.12.

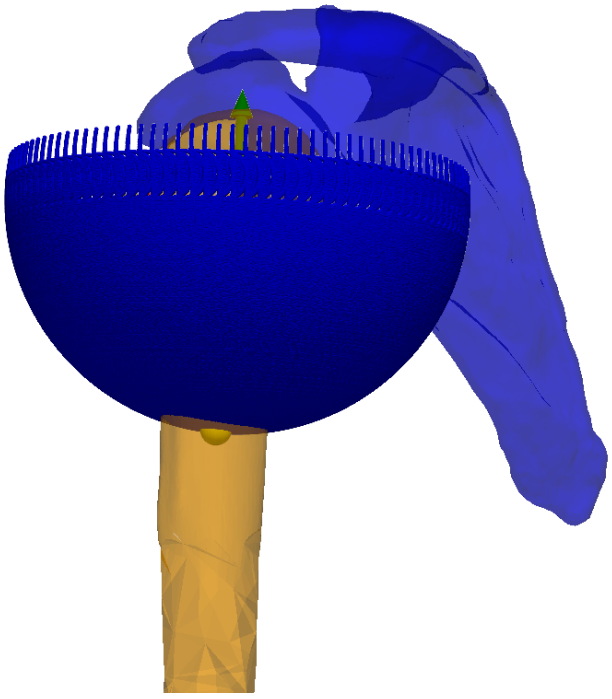

Figure 3.12: Corrected search space for GH joint exploration, showing sampled positions within bounded ranges on the Xh, Yh, and Zh axes. (Patient 1)

3.4.2 Conclusion

The selected Yh–Xh–Zh decomposition offers a clinically intuitive description of shoulder motion and avoids the risk of Gimbal lock under the tested configurations. Its use supports anatomically meaningful interpretation of simulated joint positions, especially for clinical end users. In parallel, applying physiological limits to the search space helps focus the analysis on functional ranges of motion while reducing

computational effort. Together, these choices define a stable and interpretable framework for exploring the GH ROM.

3.5 Computational Optimization Strategy

To ensure the computational feasibility of the simulations while maintaining the accuracy of the results, several optimization strategies are implemented. These strategies focus on reducing mesh complexity, minimizing memory usage, and limiting redundant operations during geometry processing. Particular attention is paid to preserving the biomechanical integrity of the anatomical regions involved in the ROM analysis.

Whenever possible, built-in functionalities from the `trimesh` library are used. These modules offer efficient, vectorized operations that leverage the underlying structure of mesh objects, including precomputed connectivity, bounding volume hierarchies, and cached geometrical properties. By exploiting these capabilities, operations such as collision detection, proximity queries, and ray-based intersection tests are executed with minimal overhead.

Another important optimization involves working with localized submeshes when only a portion of the anatomy is relevant for a given computation. For example, when assessing COV or extracting the articular surface of the humerus, a custom function is used to isolate a closed subregion of the full mesh based on a manually defined loop of points. This function relies on the `vtkSelectPolyData` module from the Visualization Toolkit (VTK), which is well-suited for topological segmentation on surface meshes. Internally, VTK computes the smallest region enclosed by the loop by projecting it onto the mesh surface and extracting the corresponding triangle subset [40]. The resulting reduced mesh allows for more efficient intersection tests and projection-based analyses by restricting computations to a small and relevant portion of the geometry.

Global mesh simplification is also applied to reduce the resolution of anatomically less relevant regions while preserving detail in areas of interest. Specifically, the humerus mesh is divided into two parts: a high-resolution proximal region (i.e., humeral head and upper shaft) and a distal region targeted for decimation. Only the distal part undergoes simplification, while the preserved region remains untouched. This simplification is performed using a surface-preserving algorithm from the PyVista library, which reduces the number of faces while maintaining the overall shape and curvature of the surface. The final mesh is a concatenation of both parts, significantly reducing computational load while maintaining anatomical accuracy in functionally critical regions. An example of the resulting downsampled mesh is shown in Figure 3.13.

Figure 3.13: Humerus mesh after selective simplification. The proximal region, including the humeral head and upper shaft, is preserved at high resolution, while the distal region is downsampled using PyVista's `decimate_pro`. This targeted simplification reduces computational demands while preserving anatomical detail in regions critical for joint function. (Patient 1)

Together, these optimizations reduce computation time throughout the pipeline without compromising the anatomical or functional quality of the results. They also improve scalability, allowing the proposed method to be applied efficiently across multiple patient-specific datasets.

3.6 Representation

After computing the set of anatomically valid joint configurations, it becomes essential to translate these data into representations that are both interpretable and clinically meaningful. Due to the high dimensionality of the rotation space and the complexity of constraint interactions, direct visualization of the full ROM is not practical. Instead, targeted representations are required to reveal the structure of the solution space, highlight constraint effects, and support anatomical interpretation.

To address these needs, three complementary representations are developed: a spatial mapping of valid joint positions, a sensitivity analysis of the constraints applied, and a projection onto anatomical planes to reconstruct clinically relevant movements.

3.6.1 Solution Space Visualization

A direct 3D plot of all humerus mesh positions would be uninterpretable due to excessive visual overlap, which led to a cluttered and unreadable representation. To overcome this, a reference point located at the center of the midshaft of the humerus is selected. This point is tracked across all valid positions and displayed in 3D space on top of the initial meshes, creating a spatial envelope that reflects the extent of the ROM without overwhelming visuals (example in Figures 4.1).

To explore this representation interactively, individual points within the solution space can be selected by the user. Upon selection, the associated humerus poses is displayed in a second window, along with the local anatomical reference frame. Additionally, the associated angle triplet is printed. This enables detailed inspection and manual verification of specific joint configurations. Points may also be manually excluded from the solution set if they seem anatomically implausible or if residual numerical artifacts are

detected. This feature provides flexibility for limited post-processing in cases where automatic filtering may be insufficient.

3.6.2 Constraint Sensitivity Mapping

A second representation focuses on the sensitivity of the solution space to threshold variations in key constraints. In particular, the AHD, CHD, and COV are highly dependent on defined thresholds. As such, modifying these thresholds could lead to deeply different ROM envelopes.

To visualize this effect without rerunning simulations for each threshold, a color-mapped ROM space is generated (example in Figures 4.6). Each valid configuration is colored according to the most restrictive threshold under which it would still be retained. Points that pass all thresholds are shown in green, while those that fail the next tighter threshold are shown in red. Intermediate thresholds are encoded in gradient colors from green to yellow, orange, and finally red (representing increasing restrictiveness). This approach enables visualization of the constraint's regional influence and how constraint thresholds affects the ROM.

In the rest of this study, threshold values are chosen based on reported standard deviations in the literature:

- AHD thresholds: [4.5, 6.0, 7.5, 9.0] mm for males and [3.5, 5.0, 6.5, 8.0] mm for females, using a 1.5 mm increment based on [27], [28].
- CHD thresholds: [8.0, 9.5, 11.0, 12.5] mm for males and [7.0, 8.5, 10.0, 11.5] mm for females, also spaced by 1.5 mm following [30], [41].
- COV thresholds: [15, 16.5, 18.0, 19.5]% for males and [13.5, 15.0, 16.5, 18.0]% for females, defined for consistency with the other metrics in the absence of validated standards.

However, users may define custom threshold sets if clinically justified.

Initially, each configuration is evaluated independently, i.e. its color reflects only its local feasibility with respect to the constraints. This approach is particularly well-suited for clinical applications. It allows practitioners to quickly identify vulnerable regions of the ROM and to understand how changes in threshold values could affect the acceptability of specific configurations.

To complement this clinically oriented tool, a second implementation was developed to model the propagation of constraint violations along movement trajectories. This version introduces an inheritance mechanism: once a constraint is violated at the start of a movement sequence, all subsequent positions along that trajectory inherit the classification, even if their individual values would otherwise be acceptable. While this approach more accurately reflects how stricter thresholds will impact the ROM envelope, it relies heavily on the specific motion decomposition used in the simulation. Since the simulated trajectories do not necessarily reflect physiologically realistic paths, the resulting color maps are less clinically interpretable. Rather than improving clinical relevance, this version is more useful as a technical tool to anticipate how the algorithm responds to threshold changes across connected configurations.

As with the original mapping, individual configurations remain selectable in both versions. This allows users to inspect or remove specific outliers based on updated thresholds. Additionally, for each selected point, the corresponding AHD, CHD, and COV values are printed for detailed evaluation.

For this study, the original mapping approach was retained. It offers better alignment with clinical interpretation, avoids confounding due to artificial motion paths, and allows for a clearer understanding of how each constraint acts locally. Despite its position-wise independence, it still provides a valuable visual approximation of how the ROM envelope would evolve under stricter or more lenient thresholds. The inheritance-based implementation remains a feature that could motivate future developments.

3.6.3 Anatomical Movement Translation

Given that Euler-Cardan decompositions do not directly correspond to anatomical movements, a third representation is available to increase the interpretability of the results from a clinical perspective (example in Figures 4.7). This involves mapping the ROM data onto anatomically meaningful planes and reconstructing movement amplitudes accordingly.

Several anatomical planes were defined based on common clinical motion categories—such as the frontal plane for abduction or the scapular plane for scapular-plane elevation. Rather than restricting analysis to points lying exactly within these planes (which would be sparse or nonexistent due to discretization), a slicing strategy is employed: all positions falling within a narrow angular window around the plane of interest are included.

To quantify movement within each slice, a vector is computed from the center of the humeral head to a reference point on the humeral shaft. The angle between this vector in the rest position and in the current pose defines the movement amplitude. For each slice, the maximum and minimum amplitudes are reported. This enables ROM analysis in terms that are familiar and interpretable to clinicians, such as the achievable range of abduction or flexion.

An illustration of this computation is provided in Figure 3.14, which shows how angular amplitude is measured for both a flexion and an adduction movement. The HA defines the orientation used for the angle computation.

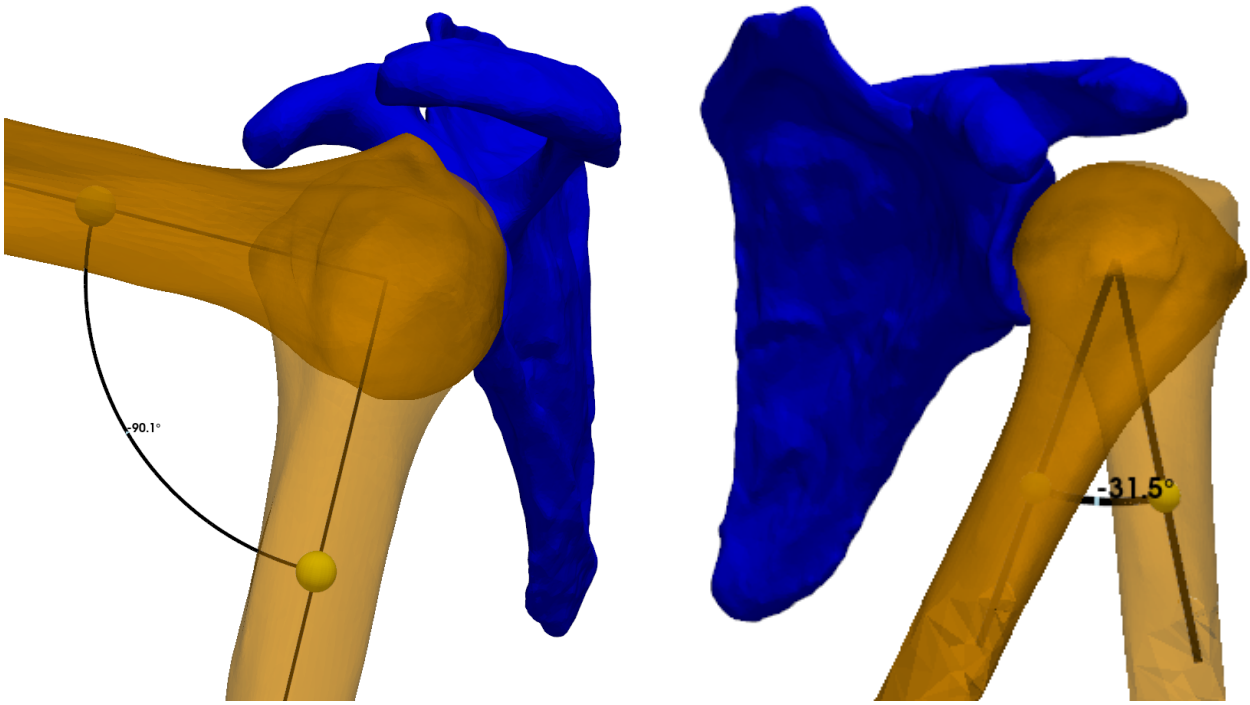

(a) Flexion movement (b) Adduction movement

Figure 3.14: Illustration of movement amplitude computation for Patient 1. A vector from the humeral head center to the shaft defines the orientation. Angular distance relative to the rest position is used to quantify motion.

3.6.4 Conclusion

Together, these three representations provide complementary perspectives on the computed ROM space. The spatial mapping offers an overview of feasible humeral displacements, the constraint sensitivity visualization reveals the influence of clinical thresholds on joint mobility, and the anatomical reconstruction translates mechanical outputs into clinically meaningful movements. These visualizations enhance clinical interpretability and clarify how constraint interactions define joint motion in each patient.

Chapter 4

Results

This chapter presents the results of the ROM analysis. It includes an overview of the analyzed dataset, a characterization of the global solution space, an evaluation of constraint sensitivity, and a projection of motion amplitudes onto clinically relevant anatomical planes. Both qualitative and quantitative observations are presented, with comparison across multiple patients.

4.1 Dataset

Table 4.1 summarizes the datasets used in this study, including demographic data, shoulder side, clinical condition, and anatomical completeness. All selected CT scans reflect common clinical imaging protocols and are chosen based on their overall quality. HSD cases are selected to ensure that the defects have a sufficient size and are clearly visible, enabling a reliable assessment of their influence on joint mobility.

The five patients are selected to reflect anatomical and pathological variability rather than one representative and common case. The dataset includes three male patients (one healthy, one with combined HSD and BBL, and one with combined HSD and a minor BBL) as well as two female patients (one healthy and one with combined HSD and BBL). Patients are annotated from 1 to 5. Patient 1 serves as the reference case and is used to illustrate the main results throughout this chapter. Results for Patients 2 to 5 are provided in Appendix A to support comparative analysis.

Table 4.1: Summary of the patient datasets used for ROM estimation. HSD = Hill-Sachs defect. BBL = bony Bankart lesion.

Patient	Sex	Age	Side	Condition	Usage	Dataset Notes
1	M	66	L	Healthy	Reference Case	Distal humerus available
2	M	20	L	HSD and BBL	A.1	No distal humerus
3	M	26	L	HSD and minor BBL	A.2	No distal humerus
4	F	63	L	Healthy	A.3	Distal humerus available
5	F	19	L	HSD and BBL	A.4	No distal humerus

Although the initial translation step could be applied to further standardize joint alignment, it is intentionally omitted here. The rotational alignment is mandatory to ensure reproducibility and comparability across patients, even though it modifies the relative pose of the humeral head and glenoid to some extent. In contrast, the additional in-plane translation has a minimal effect in this dataset, with displacements below 2 mm in all cases. Since this small displacement does not significantly affect comparisons between patients, the translation is omitted to avoid further altering the native joint configuration captured in the CT scans and to better preserve subject-specific anatomical features.

To further characterize the starting configurations, Table 4.2 reports the initial values of three key anatomical constraints: AHD, CHD, and COV.

Table 4.2: Initial values of anatomical constraints. AHD = Acromio-Humeral Distance. CHD = Coracoid-Humeral Distance. COV = Glenoid coverage.

Patient	**AHD [mm]**	**CHD [mm]**	**COV [-]**
1	10.21	11.49	0.24
2	7.97	13.87	0.22
3	8.05	12.85	0.20
4	8.62	7.46	0.18
5	6.02	7.50	0.16

As shown in Table 4.2, the reference patient Patient1 exhibits the largest acromio-humeral distance and COV ratio, consistent with a healthy male shoulder. Similarly, Patient4, who is also healthy, presents lower values that remain coherent with female anatomical norms. Patients with combined defects (e.g., 2, 3, and 5) generally show reduced AHD values, indicating a small subacromial clearance. Notably, Patient 5, who combines pathological features with expected female morphology, presents the lowest AHD and COV values overall, suggesting a more pronounced alteration of joint geometry that could significantly influence ROM.

4.2 Solution Space

The overall shape of the solution space is consistent across all patients and resembles a truncated sphere. This geometry aligns with the anatomical assumption of the GH joint acting as a ball-and-socket articulation, without any translational motion.

Two main features are consistently observed. First, in the frontal view (Figure 4.1a), a noticeable asymmetry is observed: the medial boundary is inclined relative to the vertical axis, meaning that more medial arm positions correspond to lower vertical elevations. This pattern reflects the expected reduction in elevation during adduction, particularly when scapular motion is not modeled.

Second, in the lateral view (Figure 4.1b), flexion movements consistently exhibits higher amplitude than extension movements. The amplitude gradually decreased from anterior to posterior, with a local minimum typically found in the mid-posterior region, followed by a slight increase toward the extension limit.

These spatial characteristics were present across all patients (with different amplitudes), although specific individual deviations were noted:

1. Patient 1 shows a subtle deviation in the antero-medial quadrant (left side of the frontal view in Figure 4.1a), where a small triangular region of higher amplitude is observed before a drop in elevation. This deviation is minor and does not affect the general trends.

2. Patient 2 displays a prominent void in the lateral view (FigureA.1b), characterized by a sharp decrease in ROM following flexion, before increasing again toward extension. This deep drop in the mid-range contrasts with the smoother transition observed in healthy cases and is attributed to the large BBL.

3. Patient 3 does not present the expected local minimum between flexion and extension (Figure A.4b). Instead, the area is filled with sparsely distributed solutions that likely result from suboptimal threshold values in the applied constraints. These configurations should be filtered out during post-processing (see Section 3.6.1).

4. Patient 4 does not show any noteworthy deviation from the general spatial trends.

5. Patient 5 exhibits the most restricted ROM. In the frontal view (Figure A.10a), a notable void appears between the lateral and medial regions. Given the extent of anatomical damage in this patient, this reduction in feasible joint space is expected.

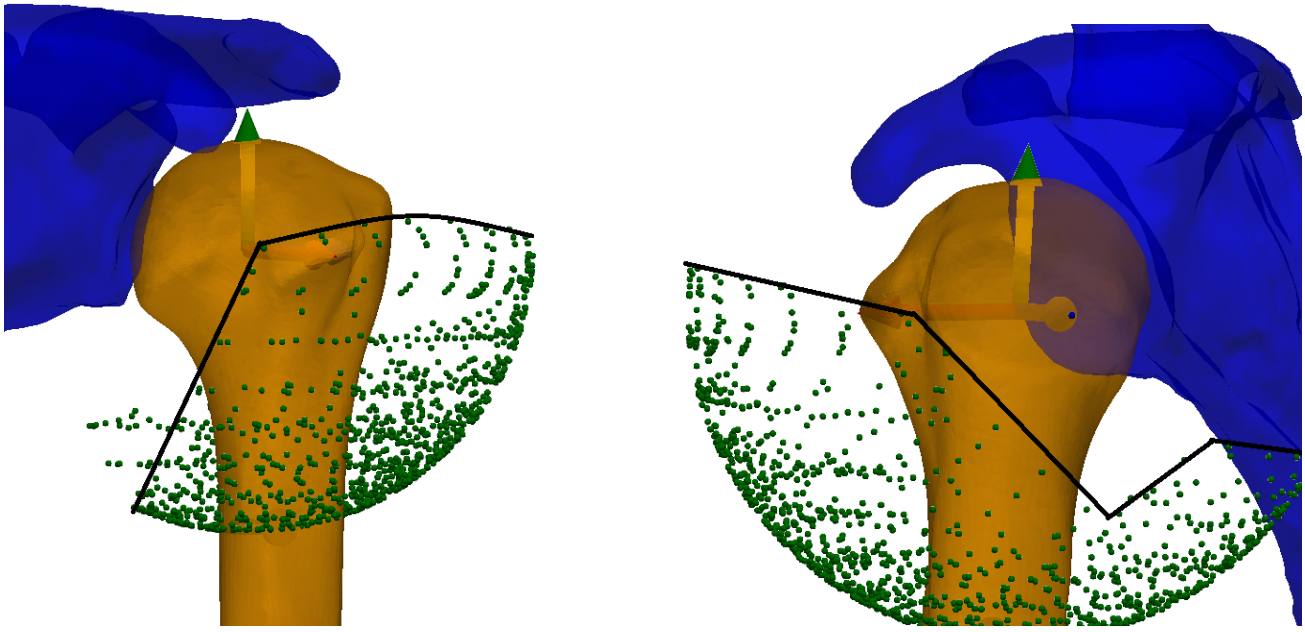

(a) Frontal view. Medial positions are on the left; lateral positions are on the right.

(b) Lateral view. Anterior positions are on the left; posterior positions are on the right.

Figure 4.1: Solution space from two perspectives. A black line highlights key geometric features of the ROM envelope. (Patient 1)

Table 4.3 summarizes the minimum, maximum, and total ROM values for each patient along the Xh, Yh, and Zh axes. Although the overall shapes of the solution space are similar, substantial inter-patient differences are observed in the amplitude of allowed motion. For example, the Xh-axis range varies from 70° (Patient 2) to 120° (Patient 3), with a mean of 106.56° and a standard deviation of 23.02°. Yh-rotation displays a comparable degree of variability (mean = 102.53°, std = 11.69°). In contrast, the Zh-axis range is identical across all patients (mean = 150°, std = 0°), likely due to the predefined algorithmic limits on the search space (Corrected Search Space Section 3.4.1). These results show that while the general motion envelope shape is preserved, the ROM amplitude is patient-specific.

Axis	Patient 1	Patient 2	Patient 3	Patient 4	Patient 5	**Mean**	**Std**
Min X	-60.00°	-34.06°	-30.31°	-60.00°	-44.69°	-45.81°	12.51°
Max X	48.44°	36.25°	90.00°	78.44°	50.63°	60.75°	20.11°
Range X	108.44°	70.31°	120.31°	138.44°	95.32°	106.56°	23.02°
Min Y	-62.50°	-79.69°	-70.31°	-50.31°	-56.88°	-63.94°	10.26°
Max Y	56.56°	8.13°	34.38°	59.75°	33.13°	38.39°	18.96°
Range Y	119.06°	87.82°	104.69°	110.06°	90.01°	102.53°	11.69°
Min Z	-90.00°	-90.00°	-90.00°	-90.00°	-90.00°	-90.00°	0.00°
Max Z	60.00°	60.00°	60.00°	60.00°	60.00°	60.00°	0.00°
Range Z	150.00°	150.00°	150.00°	150.00°	150.00°	150.00°	0.00°

Table 4.3: Range of motion limits across patients (P1–P5) in rotations along Xh, Yh, and Zh directions.

4.3 Constraint Sensitivity Mapping

Table 4.4 presents the number of times each constraint was triggered during ROM estimation. Importantly, these counts do not represent the number of rejected positions in the final solution space, but rather the number of *constraint violations encountered across all evaluated configurations*, including those tested during the intermediate steps of the binary search.

This distinction is essential, as the ROM search algorithm evaluates a high number of configurations, particularly near constraint boundaries. In such regions, constraint checks are performed at a finer resolution to precisely delineate the transition between valid and invalid motions. Therefore, the number of events gives insight into how frequently each criterion plays a limiting role throughout the search, even if those violations are not directly visualized.

As shown in Table 4.4, no constraint violations due to bone collision are detected across the five patients. This confirms that the combination of anatomical constraints is sufficient to prevent mesh interpenetration. Nevertheless, the collision check remains a critical component of the pipeline. It acts as a safeguard in case of future modifications, such as adjusted thresholds, anatomical outliers, changes in step size, or extensions of the model that introduce translational motion or relax other constraints. Additionally, it provides a formal verification step to ensure that all retained poses remain anatomically plausible.

Among the active constraints, COV is by far the most frequent cause of invalidation, accounting for approximately 63% of constraint events on average. This underscores the central role of joint stability in defining the functional ROM. AHD violations are the second most common, representing about 24% of constraint rejections, with increased prevalence in patients presenting reduced subacromial clearance. The CHD constraint is more heterogeneous across patients (entirely absent in Patient 2 and Patient 3, but dominant in Patient 4 (30.61%)) reflecting significant inter-individual differences in anterior joint clearance and coracoid proximity. Lastly, the X-axis orientation constraint consistently accounts for roughly 14% of rejected configurations.

These results highlight the complementary nature of the constraint set. COV enforces global joint stability, AHD and CHD prevent localized bony impingement, and the X-orientation constraint excludes physiologically unrealistic poses.

It is important to note that the reported number of constraint violations depends on the evaluation order implemented in the algorithm. Once a configuration is flagged as invalid by a constraint, subsequent

checks are skipped for that pose. As a result, earlier constraints in the evaluation sequence may appear more frequently, not necessarily because they are stricter, but because they are checked first. Although this ordering can affect the absolute counts, the relative trends observed across patients remain robust, and the dominant role of certain constraints (such as COV) remains evident regardless of the order.

# Events	Patient 1	Patient 2	Patient 3	Patient 4	Patient 5	**Mean**	**Std**
Collision	0 (0.00%)	0 (0.00%)	0 (0.00%)	0 (0.00%)	0 (0.00%)	0.0 (0.00%)	0.0 (0.00%)
COV	475 (56.21%)	295 (58.76%)	401 (62.27%)	446 (47.91%)	347 (49.29%)	392.8 (54.89%)	65.3 (5.50%)
AHD	163 (19.29%)	144 (28.69%)	182 (28.26%)	84 (9.02%)	153 (21.73%)	145.2 (21.39%)	33.1 (7.18%)
CHD	81 (9.59%)	0 (0.00%)	0 (0.00%)	285 (30.61%)	115 (16.34%)	96.2 (11.31%)	104.6 (11.46%)
X-orient.	126 (14.91%)	63 (12.55%)	61 (9.47%)	116 (12.46%)	89 (12.64%)	91.0 (12.41%)	26.6 (1.73%)
Total	845	502	644	931	704	725.2	150.7

Table 4.4: Number and percentage of events for each rejection criterion per patient (P1–P5). Percentages are relative to the total number of events per patient.

4.3.1 Acromiohumeral Distance (AHD)

The spatial distribution of AHD constraint violations reveals two main regions of interest in the solution space:

1. A superior region where more violations occur at high elevation angles, particularly during abduction. In these regions, the humeral tuberosities approach the acromion (see Figure 4.2a), leading to a decrease in subacromial space and frequent constraint violations. This consistently separates the ROM space into an inferior domain with fewer violations and a superior domain with more frequent constraint triggers.
2. A central region of increased constraint sensitivity appears for specific axial rotations, where alignment between the tuberosities and the acromion leads to a more rapid reduction in acromiohumeral distance (see Figure 4.2b). This produces a restricted central region flanked by two lateral regions with fewer constraint violations.

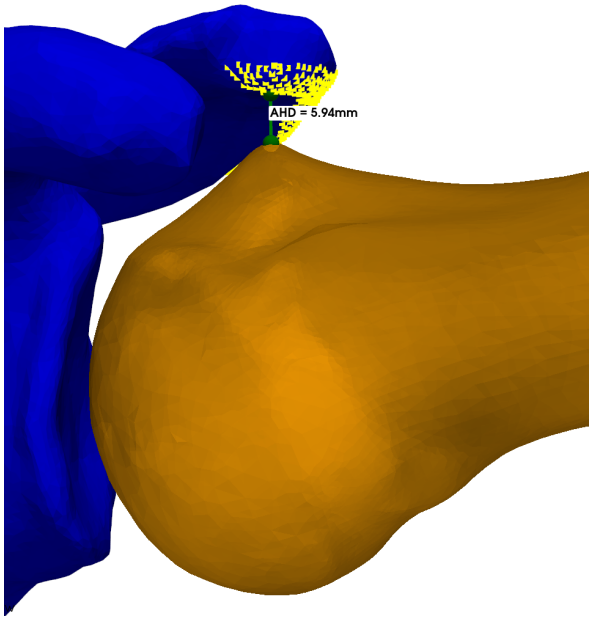

(a) Abduction at 78°, where the lower tuberosity approaches the acromion, reducing the AHD to 5.94 mm.

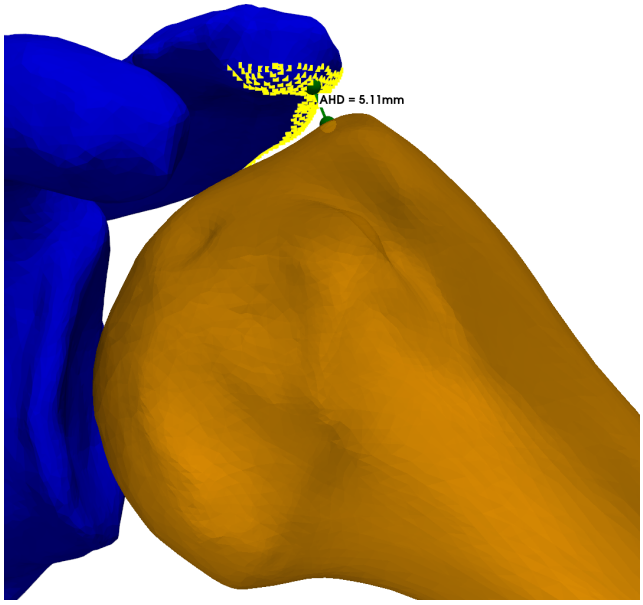

(b) Low abduction (30°) with axial rotation bringing the greater tuberosity in front of the acromion, resulting in a reduced AHD of 5.11 mm.

Figure 4.2: Illustrative joint configurations resulting in small acromiohumeral distances (AHD). (Patient 1)

Another observation is the presence of local minima during one-dimensional exploration, such as successive rotations around the Xh axis. These local dips in AHD values result from the complex geometry of the proximal humerus: the structure may initially approach the acromion, reach a minimum distance, and then move away. This leads to a non-monotonic AHD profile, as illustrated in Figure 4.3.

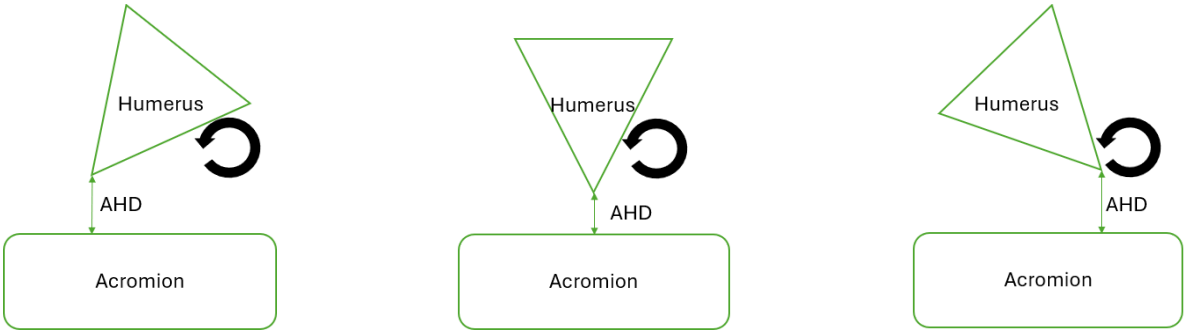

(a) Decreasing AHD (b) Minimal AHD (c) Increasing AHD

Figure 4.3: Illustration of a local minimum in the AHD profile during a continuous rotation sequence. The humerus approaches the acromion (a), reaches a minimum AHD (b), and then moves away (c).

In terms of inter-patient variation, Patient 2, Patient 3, and Patient 5 exhibit mappings with fewer green points, indicating that their subacromial space is small. In contrast, Patient 1 and Patient 4 show broader green zones, suggesting larger subacromial clearance.

In conclusion, the AHD constraint primarily limits movements involving superior elevation, such as abduction and forward flexion. Its effect is modulated by axial rotation: when the tuberosities are oriented toward the acromion, the constraint becomes more restrictive, illustrating the geometric coupling between axial orientation and subacromial clearance.

4.3.2 Coracohumeral Distance (CHD)

The CHD constraint spatially divides the solution space into two major regions: anterior and posterior. In the posterior half (Figure 4.6b), CHD values tend to be relatively uniform. In contrast, the anterior region is more heterogeneous and contains the lowest CHD values across all patients. This anterior–posterior asymmetry can be described by several geometric observations (see Figure 4.4 for illustrations):

1. **Anterior location of the coracoid:** In configurations where a large humeral structure (e.g. a tuberosity or the articular surface) is located anteriorly, the CHD tends to decrease sharply due to reduced clearance with the coracoid. The specific structure responsible for this proximity varies across patients. As a result, some patients exhibit high densities of red points in the anterior region, while others show a similar pattern posteriorly. However, one of the two regions consistently exhibits concentrated CHD violations, reflecting a systematic spatial sensitivity in the constraint map.
2. **Geometry of the proximal humerus:** The humeral head is smooth and less prominent, which results in gradual CHD changes when it is the nearest structure to the coracoid. In contrast, the tuberosities (particularly the lesser tuberosity) are more angular and protruding. When these face the coracoid, even small positional changes can result in sharp reductions in CHD, producing a heterogeneous and sensitive spatial pattern.
3. **Problematic structure dependency:** In posterior poses, CHD values remain relatively uniform and are primarily determined by the humeral head. In contrast, anterior configurations involve the tuberosities more frequently, resulting in distinct spatial profiles in the CHD mapping.

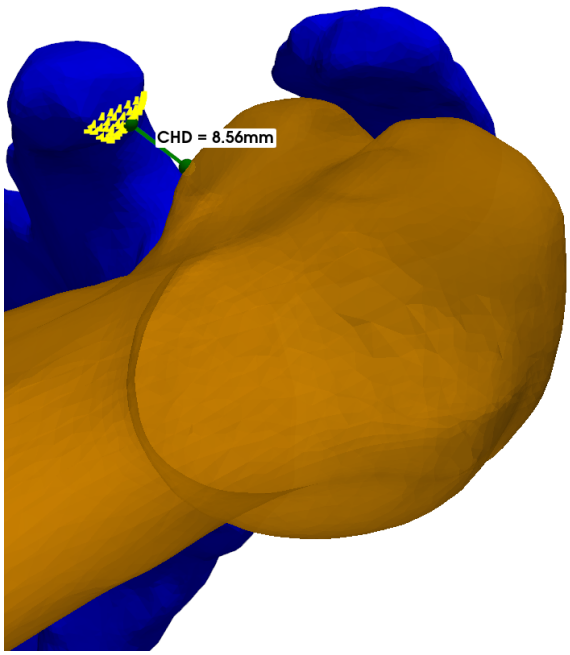

(a) Anterior configuration (flexion of 53°) with the lower tuberosity approaching the coracoid, reducing the CHD to 8.56 mm.

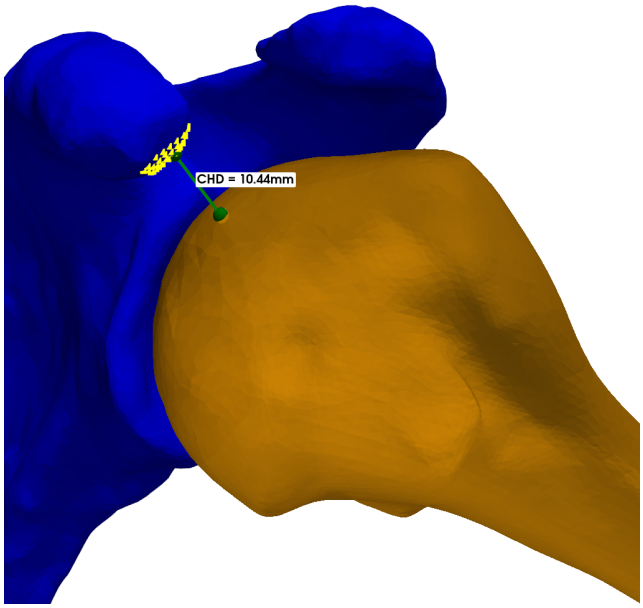

(b) Posterior configuration (extension of 66°) where the articular surface approaches the coracoid, reducing the CHD to 10.44 mm.

Figure 4.4: Examples of joint configurations leading to reduced coracohumeral distance (CHD). (Patient 1)

A consistent difference was observed between male and female patients. In male patients (Patient 1, Patient 2, Patient 3), the red points (i.e., severe constraint violations) were predominantly located in the

anterior region. In contrast, the female patients (Patient 4, Patient 5) exhibited red points primarily in posterior regions.

Another notable observation of the CHD constraint map is that its violations are not confined to the periphery of the ROM envelope (as with AHD or COV) but rather cluster within the central, anterior region of the solution space. These violations often occur near the neutral position and are strongly associated with axial rotations that orient the critical structure (either articular surface or tuberosity) toward the coracoid, leading to constraint failure even at modest elevations.

Conversely, the highest CHD values (green or yellow points) are rare near the initial pose and are typically found in the anterior-superior quadrant. These positions correspond to axial rotations that position the tuberosities between the acromion and the coracoid, such that elevation moves them *away* from the coracoid. In this configuration, the humeral neck (not the head or the tuberosities) is oriented toward the coracoid, and its concave geometry allows for greater clearance. In posterior movements, the coracoid faces the convex apex of the humeral head, leading to inherently smaller CHD values.

In terms of inter-patient variation, Patient 1, Patient 4, and Patient 5 exhibit mappings with fewer green points, suggesting a more restricted subcoracoid space. In contrast, Patient 2 and Patient 3 display broader regions of permissive CHD, indicating larger subcoracoid clearance.

In summary, two dominant spatial profiles emerge:

- Posterior movements: Characterized by smooth geometric transitions involving the humeral head, resulting in low but relatively uniform CHD values.
- Anterior movements: Characterized by heterogeneous and abrupt variations involving the tuberosities, with sharp gradients in CHD between neighboring configurations.

4.3.3 Glenoid Coverage (COV)

The COV constraint primarily acts at the boundaries of the solution space, dividing it between medial and lateral. While it occasionally also limits extreme abduction movements, its principal effect is to delineate configurations in which the humeral head loses sufficient glenoid containment, particularly in highly medial positions. As COV is a key factor for joint stability, these low-COV areas correspond to mechanically vulnerable zones.

Low COV is systematically associated with joint configurations in which the humeral neck (clearly visible in Figure 4.5c) engages with the rim of the glenoid, reducing the articular contact area. These extreme positions are linked to intrinsic instability and often occur at the limits of motion. Thus, the COV constraint plays a critical role in defining the boundaries of the ROM space, rather than affecting its internal bulk.

Several extreme abduction positions are also slightly limited by the COV constraint. However, the AHD constraint also applies in these configurations, and the more restrictive condition determines the final rejection. Notably, most extreme abduction poses are not classified as invalid by COV alone, indicating that AHD is the dominant constraint in this region. Moreover, the ROM search space was manually capped at 90° of positive Xh rotation, possibly preventing further progression into COV-limited territory. Therefore, although abduction could reasonably be constrained by both conditions, AHD remains the primary limiter under the current settings. An example of a configuration affected by both constraints is shown in Figure 4.5b.

Another important region is medial elevation, corresponding to the left side of the frontal solution space (as described in the first pattern of the Solution Space subsection). These positions were initially presumed to be restricted by CHD due to their proximity to the coracoid. However, comparison of the

constraint maps reveals that COV is the dominant limiting factor in this zone, as shown by a higher density of red points in the COV map. This is anatomically plausible (see Figure 4.5): medial elevations combine humeral adduction with upward motion, positioning the humeral head closer to the glenoid rim. In this configuration, the region of the humeral head that remains covered by the glenoid surface is reduced, increasing the instability. These positions are inherently less stable, as adduction already compromises containment, and further elevation exacerbates the loss of COV. In adjacent positions (near the coracoid) the COV improves slightly, but the CHD constraint becomes more restrictive. This interaction illustrates how constraint dominance can shift depending on local humeral orientation, and certain regions are limited by multiple overlapping mechanisms.

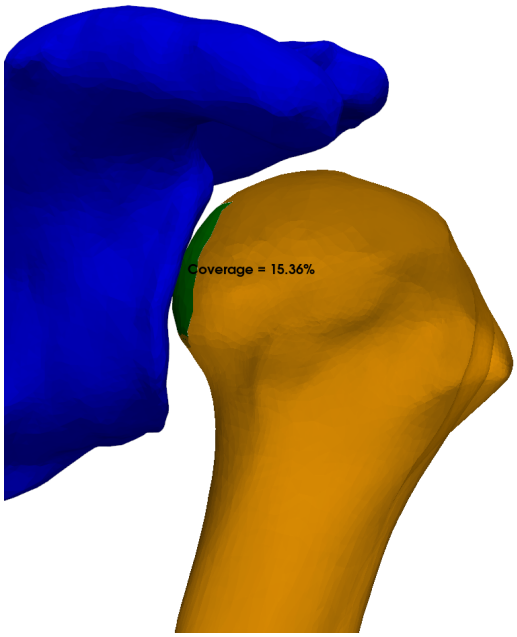

(a) Pure adduction of 30°, resulting in a low COV of 15.36%.

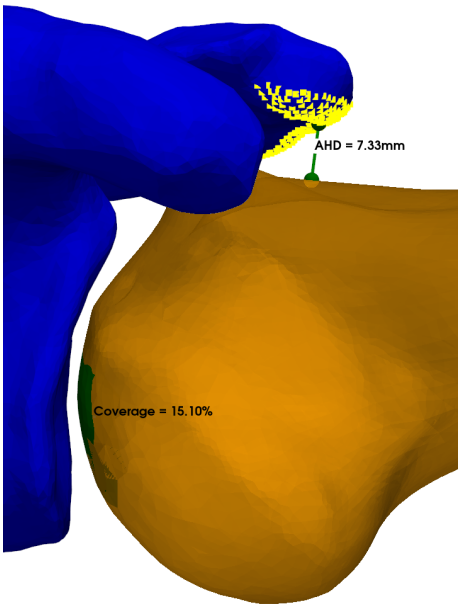

(b) Abduction of 85°, constrained by both COV (15.10%) and AHD (7.33 mm).

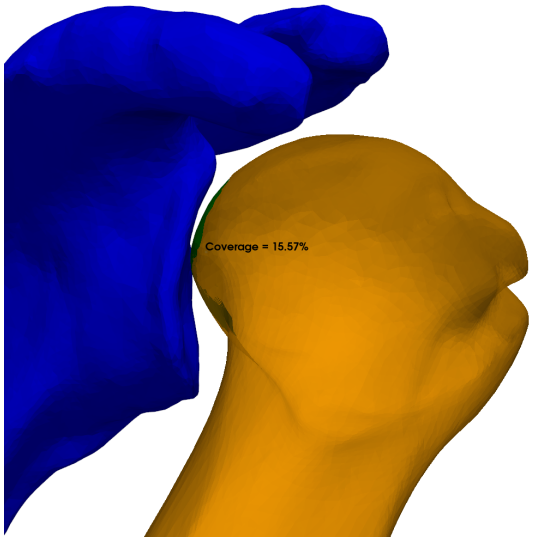

(c) Combined abduction and elevation (total angle: 58°), reducing COV to 15.57%.

Figure 4.5: Examples of joint configurations with reduced COV. (Patient 1)

From a patient-specific perspective, Patient 4 and Patient 5 exhibit highly saturated COV maps, with predominantly orange and red values. In the case of Patient 5, the presence of a large BBL results in a reduced glenoid surface area, leading to lower overall COV and confirming the expected link between BBL and mechanical instability. Interestingly, the relatively uniform distribution of color in female patients may suggest reduced variability in COV values compared to male patients. However, due to the small sample size, this potential sex-related difference should be interpreted with caution.

In summary, the COV constraint primarily limits the outer boundary of the ROM envelope and reflects the intrinsic stability of the GH joint. When it is not the dominant limiter, it is typically because another constraint (such as AHD or CHD) is more restrictive at that configuration. In some cases, such as extension movements, manual bounds on the search space may also prevent the COV constraint from activating.

Summary of Threshold Sensitivity The spatial mapping of constraint thresholds reveals that each condition contributes differently to the limitation of the ROM space, both in location and intensity. The AHD and COV constraints show relatively steep threshold gradients, with clearly defined transitions between permissive and restricted zones. This indicates a high sensitivity to threshold variation, particularly near the boundaries of abduction and medial elevation. In contrast, the CHD exhibits a more diffuse and heterogeneous response, especially in anterior regions where its impact depends heavily on fine variations in humeral geometry and axial rotation.

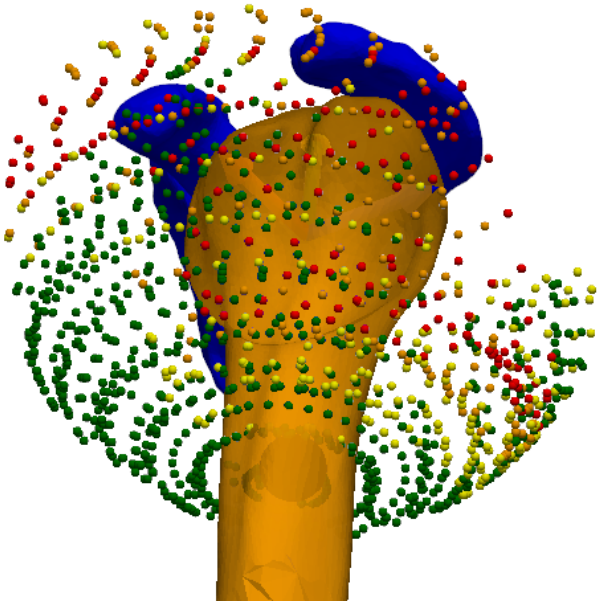

(a) Acromio-humeral distance (AHD) mapping. Red: 4.5–6 mm, orange: 6–7.5 mm, yellow: 7.5–9 mm, green: >9 mm.

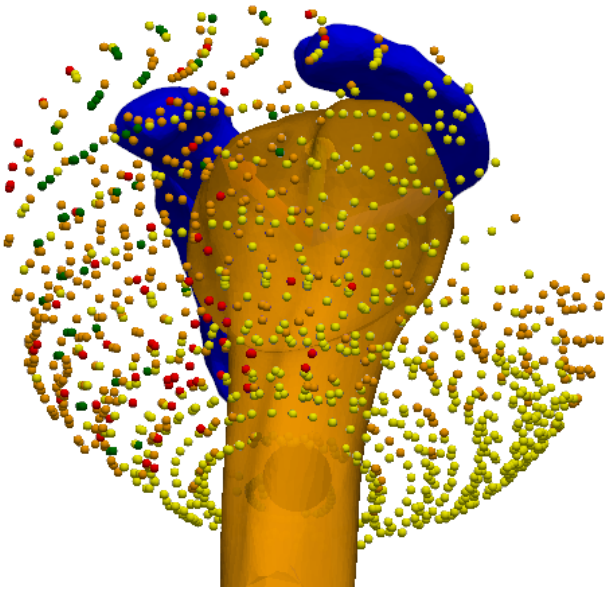

(b) Coraco-humeral distance (CHD) mapping. Red: 8–9.5 mm, orange: 9.5–11 mm, yellow: 11–12.5 mm, green: >12.5 mm.

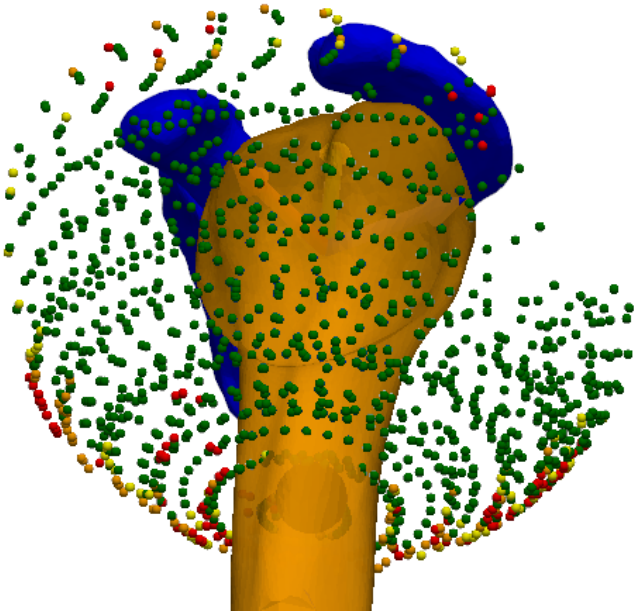

(c) Glenoid coverage (COV) mapping. Red: 15–16.5%, orange: 16.5–18%, yellow: 18–19.5%, green: >19.5%.

Figure 4.6: Constraint sensitivity mapping of the solution space for Patient 1. Subfigures show thresholds applied to (a) acromio-humeral distance (AHD), (b) coraco-humeral distance (CHD), and (c) glenoid coverage (COV).

4.4 Movement Amplitudes

To improve clinical interpretability, representative anatomical movements were extracted from the ROM solution space using planar slices. Each slice corresponds to a predefined motion category (pure abduction,

scapular abduction, or forward flexion) and includes all configurations falling within a narrow angular window around the target plane. Within each slice, movement amplitude was computed as the angle between the initial and terminal positions of the vector joining the humeral head center to a reference point on the shaft.

Figure 4.7 illustrates these valid configurations for Patient 1. The obtained subsets of the solution space form arc-like patterns, which is consistent with the underlying assumption of a ball-and-socket joint. The abduction–adduction (Figure 4.7a) and scapular abduction–adduction (Figure 4.7b) slices yield shorter arcs compared to the broader flexion–extension arc (Figure 4.7c).

From a patient-specific perspective, Patient 2 and Patient 5 exhibit noticeable voids in their abduction and scapular abduction maps, resulting in significantly reduced arc lengths. In contrast, their flexion maps appear less affected and show more complete arcs, similar in coverage to those of healthy patients. This confirms that forward flexion is generally more preserved in the presence of bony lesions, while abduction is more vulnerable to constraint-induced limitations.

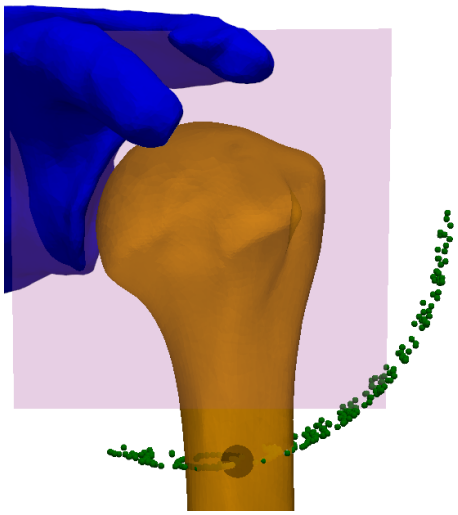

(a) Abduction-adduction solutions

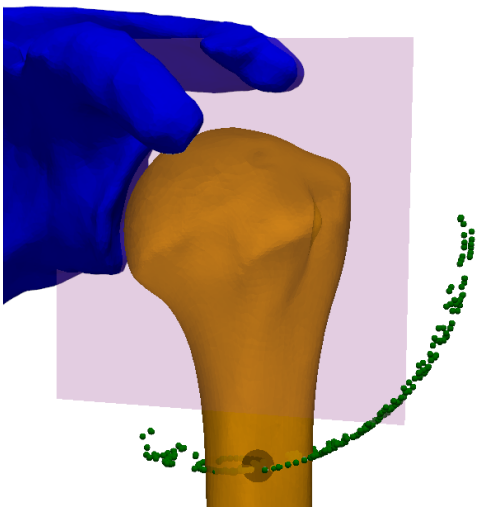

(b) Scapular abduction-adduction solutions

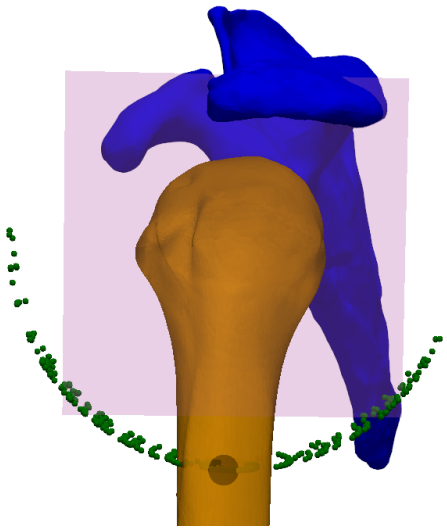

(c) Pure flexion-extension solutions

Figure 4.7: Planar motion slices for Patient 1. The purple plane defines the anatomical movement direction. Valid configurations (green) represent achievable positions within the defined slice.

Quantitative values for each patient are reported in Table 4.5. The measured range, minimum, and maximum angles are provided for frontal plane motion, scapular plane motion, and sagittal plane motion. Healthy patients (Patient 1 and Patient4) consistently exhibit larger ranges of motion. Patient 3, although affected by a Hill-Sachs defect, shows no significant glenoid-side involvement and therefore behaves similarly to a healthy joint from the algorithm's perspective.

In contrast, Patient 2 and Patient 5 present BBL that reduce the glenoid contact surface and lead to joint instability. Accordingly, these two patients demonstrate reduced ranges of motion across all movement categories.

The ranking of movement amplitudes across patients reveals consistent trends:

- **Abduction:** Patient1, Patient 4, and Patient 3 exhibit the largest ranges, whereas Patient 2 and Patient 5 show more restricted motion.
- **Scapular abduction:** Highest in Patient 1, Patient 3, and Patient 4; reduced in Patient 5 and Patient 2.
- **Flexion:** Greatest in Patient 4, followed by Patient 3 and Patient 1; lowest in Patient 2 and Patient 5.

Across the dataset, flexion consistently produced the largest motion amplitude (mean: 158.0° ± 9.4°), followed by scapular abduction (mean: 104.3° ± 17.1°), and finally pure abduction (mean: 101.3° ± 15.8°). No systematic dominance was observed between abduction and scapular abduction, with the dominant movement varying according to individual joint morphology and constraint distribution.

Movement	Patient 1	Patient 2	Patient 3	Patient 4	Patient 5	**Mean**	**Std**
Frontal Motion							
Max Adduction	-32.03°	-31.60°	-23.08°	-25.11°	-30.34°	-28.43°	3.64°
Max Abduction	82.80°	51.33°	91.50°	87.95°	50.52°	72.82°	18.09°
Range	114.82°	82.94°	114.58°	113.06°	80.86°	101.25°	15.83°
Scapular Motion							
Max Adduction	-32.22°	-31.56°	-21.91°	-23.32°	-23.75°	-26.55°	4.41°
Max Abduction	86.46°	39.59°	92.41°	88.07°	82.21°	77.75°	19.36°
Range	118.68°	71.15°	114.32°	111.39°	105.96°	104.30°	17.08°
Sagittal Motion							
Max Extension	-68.56°	-60.60°	-66.05°	-84.27°	-63.55°	-68.61°	8.27°
Max Flexion	90.10°	92.16°	93.69°	89.39°	81.63°	89.39°	4.17°
Range	158.66°	152.75°	159.75°	173.66°	145.18°	158.00°	9.39°

Table 4.5: Range of Motion (ROM), minimum, and maximum angles for abduction, scapular abduction, and flexion for each patient (P1–P5).

Chapter 5

Discussion

This chapter interprets the key results obtained from the GH ROM simulations performed across five patients. The objective is to contextualize the findings in light of anatomical expectations, clinical relevance, and modeling limitations. Particular attention is given to the influence of pathological features on joint mobility and constraint sensitivity. By comparing observed motion patterns and constraint interactions, this discussion aims to highlight both the robustness and the limitations of the proposed methodology.

Several consistent patterns emerged from the analysis. First, the overall solution space closely resembled a truncated sphere, reflecting the ball-and-socket nature of the GH joint. Second, the ROM boundaries were shaped by multiple anatomical constraints, each acting within distinct spatial zones. Third, inter-patient differences in ROM were strongly associated with pathological features, most notably the presence of BBL, which systematically reduced motion amplitudes and introduced discontinuities into the solution space.

5.1 Complementary Representations and Their Interpretive Power

This study employed three complementary representations to analyze the GH joint's ROM: the global ROM envelope, constraint mapping, and anatomical motion slicing. Together, these views provided a comprehensive understanding of both the extent and the underlying causes of motion limitations.

The ROM envelope offered a global view of the reachable positions, visually revealing voids, asymmetries, and motion biases. Constraint mapping then provided local explanations for these features by identifying which anatomical factors were responsible for invalid configurations. Finally, anatomical slicing projected the solution space into clinically familiar planes (frontal, sagittal, and scapular) translating abstract 3D results into interpretable motion amplitudes.

Importantly, these three perspectives were found to be consistent and mutually reinforcing. For example, local voids in the ROM envelope corresponded to regions of low constraint values and to missing solution in the anatomical motion slices. In this way, the framework not only enabled triangulation of findings but also ensured that mechanical limitations could be anatomically and clinically contextualized.

5.2 Patient-by-Patient Analysis

Patient-specific differences were clearly reflected across all three representations, demonstrating the model's ability to adapt to anatomical and pathological variability.

As expected, Patient 1 (Healthy Male – Reference Case) exhibited a large and continuous ROM

envelope, a low proportion of configurations close to constraint limits (i.e., low constraint saturation), and normal motion amplitudes across all planes.

Patient 2 (Male with BBL and HSD) showed marked ROM reduction, particularly in abduction and scapular abduction. The envelope presented voids near the superolateral edges, which were linked to low AHD values, indicating a low subacromial space. In the anatomical slices, motion arcs were severely truncated, especially in abduction, highlighting the compounded effects of dual pathology.

Patient 3 (Male with HSD with minor BBL) demonstrated a ROM envelope and amplitude range similar to those of Patient 1. This aligns with the fact that HSD, do not significantly impact constraint maps in the current model (They are not considered during ROM evaluation). Constraint event counts were low and scattered, and the anatomical slices formed complete arcs in all three planes, confirming that ROM preservation is likely in the absence of major glenoid-side defects. However, this patient required postprocessing to eliminate configurations initially classified as valid but that were later deemed unrealistic due to simultaneous near-threshold CHD and AHD values.

Patient 4 (Healthy Female) also exhibited a full ROM envelope and broad motion arcs. However, CHD mapping showed differences compared to Patient 1, with more posterior constraint events. This may reflect anatomical variation in humeral neck or coracoid morphology between sexes. Still, the functional outcomes remained comparable to the healthy male case.

Patient 5 (Female with BBL and HSD) presented the most constrained profile, with a reduced ROM envelope, high constraint saturation (particularly in COV mapping) and severely shortened arcs in anatomical motion planes. Interestingly, scapular abduction-adduction remained relatively preserved, while abduction-adduction and flexion-extension were significantly reduced. This pattern confirms that the model captures how defects influence ROM.

In conclusion, these patient-specific results support the clinical relevance of the proposed framework. The three-layered representation strategy provided both global and local insight into how pathologies manifest within the motion space. Moreover, the consistency across envelope shape, constraint location, and movement amplitude strengthens the results.

To further assess the realism of the motion amplitudes, results from the two healthy patients (Patient1 and Patient4) were compared to typical anatomical ranges reported in the literature. As expected, flexion, abduction, and scapular abduction values were all lower than standard norms. For instance, flexion-extension reached approximately 160°-175°, compared to a physiological range of 240° (180° flexion and 60° extension). Similar trends were observed for frontal and scapular plane motions, with measured ranges typically around 110°–120°, whereas full shoulder abduction-adduction can reach 180°–210° in healthy individuals [4]. This underestimation is primarily attributed to the absence of scapulohumeral rhythm modeling in the current framework. Indeed, scapular upward rotation contributes significantly to humeral elevation beyond 90°, and ignoring this motion results in a truncated arc of movement [5]. Although our values cannot be directly validated due to the small sample size and imaging modality limitations, they remain plausible: they are smaller than clinical norms (as expected) yet still exceed the 90° threshold at which scapular contribution becomes increasingly necessary. This suggests that our rigid, bony-only model did not artificially inflate motion estimates.

It is also important to emphasize that the anatomical motion planes (abduction, flexion, etc.) are used as the primary interpretive metric because they allow comparison with clinical literature. In contrast, raw Xh, Yh, and Zh rotation values (while fundamental to the algorithm) lack direct clinical analogues and are not commonly reported. To our knowledge, no prior study has systematically computed or validated GH ROM envelopes using a same approach as ours. Therefore, anatomical slicing was essential to bridge the gap between algorithmic output and clinically interpretable movement ranges.

5.3 Constraint Roles and Interactions

Each constraint in the framework played a distinct role in shaping the ROM envelope, with their effects distributed spatially in ways that mirror known anatomical and clinical behavior. Rather than acting uniformly, constraints exerted localized influences.

COV was the primary constraint responsible for limiting the stable ROM by ensuring stability of the joint configuration. This aligns with known patterns of GH instability, where loss of bony containment can lead to dislocation or subluxation. It particularly acted at the boundaries of the ROM envelope in highly medial positions, this is consistent with clinical observations that dislocations most frequently occur during fully extended or abducted positions. Across all patients, COV was also the most frequently triggered constraint, highlighting its dominant role in restricting extreme joint configurations. In several cases (including Patient 2 and Patient 5, where the glenoid surface was reduced) high constraint density in COV maps corresponded with reduced motion ranges and voids in the ROM envelope, further enforcing its role as a predictor of instability. Importantly, COV often acted in regions where other constraints were not triggered, confirming its complementary and boundary-defining function.

AHD was the main limiting factor for superior movements, particularly abduction and scapular-plane elevation. It frequently operated alongside COV, especially in lateral positions. In cases such as Patient 2, AHD violations contributed to superior voids that constrained abduction amplitudes. AHD was also responsible for local constraint saturation for specific axial rotations, confirming its directional sensitivity to certain bone structures.

CHD exhibited the most heterogeneous behavior across patients and directions. It often limited anterior movements (particularly in configurations involving tuberosity) but was less spatially consistent than AHD or COV. For example, CHD played a prominent role in constraining anterior poses in male patients, while posterior CHD saturation was more visible in females. This anterior–posterior asymmetry may reflect sex-based differences in the relative prominence or geometry of the humeral articular surface versus the tuberosities. In posterior configurations, the articular surface becomes the limiting structure. Whereas in anterior poses, it is the tuberosities that approach the coracoid more directly. However, given the small sample size, this trend should be interpreted with caution. CHD was especially useful in revealing "soft" limitations that might not lead to outright rejection but still indicated anatomical proximity to risky zones.

While not based on spatial proximity, the X-orientation constraint filtered implausible joint configurations by limiting the posterior tilt of the LT. Its effect was particularly relevant in posterior poses, where none of the distance-based constraints were active. Although this filter reduced the number of unrealistic configurations during extension, it was insufficient to prevent all implausible cases. As such, a manual boundary was applied to cap extension at 90°.

An important feature of the model is that no single constraint dominated across the entire ROM space. Instead, constraints operated in partially overlapping but distinct regions. This overlap was particularly relevant in complex anatomical cases: for example, Patient 5 displayed regions where both AHD and COV simultaneously limited motion. In contrast, extension movements lacked sufficient constraint activation altogether. Although CHD showed increased values (orange regions), it did not reach the smallest threshold, leaving the posterior envelope poorly defined. This led to the need for a manual limitation and also highlighted a key limitation of bony-only modeling: the absence of capsular or ligamentous resistance means certain movements can remain technically valid despite being physiologically implausible.

Taken together, the constraint system proved to be both complementary and clinically interpretable. Each constraint corresponds to a meaningful anatomical feature (such as subacromial space, glenoid containment, coracoid proximity, or humeral rotation) and their spatial interplay provides an intuitive framework for analyzing ROM in both healthy and pathological shoulders. However, limitations in extension modeling and the need for postprocessing in certain edge cases suggest that the current framework remains incomplete for fully capturing patient-specific variations.

5.4 Threshold Sensitivity and Patient-Specificity

A key consideration in constraint-based modeling is the selection of appropriate threshold values. In this study, thresholds were defined semi-empirically based on literature and anatomical reasoning, but their influence on ROM prediction was found to be highly non-linear and patient-dependent. Additionally, the results highlighted that even small changes in threshold values (within clinically reasonable bounds) can shift the location and extent of restricted motion.

No systematic correlation was observed between the initial values of constraint metrics and the optimal thresholds required to define anatomically valid ROMs. In other words, a patient with lower baseline CHD or AHD values did not necessarily require more permissive thresholds. While some trends were observable, the current sample size was too small to justify applying a systematic shift (e.g., a fixed offset) between initial values and final thresholds. This unpredictability suggests that anatomical variability (particularly in local bone morphology) affects not only the magnitude of constraint values, but also the *rate* at which they change with motion. As a result, threshold sensitivity is also tied to geometric context rather than raw distance measures alone.

For instance, in Patient 3, some configurations that technically passed the fixed thresholds were manually removed during post-processing due to their anatomical implausibility. This reflects a broader challenge: fixed thresholds can produce false-positive "valid" solutions in geometrically complex or borderline regions.

Despite these limitations, the ability to tune thresholds remains a strength of the framework. Depending on clinical objectives, more conservative or permissive ROM envelopes can be defined:

1. In preoperative planning, stricter thresholds may help simulate safer ranges that reduce dislocation risk.
2. In rehabilitation scenarios, more permissive thresholds could reflect recovery goals or capture borderline functional positions.

However, this flexibility also introduces methodological variability. When thresholds are adjusted manually on a case-by-case basis, transparent justification becomes essential to preserve reproducibility and clinical credibility. In this study, a uniform "one-size-fits-all" threshold set was ultimately selected. While this does not align with the goal of producing a fully patient-specific software, it enabled standardized comparisons across cases and was sufficient to explore the behavior of the framework.

Through iterative testing, we could be able to identify optimal threshold sets that produced consistent constraint maps for each individual patient. However, we found no systematic way to automate or optimize this process. Furthermore, the approach of minimizing map saturation is more meaningful in healthy joints, where the goal is to define a "true" ROM limit, than in pathological shoulders, where constraints may naturally cluster and restrict large regions.

One of the most sensitive and least standardized parameters in the model is the COV threshold. Unlike AHD or CHD, which are more documented and used, COV lacks reproducible definitions in the literature due to large methodological discrepancies, particularly the inclusion of the labrum and poorly described computation techniques. In our case, the concentric projection method was adopted, casting rays from the glenoid rim toward the humeral head center. This approach systematically underestimates COV but was intentionally selected to favor conservative stability assessments in the absence of a true contact model. An orthogonal projection method, for example, would likely overestimate the contact area by including points that are not mechanically engaged. While this underestimation provides a useful safety margin, it also means the empirical threshold (15% male / 13.5% female) cannot be generalized beyond the current setup. Furthermore, the threshold remains sensitive to the specific implementation, not the pose itself.

Until a standardized 3D computation protocol is adopted and validated against in vivo or intraoperative data, COV thresholds must be considered modeling assumptions rather than anatomical constants.

5.5 Limitations

While individual methodological limitations have been discussed throughout this document, several broader limitations affect the overall applicability and generalizability of the proposed framework.

5.5.1 Dataset Size

This study was conducted on five patient-specific cases selected for anatomical diversity and CT quality. While the sample includes a mix of healthy and pathological shoulders, it is insufficient to draw population-level conclusions. Observations such as sex-based differences in CHD behavior or glenoid surface variability cannot be confirmed without a larger cohort. As such, the present work should be regarded as a proof-of-concept demonstration of the model's capabilities and robustness.

The limited dataset also impacted the ability to generalize threshold-setting strategies. Although some trends were observable between initial constraint values and optimal thresholds, the sample size was too small to support reliable predictive modeling. As a result, thresholds were tuned manually and uniformly across cases, rather than being tailored through a data-driven or automated procedure.

In future work, increasing the number of patients will be critical to identifying whether statistically meaningful relationships exist between anatomical baselines and optimal constraint parameters. Such trends could eventually inform personalized threshold selection, leading toward a fully automated and individualized ROM estimation framework.

5.5.2 Image Modality and Soft Tissue Absence

All modeling in this study was performed from computed tomography (CT) scans, which provide excellent resolution for bony structures but no information about soft tissues. While CT remains the routine imaging modality in shoulder instability cases due to its accessibility and spatial accuracy, it inherently limits the ability to model key stabilizing structures such as cartilage, ligaments, and muscles.

This limitation impacts the framework in several ways:

1. A true patient-specific rest pose cannot be defined, as the equilibrium position depends on passive soft-tissue tension.
2. Passive soft-tissue constraints (such as capsular stiffness or rotator cuff impingement) must be approximated using bony surrogates like CHD and AHD.
3. Active or functional modeling, including simulations of muscle force or neuromuscular control, is not feasible in the current CT-based setup.

5.5.3 Manual Landmarking

All anatomical landmarks used for aligning bones, defining reference frames, or computing distances were manually selected. While care was taken to follow consistent criteria, this introduces user-dependency and potential reproducibility issues. Automating landmark selection via registration or machine learning could improve both repeatability and scalability.

5.5.4 Simplified Modeling of the Shoulder Kinematic Chain

The current framework models the GH joint in isolation, assuming pure rotation around a fixed center with the scapula treated as a static reference structure. While this simplification facilitates controlled analysis, it neglects several important components of shoulder kinematics that affect motion validity and anatomical realism.

First, scapular motion is not modeled, which omits the scapulothoracic contribution to shoulder mobility and the well-established scapulohumeral rhythm. As a result, some poses may be falsely classified as invalid due to apparent bony conflict that would otherwise be resolved by scapular rotation. Accounting for scapular motion would improve anatomical fidelity but would also require assumptions regarding thoracic posture, scapular resting position, and coordinated muscle activation, factors that are difficult to derive from CT alone.

Second, the model does not incorporate translational degrees of freedom at the GH joint. Although the assumption of a fixed rotational center is a valid first-order approximation, it excludes physiologically relevant translations and GH centering behaviors. These micro-translations can influence joint congruency and alter constraint proximity (especially near the boundaries of the solution space) potentially leading to either overly conservative or permissive ROM estimates.

Together, these simplifications limit the capacity of the framework to fully replicate the complex and dynamic interplay of the shoulder's kinematic chain. Future versions of the model could integrate these additional degrees of freedom to enhance the physiological accuracy of ROM predictions.

Chapter 6

Application : Post-Processing Hill-Sachs Engagement Using the Computed ROM

This chapter presents an example of clinical application using the previously computed ROM space. It explores how the ROM simulation framework developed in this thesis can be used to assess the potential impact of HSDs on shoulder stability. The goal is to move beyond static classification models and evaluate lesion engagement dynamically, using a post-processing strategy built on the validated solution space.

The presence and orientation of an HSD can significantly affect shoulder stability. Traditionally, engagement has been assessed using static models such as the "on-track/off-track" concept (or GTC), which compares the medial extent of the HSD to the glenoid track, the area of contact between the glenoid and humeral head during motion [16]. A lesion extending beyond this track is considered "off-track," increasing the risk of engagement and recurrent instability.

However, recent studies have questioned the predictive power of this model. Stefaniak et al. reported that 15% of shoulders classified as "on-track" still experienced instability after Bankart repair [19]. These findings underscore the limitations of static assessments and motivate a more dynamic, movement-based evaluation of HSD engagement.

6.1 Post-Processing Method

No constraint related to the HSD is applied during the ROM search itself. This choice preserves the full space of feasible motions and delegates the interpretation of engagement risk to the clinician. Rather than enforcing a fixed threshold, the following tool provides a post-processing analysis that quantifies the potential influence of the HSD on the ROM, enabling a more personalized and clinically flexible decision-making process.

The glenoid projection onto the humeral head is extracted in the same manner as during ROM computation and serves as the basis for coverage analysis. The HSD is manually segmented based on its visual appearance on the humeral head surface. This segmentation is performed independently of the articular surface definition used for COV computation, ensuring that the ROM evaluation remains unbiased by the presence of the lesion. The HSD is introduced only during post-processing. Some overlap between the defect and the articular surface is expected and necessary to assess its potential impact on joint stability. The dimensions and localization of each lesion are computed using `Replasia ShoulderStudio` to enable complete characterization.

6.2 Representation

To facilitate interpretation, a discrete color mapping of engagement is applied across the ROM space:

- **Green:** Engagement $< 1\%$ — minimal or no interaction (accounting for mesh resolution).
- **Yellow:** Engagement between 1% and 15% — moderate overlap, requiring clinical interpretation.
- **Red:** Engagement $\geq 15\%$ — substantial overlap, likely to affect joint stability.

These thresholds are proposed for visualization purposes and can be adjusted by users according to their clinical judgment. This allows the tool to be adapted to different surgical philosophies or patient-specific contexts.

This color-based representation allows clinicians to rapidly identify whether the HSD influences daily functional movements or is only engaged in extreme positions unlikely to be clinically significant.

In addition to this color mapping of the solution space, two visuals are provided to synthesize and interpret lesion impact:

- A **pie chart** displays the overall distribution of ROM configurations across the three engagement categories (green, yellow, red). This provides an immediate, intuitive view of how much of the motion space is at risk.
- **Histograms per color category** show the internal distribution of engagement percentages within each group. These histograms allow the user to evaluate whether points are clustered near lower thresholds (e.g., minimal engagement) or closer to upper thresholds (e.g., high risk of instability). For example, a yellow category concentrated near the red limit would be more concerning than one distributed near green.

Together, these graphs allow for both a qualitative (visual) and a semi-quantitative (distributional) interpretation of HSD risk across the ROM.

6.3 Results

Patient 1 and Patient 4 do not exhibit an HSD and are therefore excluded from this section. Due to the considerable inter-patient variability observed in Patient 2, Patient 3, and Patient 5, all three are discussed in the main text.

To enhance clarity, the detailed engagement maps, pie charts, and histograms have been relocated to the appendix. Instead, Table 6.1 summarizes the key findings, including defect positioning, geometric dimensions, and engagement statistics across the ROM. The full visualization and classification maps for each patient are provided in Appendix C.

Patient 3 presents the deepest and widest defect, while Patient 5 shows the tallest one. Notably, the lesion in Patient 5 is also the most laterally located, whereas those of Patient 2 and 3 are situated more medially.

Patient 5 displays no engagement throughout the motion space, with 100% of configurations falling in the green (non-engaged) category. Patient 2 exhibits moderate engagement in select regions, with 7.6% of poses reaching the yellow threshold but none entering the red zone. Patient 3 demonstrates both medium and high-risk engagement patterns, with 10.4% of positions in the yellow category and 4.7% in the red.

In both Patient 2 and Patient 3, these engagements tend to cluster near the initial reference pose, rather than at the extremes of the ROM envelope. No consistent anatomical or directional pattern emerged beyond this initial positioning trend.

Table 6.1: Quantitative summary of Hill-Sachs defect characteristics and engagement risk across the three affected patients. "Rel. Pos." refers to the relative mediolateral location of the defect. D, H, and W indicate defect depth, height, and width, respectively, measured on the 3D surface. The final three columns report the proportion of joint configurations falling into each engagement risk category (Green: $<1\%$, Yellow: 1–15%, Red: $\geq 15\%$).

Patient	**Rel. Pos.**	**D (mm)**	**H (mm)**	**W (mm)**	**Gre. (%)**	**Yel. (%)**	**Red (%)**
P2	Medial	4.1	12.7	3.5	92.4	7.6	0.0
P3	Medial	5.9	15.3	7.4	84.9	10.4	4.7
P5	Lateral	3.6	19.6	5.5	100.0	0.0	0.0

The histogram plots (Figure 6.1) offer a more detailed look at engagement distribution. For Patient 5, the green distribution includes only a single point slightly above 0% (engagement of 0.09%), and the yellow and red distributions are empty. This confirms that the selected thresholds are appropriate and need not be redefined.

For Patient 2, a few sub-1% engagements are present, but the yellow category remains concentrated in the lower range (1–4%).

In Patient 3, minimal sub-threshold engagements are again observed, but the yellow category displays a broader distribution than in Patient 2, extending further toward the upper limit. The red category does not show a clear bias toward high or low values.

In summary, this analysis reveals substantial inter-patient variability in HSD engagement, both in terms of extent and spatial distribution. While Patient 5 demonstrates no engagement risk despite a visible lesion, Patients 2 and 3 show varying degrees of involvement, with Patient 3 exhibiting the most concerning profile. These findings reinforce the value of a dynamic, patient-specific assessment of HSD, rather than relying solely on static geometric criteria.

6.4 Discussion

The dynamic engagement analysis introduced in this study provides a complementary perspective to traditional static methods such as the “on-track/off-track” model. By quantifying the interaction between the glenoid and HSD across the full ROM space, it offers a more functional and individualized evaluation of engagement risk.

The results clearly demonstrate that engagement risk is not solely dependent on lesion size. For instance, although Patient 5 had the tallest defect, no engagement was observed, likely due to its more lateral positioning. In contrast, Patient 2 exhibited moderate engagement despite having the smallest defect in the cohort. These observations support the idea that lesion location may be more critical than geometric dimensions in determining engagement behavior. This also aligns with the literature, where HSD width (rather than depth or height) is commonly used to define the glenoid track.

Interestingly, engagement was mostly observed near the initial reference pose rather than in extreme positions. This challenges the assumption that risky contact only occurs at large amplitudes and instead suggests that some lesions may pose a threat even during daily, low-amplitude motion. Initially, it was

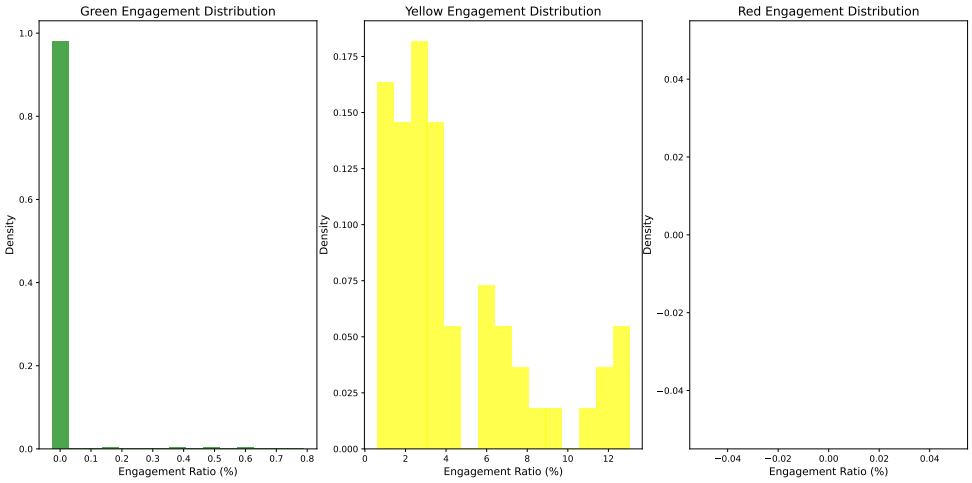

(a) Patient 2

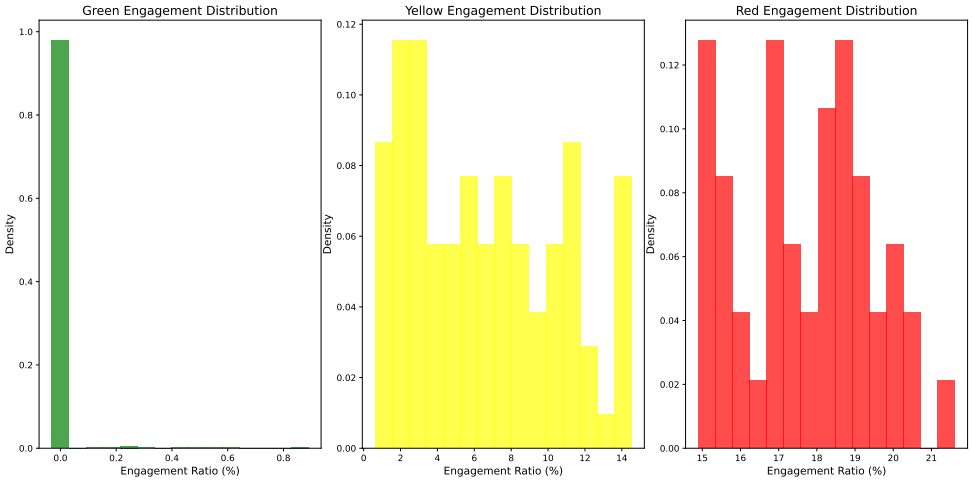

(b) Patient 3

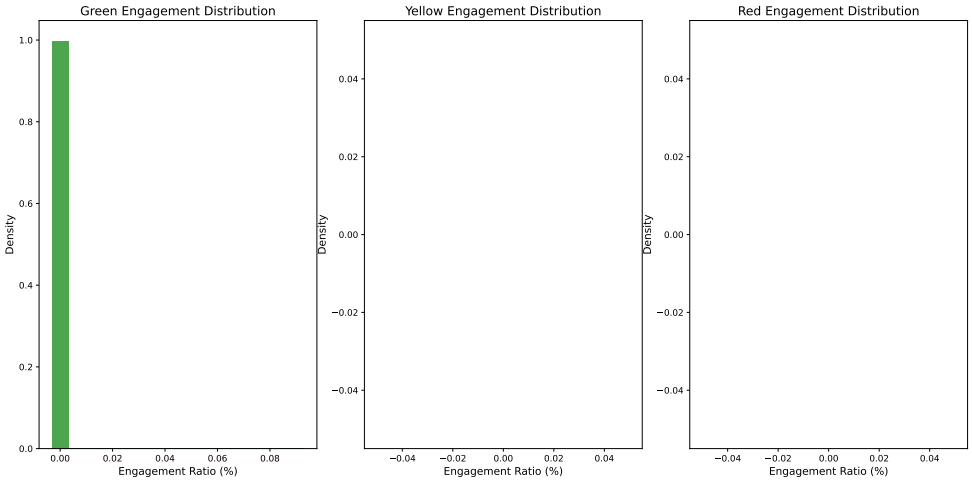

(c) Patient 5

Figure 6.1: Normalized engagement ratio distributions per risk category for each patient. Each curve reflects the proportion of configurations classified into the respective HSD risk zones.

assumed that the reduced ROM of Patient 5 might explain the absence of engagement. However, since engagements in other patients occurred near the starting pose, this does not appear to be the decisive factor.

These findings also highlight a potential limitation of the GTC: because it relies primarily on lesion width and does not account for lesion positioning, it may fail to predict engagement accurately in certain scenarios. The case of Patient 2 reinforces this idea: despite a narrow lesion, it still presented measurable engagement risk, likely due to medial positioning.

Inheritance and Functional Implications

Given the clustering of engagement near the neutral pose, it could be clinically relevant to explore "inheritance" of engagement, where a risk observed in one configuration might extend to nearby motions, thereby limiting entire movement paths rather than isolated points. However, the current ROM simulation relies on a simplified decomposition that does not follow natural motion trajectories. As a result, introducing inheritance could lead to misleading conclusions and artificially expand the yellow or red zones. Future work could consider this idea but would require more physiologically accurate motion modeling.

Underestimation of Engagement Due to Translation-Free Modeling

A major limitation of the current tool is the absence of translational motion in the humeral head. Engagement is estimated purely through projection, without accounting for anterior-posterior shifts that occur during physiological movements. This simplification likely explains some unexpected findings, such as the lack of observed contact between the HSD and the Bankart lesion, despite their well-documented clinical association. The model's assumption of a ball-and-socket joint without translation restricts the humeral head to remain centered, which prevents it from reaching positions where the posterior HSD might contact the anterior glenoid (where Bankart lesions typically occur).

Moreover, the glenoid surface used for ROM determination does not represent the pre-lesion anatomy. Since the Bankart lesion reduces anterior surface area, the actual envelope of feasible positions might already be limited in that region, preventing engagement events from being observed, even when clinically expected. Nonetheless, the complete absence of posterior-to-anterior contact (between HSD and Bankart zones) suggests that incorporating translational kinematics is essential for capturing this interaction and improving the realism of the engagement model.

Altogether, the projection-only estimation may underestimate or overestimate functional engagement in specific configurations. Incorporating coupled rotational-translational kinematics in future work would improve physiological accuracy and allow better prediction of clinically relevant lesion interactions.

Segmentation and Sample Size

The manual segmentation of the HSD introduces potential variability, despite using a consistent method across patients. Future implementations could benefit from semi-automated surface extraction to reduce subjectivity. Additionally, while the observations made here are informative, they are based on only three patients with different profiles. It is therefore important to avoid generalizing these findings too quickly. A larger dataset, including a wider range of lesion types and patient anatomies, would be necessary to validate the method's clinical utility.

6.5 Conclusion

This chapter has illustrated how the simulated ROM envelope can serve as a foundation for evaluating the clinical relevance of bone lesions through targeted post-processing.

This post-processing framework introduces a dynamic and patient-specific method for evaluating the influence of HSDs on shoulder motion. By deferring engagement analysis to a separate step after ROM exploration, the tool preserves the full movement envelope while enabling a flexible interpretation of clinical risk. The use of color mapping and visual summaries (pie charts, histograms) supports both intuitive and semi-quantitative insights, bridging biomechanical simulation with surgical decision-making.

The results demonstrate that engagement is not solely driven by lesion size, but also by lesion positioning. Patients with small but medially located defects showed measurable engagement, whereas more lateral lesions, even when tall, did not. This observation supports critiques of the "on-track/off-track" model, which emphasizes lesion width but neglects spatial positioning. In this context, dynamic evaluation provides a richer understanding of instability risk.

While developed as a proof of concept for HSDs, the methodology is general and could be extended to other pathologies of the humeral head, such as reverse HSD, osteochondral defects, or post-surgical voids. Future improvements should focus on integrating translational joint behavior, soft tissue effects, and automated segmentation to further enhance realism and clinical applicability.

In summary, this tool represents a first step toward more dynamic, personalized assessment of GH engagement. It complements existing static criteria and opens the door for more nuanced surgical planning tailored to each patient's anatomical and functional profile.

Chapter 7

General Conclusions and Perspectives

7.1 General Conclusions

This thesis presented the development and application of a patient-specific simulation framework designed to estimate the GH ROM using clinical CT scans. The core objective was to build a framework capable of determining shoulder joint mobility by accounting for individual anatomical features and pathological conditions, with particular emphasis on how bony defects, such as HSD and BBL, affect the feasibility of joint configurations.

The proposed framework relies on three key components. First, the GH joint is modeled as a ball-and-socket articulation, and the solution space is explored through a combination of coarse sampling and binary search refinement near motion boundaries. This hybrid strategy was designed to efficiently identify valid configurations while reducing redundant evaluations and controlling computational cost. Second, a multi-criteria constraint evaluation system was implemented, incorporating collision detection, COV assessment, critical distance thresholds (CHD and AHD), and anatomical orientation checks. These constraints were selected to ensure clinical relevance while preserving generalizability across patients. Third, comprehensive visualization and categorization tools were developed to interpret, quantify, and compare ROM across subjects and motion planes.

The analysis conducted across five patients revealed consistent trends and clinically meaningful findings. For instance, the solution space of feasible joint positions consistently approximated a truncated sphere, an expected outcome given the ball-and-socket assumption, with specific patterns observed across all patients. The introduction of anatomical constraints shaped this envelope, reducing feasible amplitudes in spatial zones corresponding to known impingement or instability risks. Pathology-induced alterations were also captured, with BBL reducing glenoid support and thereby affecting joint stability. In contrast, the influence of HSD was analyzed during postprocessing, revealing that their engagement with the glenoid depends strongly on their size and orientation.

In addition to characterizing the global ROM envelope, the framework enabled a deeper analysis of how constraint thresholds and anatomical conditions shape specific motion patterns. Constraint sensitivity mapping illustrated how threshold changes can drastically reshape the ROM envelope, offering valuable insight into potential compensatory mechanisms or surgical planning strategies. Furthermore, the engagement analysis with HSD showed that critical interactions often occurred near the neutral pose, rather than at the extremes of motion, suggesting that conventional assessments may underestimate mid-range instabilities.

Nevertheless, several simplifying assumptions were necessary for feasibility. The scapula was treated as a static structure, omitting scapulothoracic motion and its coupling with humeral kinematics. The humeral head was assumed to rotate about a fixed center, excluding physiologically relevant translations.

Soft tissues, though essential to joint function, were not represented, limiting the model to a geometric feasibility analysis. Moreover, landmarking was performed manually, introducing potential variability, and the dataset remained relatively small, restricting broader generalization.

Despite these limitations, the proposed framework provides a first foundation for exploring the feasibility of patient-specific ROM analysis. It demonstrates that combining anatomical modeling, constraint-based simulation, and motion decomposition is technically achievable and can yield clinically interpretable outputs under controlled assumptions. However, the tool remains at an early stage of development, and its applicability to clinical decision-making is far from guaranteed.

Significant challenges must be addressed before this approach can be considered robust or generalizable. These include the integration of soft tissue behavior, improved modeling of joint mechanics, expanded and validated datasets, and a better understanding of how to interpret constraint interactions in real clinical scenarios. Whether this line of research can ultimately support surgical planning or diagnostic protocols remains an open question requiring further investigation.

Nonetheless, this thesis provides a starting point for future work. It shows that modeling shoulder motion in a patient-specific and anatomically realistic way is possible, but also complex. The results help define the challenges ahead and open the door to further studies aimed at improving and expanding the method.

7.2 Perspectives

While the current framework offers a base for joint motion simulation, several improvements are necessary to enhance clinical realism, interpretability, and applicability. This section outlines key directions for future development based on the limitations identified throughout the study.

7.2.1 Expanding and Validating the Dataset

The most immediate limitation of the present work is the small dataset size, which restricts statistical power and limits the ability to generalize the results. Future studies should aim to incorporate a broader and more diverse patient population, including variations in age, sex, and pathological conditions. When possible, bilateral imaging could offer valuable internal comparisons between the pathological and contralateral shoulder, helping to define personalized baselines for constraint interpretation.

As the dataset grows, ensuring the reliability and clinical relevance of the simulated results becomes increasingly important. This will require a validation strategy, beginning with comparisons to clinical assessments such as goniometric measurements or intraoperative observations, which can serve as external references for joint mobility and constraint behavior. Evaluating the intra- and inter- reproducibility of the framework through repeatability studies will also be essential

In parallel, the development of standardized quantitative metrics (such as envelope volume, angular excursion, or constraint sensitivity indices) would facilitate objective comparisons across patients, conditions, and modeling parameters. Establishing formal validation protocols, along with defined performance benchmarks, will be crucial to assess simulation accuracy and to guide further methodological refinement.

Beyond clinical comparison, experimental studies on cadaveric specimens could play a key role in verifying specific aspects of the model. Such studies would allow for the assessment of constraint threshold definitions and joint engagement patterns under controlled conditions. By providing a physical ground truth, cadaveric experiments would support the calibration of simulation parameters and help bridge the gap between computational predictions and physiological behavior.

7.2.2 Image Modality Upgrade: Incorporating MRI

CT imaging provides detailed information about bone morphology, but it does not capture soft tissue structures, which play a crucial role in joint stability and motion limits. MRI, especially when performed on high-field scanners, has emerged as a potential alternative that can capture both soft tissues and osseous structures in a single scan [42].

Recent studies have demonstrated the feasibility of segmenting bone structures from MRI, while also providing access to soft tissues such as the capsule, labrum, and rotator cuff. Incorporating these structures into the simulation would allow for more realistic modeling of passive constraints such as capsular tension, labral engagement, and muscular pull [42].

However, the use of MRI is not without limitations. Image quality can vary significantly depending on the scanner hardware and imaging protocols used. In particular, the resolution of soft tissues must be sufficiently high to support reliable segmentation and biomechanical modeling. If key structures such as the capsule, labrum, or rotator cuff are poorly defined or blurred, they may introduce uncertainty or noise into the simulation rather than improving its realism. Moreover, while high-resolution MRI scanners have shown promise for simultaneous bone and soft tissue visualization, such equipment is not universally available, and most clinical settings still rely on lower-field or non-optimized systems [42].

Another important consideration is cost and practicality. Acquiring both CT and MRI scans for each patient would significantly increase imaging time, clinical workload, and overall resource consumption. This reduces the likelihood of such a dual-modality approach being adopted in routine practice. Therefore, a preliminary feasibility study comparing CT- and MRI-based models on the same patients is recommended to assess whether MRI alone can deliver sufficient anatomical fidelity. If MRI proves inadequate for bone structure definition, hybrid approaches may offer a compromise, combining CT for accurate osseous geometry and MRI for soft-tissue data, but such solutions must be carefully weighed against their clinical and logistical constraints.

7.2.3 Automated Landmarking and Reconstruction Methods

A key limitation of the current framework lies in the use of manual landmarking, which is time-consuming and prone to inter- and intra- variability. This not only affects reproducibility but also limits the scalability of the method when applied to larger datasets.

To overcome these issues, future work could explore automated landmarking approaches. By reducing user intervention, automation would improve consistency across patients and significantly speed up the modeling pipeline. While the implementation of such methods would require additional development and validation, their integration could make the framework more robust and clinically viable.

In addition, surface reconstruction methods could help address cases where anatomical regions are incomplete due to imaging artifacts, missing segments, or the presence of lesions. One promising approach in this context is statistical shape modeling, which uses a population-based model to estimate the most likely shape of missing or altered anatomical structures. By approximating the original bone geometry or simulating a healthy counterpart, such techniques could support more accurate comparisons and improve the interpretation of how specific defects affect joint mobility.

Finally, incorporating contralateral shoulder data, when available, would allow for personalized baseline definitions and help analyze potential compensatory mechanisms or side dominance effects. Although bilateral imaging is not routinely performed in clinical practice, mirrored anatomy or population-based anatomical models could serve as useful alternatives in this context. However, it is important to note that such symmetry assumptions are more reliable for bony structures than for soft tissues, which are often asymmetric due to muscle dominance, usage patterns, or previous injuries. This distinction should

be considered when interpreting contralateral comparisons, especially in simulations involving soft-tissue constraints.

7.2.4 Parallelization and Computational Scalability

Although several structural and algorithmic optimizations have been implemented in the current framework, further improvements in computational efficiency remain possible. One particularly promising direction is the use of parallel processing. The evaluation of candidate poses during ROM analysis is inherently independent, making the task well-suited for parallel execution.

Introducing multithreading or multiprocessing techniques could enable simultaneous evaluation of multiple joint configurations. This would be especially beneficial when exploring large angular spaces or processing multiple patient datasets, as it would significantly reduce total computation time without altering the logic of constraint verification.

Such an improvement would not only enhance the responsiveness of the simulation pipeline but also make the framework more scalable for future clinical or research use.

7.2.5 Modeling Improvements: Toward Physiological Fidelity

The current model is intentionally simplified to focus on feasibility, but future versions should move toward a more physiologically realistic representation of the shoulder joint.

Alternative Rotation Decompositions

This thesis employed a fixed rotation sequence (Yh–Xh–Zh) to describe GH motion, primarily for its simplicity and clinical interpretability. While this decomposition produced consistent results, it may not be optimal for all components of the framework, particularly the inheritance mechanism used during post-processing.

Alternative decompositions, such as Yh–Xh–Yh, could offer better alignment with perceived motion patterns and improve the continuity of inherited configurations across motion paths. Due to time constraints, only a limited comparison of rotation schemes was performed, and a more systematic analysis is still needed. Although we believe that starting with Yh (axial rotation) remains a sound choice, the second and third rotation axes may require revision to better support motion classification and interpretability.

Introducing Translational Degrees of Freedom

In the current framework, the GH joint is modeled as a purely rotational ball-and-socket joint with a fixed CoR. While this assumption simplifies the simulation and reflects the dominant behavior of the joint, it does not fully capture its physiological behavior. In reality, the humeral head can translate slightly relative to the glenoid, especially in cases of instability or during dynamic movements.

Allowing small translations would improve the biomechanical realism of the model but would also challenge the ball-and-socket assumption, since the CoR would no longer be fixed. Future developments could begin by enabling controlled anterior-posterior translations and testing whether the current constraints are sufficient to maintain a stable and realistic joint configuration.

If necessary, additional mechanisms such as soft-tissue-inspired stabilizing forces or translation thresholds could be introduced to prevent non-physiological displacements. These adaptations would require redefining how constraints are evaluated, particularly those involving COV or proximity. Although such

changes would increase the model's complexity, they would also allow for a more accurate simulation of shoulder motion in pathological or borderline-stable conditions.

Adding Scapular Motion

In the current implementation, the scapula is modeled as a static structure, and all humeral motion is due to the GH joint. While this assumption simplifies the kinematic chain and isolates GH behavior, it ignores the physiological contribution of scapular motion to shoulder elevation.

To approximate the scapulohumeral rhythm without significantly increasing model complexity, a first step could be to introduce a simplified kinematic rule that updates the scapular orientation based on global arm elevation. For example, upward rotation of the scapula could be applied proportionally to the elevation angle, shifting the glenoid frame accordingly before computing humeral motion. This would require adapting the transformation chain used during ROM sampling so that the glenoid orientation becomes a function of the current pose, rather than remaining fixed throughout the simulation.

A more advanced solution would involve modeling the entire shoulder girdle, including the clavicle, sternoclavicular, and acromioclavicular joints. In this scenario, scapular positioning would be derived from a chain of joint rotations, and the orientation of the glenoid would be updated dynamically through successive transformations from the thorax. While such an approach would significantly enhance anatomical realism, it also introduces considerable complexity in terms of joint representation, motion coordination, and parameter tuning.

Moreover, implementing such a model is constrained by practical limitations in image acquisition. In most clinical CT protocols focused on the shoulder, the clavicle (particularly the sternoclavicular joint) is only partially visible or entirely outside the field of view. This restricts the possibility of extracting patient-specific geometry or kinematics for these structures. As a result, full girdle modeling would require either generic anatomical assumptions or statistical estimation. Given these constraints, this level of modeling is more suitable for long-term research or specialized applications in musculoskeletal simulation rather than immediate integration into the current framework.

Incorporating scapular motion, even in a simplified form, would reduce the risk of falsely classifying feasible postures as invalid and bring the model closer to physiological reality.

Incorporating Soft Tissue Models

A major limitation of the current framework is the absence of soft tissue modeling. At present, joint feasibility is assessed purely through geometric criteria applied to the bony structures. While this approach simplifies the problem and provides useful insights, it does not account for key stabilizing elements such as the capsule, ligaments, or muscle forces. Transitioning toward a functional musculoskeletal model would allow simulation of passive and active joint mechanics, enabling a deeper assessment of motion feasibility. Platforms such as OpenSim offer the ability to simulate muscle-tendon dynamics and joint reaction forces, which could help identify configurations that are not just collision-free but also biomechanically stable.

However, this extension represents a long-term objective rather than an immediate improvement. Accurate soft tissue modeling requires either detailed imaging (e.g., high-resolution MRI) or the use of population-based parametric models, both of which introduce challenges in terms of data acquisition, model complexity, and validation. Moreover, simulating active control strategies would require assumptions about muscle recruitment and external loads that go beyond the current scope. Although this direction holds strong potential, it would involve a significant methodological shift and is unlikely to be feasible without a dedicated imaging and modeling pipeline.

Summary

The framework developed in this thesis represents a first step toward patient-specific, constraint-aware modeling of shoulder motion. Although not yet suitable for clinical use, it demonstrates the feasibility of combining anatomical modeling, constraint evaluation, and motion decomposition in a structured and interpretable simulation pipeline. The results highlight key areas for future development, including dataset expansion, integration of scapular and translational kinematics, automated landmarking, incorporation of soft tissue effects, and improvements in computational scalability through parallel processing. While some of these extensions are technically accessible in the short term, others (such as full musculoskeletal modeling) remain long-term objectives. Continued progress in these directions will be essential to determine whether this type of simulation can ultimately support clinical decision-making in diagnosis, rehabilitation, or surgical planning.

Bibliography

[1] C. Charbonnier, S. Chagué, F. C. Kolo, J. C. K. Chow, and A. Lädermann, "A patient-specific measurement technique to model shoulder joint kinematics," *Orthopaedics & Traumatology: Surgery & Research*, vol. 100, no. 7, pp. 715–719, 2014. doi: 10.1016/j.otsr.2014.06.015.

[2] P. Lukasiewicz, E. McFarland, J. D. Hassebrock, *et al.*, "Anatomic glenohumeral arthroplasty: State of the art," *Journal of ISAKOS*, vol. 8, no. 5, pp. 296–305, 2023. doi: 10.1016/j.jisako.2023.05.001.

[3] R. Abrams and H. Akbarnia. "*Shoulder Dislocations Overview*." Available: https://www.ncbi.nlm.nih.gov/books/NBK459125/, StatPearls Publishing. (Aug. 8, 2023).

[4] L. R. Chang, P. Anand, and M. A. Varacallo. "Anatomy, shoulder and upper limb, glenohumeral joint," StatPearls Publishing. (Aug. 8, 2023), [Online]. Available: https://www.ncbi.nlm.nih.gov/books/NBK537018/.

[5] G. Gasbarro, B. Bondow, and R. Debski, "Clinical anatomy and stabilizers of the glenohumeral joint," *Annals of Joint*, vol. 2, no. 10, 2017. doi: 10.21037/aoj.2017.10.03.

[6] G. Wu, F. C. van der Helm, H. (DirkJan) Veeger, *et al.*, "Isb recommendation on definitions of joint coordinate systems of various joints for the reporting of human joint motion—part ii: Shoulder, elbow, wrist and hand," *Journal of Biomechanics*, vol. 38, no. 5, pp. 981–992, 2005. doi: 10.1016/j.jbiomech.2004.05.042.

[7] G. C. Terry and T. M. Chopp, "Functional anatomy of the shoulder," *Journal of Athletic Training*, vol. 35, no. 3, pp. 248–255, 2000. [Online]. Available: https://pmc.ncbi.nlm.nih.gov/articles/PMC1323385/.

[8] Y. A. Almajed, A. C. Hall, T. H. Gillingwater, and A. Alashkham, "Anatomical, functional and biomechanical review of the glenoid labrum," *Journal of Anatomy*, vol. 240, pp. 761–771, 2021. doi: 10.1111/joa.13582.

[9] J. P. Braman, S. C. Engel, R. F. LaPrade, and P. M. Ludewig, "In vivo assessment of scapulohumeral rhythm during unconstrained overhead reaching in asymptomatic subjects," *Journal of Shoulder and Elbow Surgery*, vol. 18(6), pp. 960–967, 2009. doi: 10.1016/j.jse.2009.02.001.

[10] S. E. Sheehan, G. Gaviola, R. Gordon, A. Sacks, L. L. Shi, and S. E. Smith, "Traumatic shoulder injuries: A force mechanism analysis—glenohumeral dislocation and instability," *American Journal of Roentgenology*, vol. 201, no. 2, pp. 378–393, 2013. doi: 10.2214/AJR.12.9986.

[11] S. Cutts, M. Prempeh, and S. Drew, "Anterior shoulder dislocation," *Annals of The Royal College of Surgeons of England*, vol. 91, no. 1, pp. 2–7, 2009. doi: 10.1308/003588409X359123.

[12] R. M. Greiwe and W. N. Levine, "Chapter 6 - findings and pathology associated with anterior shoulder instability," in *Shoulder Instability: A Comprehensive Approach*, M. T. Provencher and A. A. Romeo, Eds., Philadelphia: W.B. Saunders, 2012, pp. 65–78. doi: 10.1016/B978-1-4377-0922-3.00015-0.

[13] A. W. Hasebroock, J. Brinkman, L. Foster, and J. P. Bowens, "Management of primary anterior shoulder dislocations: A narrative review," *Sports Medicine - Open*, vol. 5, no. 31, pp. 1–8, 2019. doi: 10.1186/s40798-019-0203-2.

[14] E. Ramhamadany and C. S. Modi, "Current concepts in the management of recurrent anterior glenohumeral joint instability with bone loss," *World Journal of Orthopedics*, vol. 7, no. 6, pp. 343–354, Jun. 2016. doi: 10.5312/wjo.v7.i6.343.

[15] J. F. Griffith, G. E. Antonio, P. S. H. Yung, *et al.*, "Prevalence, pattern, and spectrum of glenoid bone loss in anterior shoulder dislocation: Ct analysis of 218 patients," *American Journal of Roentgenology*, vol. 190, no. 5, pp. 1247–1254, 2008. doi: 10.2214/AJR.07.3009.

[16] Z. J. Herman, E. M. Nazzal, L. Keeling, *et al.*, "Bipolar bone loss and distance to dislocation," *Annals of Joint*, vol. 9, p. 7, 2024. doi: 10.21037/aoj-23-17.

[17] R. R. Thacher, J. S. Retzky, M. S. Dekhne, Y. A. Oquendo, and H. G. G. IV, "Current concepts in the measurement of glenohumeral bone loss," *Current Reviews in Musculoskeletal Medicine*, vol. 16, pp. 419–431, 2023. doi: 10.1007/s12178-023-09852-0.

[18] M. Maio, M. Sarmento, N. Moura, and A. Cartucho, "How to measure a hill–sachs lesion: A systematic review," *EFORT Open Reviews*, vol. 4, pp. 151–157, 2019. doi: 10.1302/2058-5241.4.180031.

[19] J. Stefaniak, M. Olmos, M. Chelli, T. Johnston, G. Cárdenas, and P. Boileau, "The glenoid track concept is insufficient to predict bankart failures: A computed tomography scan study," *JSES International*, vol. 8, pp. 434–439, 2024. doi: 10.1016/j.jseint.2024.02.001.

[20] M. Buda, R. D'Ambrosi, E. Bellato, *et al.*, "Failed latarjet procedure: A systematic review of surgery revision options," *Journal of Orthopaedics and Traumatology*, vol. 22, p. 24, 2021. doi: 10.1186/s10195-021-00587-7.

[21] P. Domos, E. Lunini, and G. Walch, "Contraindications and complications of the latarjet procedure," *Shoulder & Elbow*, vol. 10, no. 1, pp. 15–24, 2018. doi: 10.1177/1758573217728716.

[22] M. Ghoraishian, J. A. Abboud, A. A. Romeo, G. R. Williams, and S. Namdari, "Augmented glenoid implants in anatomic total shoulder arthroplasty: Review of available implants and current literature," *Journal of Shoulder and Elbow Surgery*, vol. 28, pp. 387–395, 2019. doi: 10.1016/j.jse.2018.08.017.

[23] D.-H. et al., *Trimesh*, https://trimesh.org/, Version 3.2.0, 2019.

[24] P. Jia, C. Sachin, and M. Dinesh, *Fcl: The flexible collision library*, https://github.com/flexible-collision-library/fcl, Version 0.7.0, Sep. 9, 2021.

[25] X. Chen, T. Liang, C. Liu, *et al.*, "Sex differences in shoulder acromiohumeral contact surface arc length on three-dimensional computed tomography imaging," *Scientific Reports*, vol. 14, no. 1, p. 28 813, 2024, issn: 2045-2322. doi: 10.1038/s41598-024-80336-y.

[26] R. Churchill, J. J. Brems, and H. Kotschi, "Glenoid size, inclination, and version: An anatomic study," *Journal of Shoulder and Elbow Surgery*, vol. 10, no. 4, pp. 327–332, 2001, issn: 1058-2746. doi: 10.1067/mse.2001.115269.

[27] Y. Yoshida, N. Matsumura, Y. Yamada, *et al.*, "Evaluation of three-dimensional acromiohumeral distance in the standing position and comparison with its conventional measuring methods," *Journal of Orthopaedic Surgery and Research*, vol. 15:436, 2020. doi: 10.1186/s13018-020-01935-9.

[28] D. Goutallier, P. Le Guilloux, J.-M. Postel, C. Radier, J. Bernageau, and S. Zilber, "Acromio humeral distance less than six millimeter: Its meaning in full-thickness rotator cuff tear," *Orthopaedics & Traumatology: Surgery & Research*, vol. 97, no. 3, pp. 246–251, 2011. doi: 10.1016/j.otsr.2011.01.010.

[29] H. Graichen, H. Bonél, T. Stammberger, K.-H. Englmeier, M. Reiser, and F. Eckstein, "Sex-specific differences of subacromial space width during abduction, with and without muscular activity, and correlation with anthropometric variables," *Journal of Shoulder and Elbow Surgery*, vol. 10, no. 2, pp. 129–135, 2001. doi: 10.1067/mse.2001.112056.

[30] D. P. Richards, S. S. Burkhart, and S. E. Campbell, "Relation between narrowed coracohumeral distance and subscapularis tears," *Arthroscopy*, vol. 21, pp. 1223–1228, 2005. doi: 10.1016/j.arthro.2005.06.015.

[31] S. F. El-Amin, N. Maffulli, M. C. Mai, *et al.*, "Coracoid impingement and morphology is associated with fatty infiltration and rotator cuff tears," *Journal of Clinical Medicine*, vol. 11, no. 9, 2022. doi: 10.3390/jcm11092661.

[32] U. Orthopaedics and S. Medicine. "Humeroscapular positions and motion." Accessed: 2025-04-04. (2013), [Online]. Available: https://orthop.washington.edu/patient-care/articles/shoulder/humeroscapular-positions-and-motion.html.

[33] H. J. Sulkar, J. L. Zitnay, K. Aliaj, and H. B. Henninger, "Proximal humeral coordinate systems can predict humerothoracic and glenohumeral kinematics of a full bone system," *Gait & Posture*, vol. 90, pp. 380–387, 2021. doi: 10.1016/j.gaitpost.2021.09.180.

[34] R. M. Ehrig, W. R. Taylor, G. N. Duda, and M. O. Heller, "A survey of formal methods for determining the centre of rotation of ball joints," *Journal of Biomechanics*, vol. 39, no. 15, pp. 2798–2809, 2006. doi: 10.1016/j.jbiomech.2005.10.002.

[35] R. L. Lawrence, K. Roseni, and M. J. Bey, "Correspondence between scapular anatomical coordinate systems and the 3d axis of motion: A new perspective on an old challenge," *Journal of Biomechanics*, vol. 145, p. 111 385, 2022. doi: 10.1016/j.jbiomech.2022.111385.

[36] M. Calderone, A. Cereatti, M. Conti, and U. Della Croce, "Comparative evaluation of scapular and humeral coordinate systems based on biomedical images of the glenohumeral joint," *Journal of Biomechanics*, vol. 47, no. 3, pp. 736–741, 2014. doi: 10.1016/j.jbiomech.2013.10.045.

[37] C. W. Kolz, H. J. Sulkar, K. Aliaj, *et al.*, "Reliable interpretation of scapular kinematics depends on coordinate system definition," *Gait & Posture*, vol. 81, pp. 183–190, 2020. doi: 10.1016/j.gaitpost.2020.07.020.

[38] Y. Yoshida, N. Matsumura, Y. Yamada, *et al.*, "Three-dimensional alignment of the upper extremity in the standing neutral position in healthy subjects," *Journal of Orthopaedic Surgery and Research*, vol. 17, no. 1, p. 239, 2022. doi: 10.1186/s13018-022-03113-5.

[39] M. Šenk and L. Chèze, "Rotation sequence as an important factor in shoulder kinematics," *Clinical Biomechanics*, vol. 21, S3–S8, 2006, Proceedings of the 5th Meeting of the International Shoulder Group. doi: 10.1016/j.clinbiomech.2005.09.007.

[40] K. Martin, W. Schroeder, and B. Lorensen, *Vtkselectpolydata*, https://vtk.org/doc/nightly/html/classvtkSelectPolyData.html, 2024.

[41] J. P. Brunkhorst, J. E. Giphart, R. F. LaPrade, and P. J. Millett, "Coracohumeral distances and correlation to arm rotation: An in vivo 3-dimensional biplane fluoroscopy study," *Orthopaedic Journal of Sports and Medicine*, vol. 1(2), 2013. doi: 10.1177/2325967113496059.

[42] L. R. Chong, K. Lee, and F. Y. Sim, "3d mri with ct-like bone contrast – an overview of current approaches and practical clinical implementation," *European Journal of Radiology*, vol. 143, p. 109 915, 2021, issn: 0720-048X. doi: 10.1016/j.ejrad.2021.109915.

Appendix A

Supplementary Results

This appendix presents results from Patients 2 to 5. Each section includes 3D visualizations of the range of motion (ROM) envelope, constraint sensitivity mapping, and anatomical motion slices.

A.1 Patient 2 Results

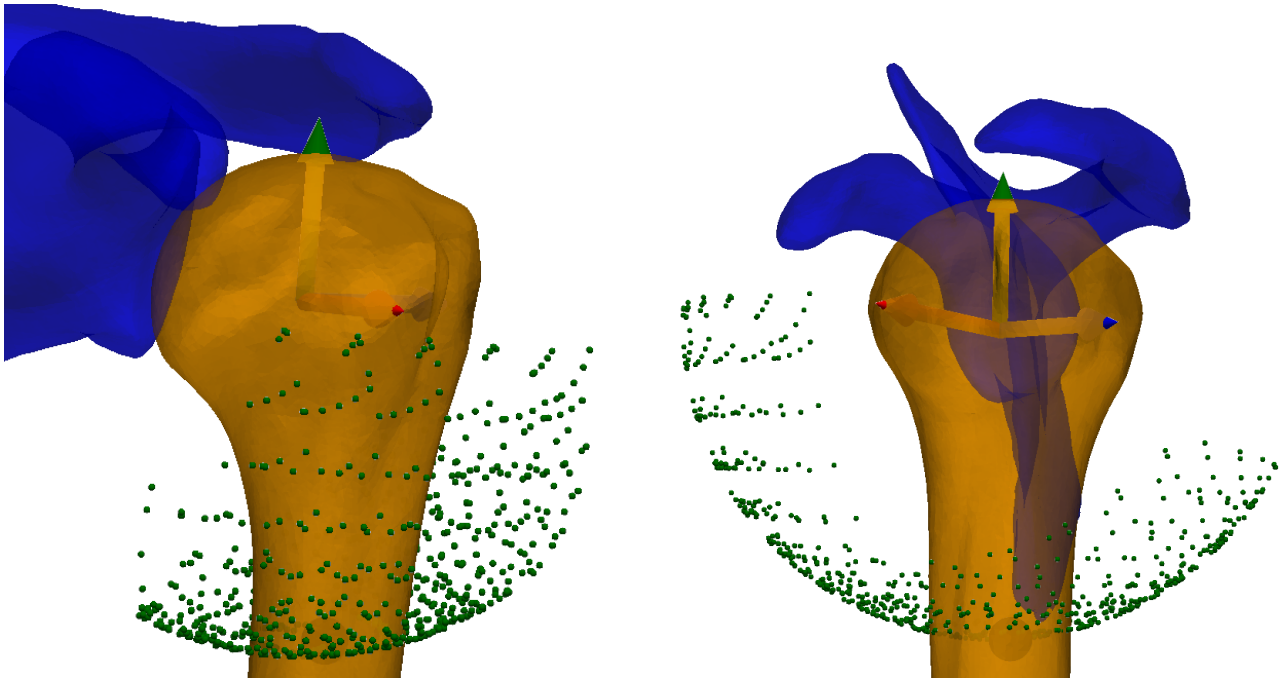

(a) Frontal view (b) Lateral view

Figure A.1: Solution space with two different views. A black line has been added to highlight key geometric features of the solution envelope. (Patient 2)

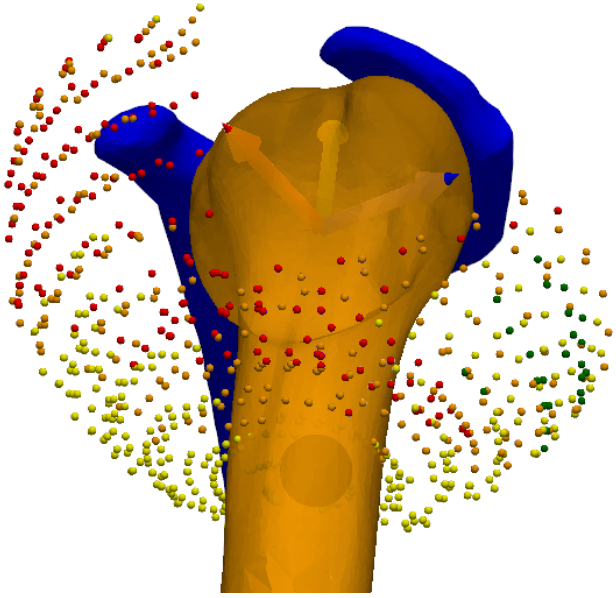

(a) Acromio-humeral distance (AHD) mapping. Red: 4.5–6 mm, orange: 6–7.5 mm, yellow: 7.5–9 mm, green: >9 mm.

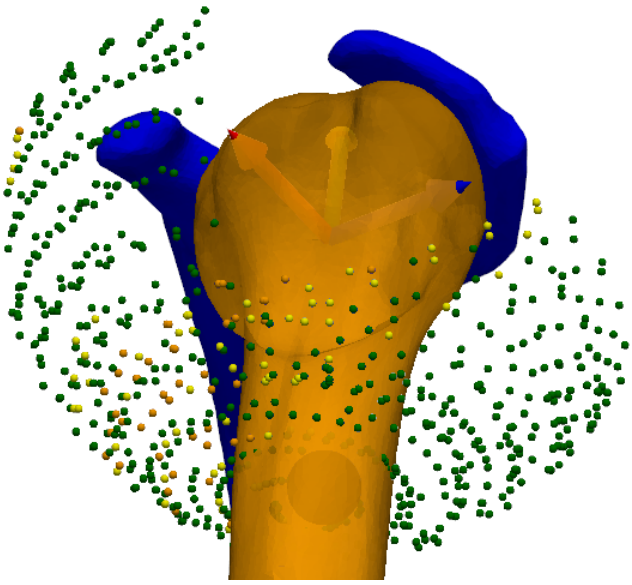

(b) Coraco-humeral distance (CHD) mapping. Red: 8–9.5 mm, orange: 9.5–11 mm, yellow: 11–12.5 mm, green: >12.5 mm.

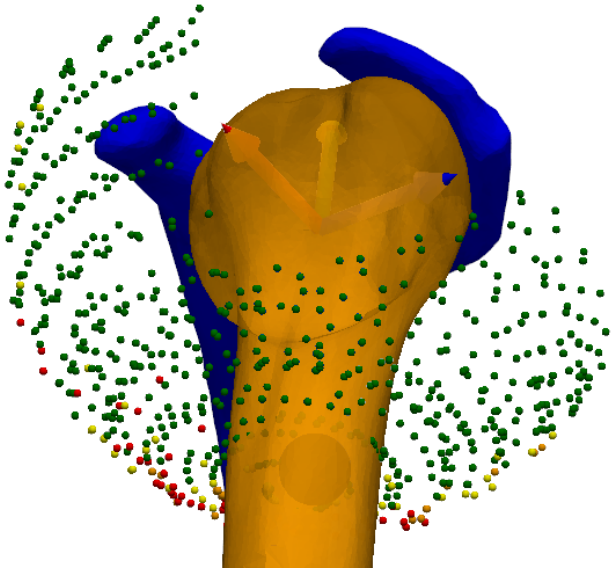

(c) Glenoid coverage mapping. Red: 15–16.5%, orange: 16.5–18%, yellow: 18–19.5%, green: >19.5%.

Figure A.2: Constraint mapping of the solution space for Patient 2. Subfigures show thresholds applied to (a) acromio-humeral distance (AHD), (b) coraco-humeral distance (CHD), and (c) glenoid coverage.

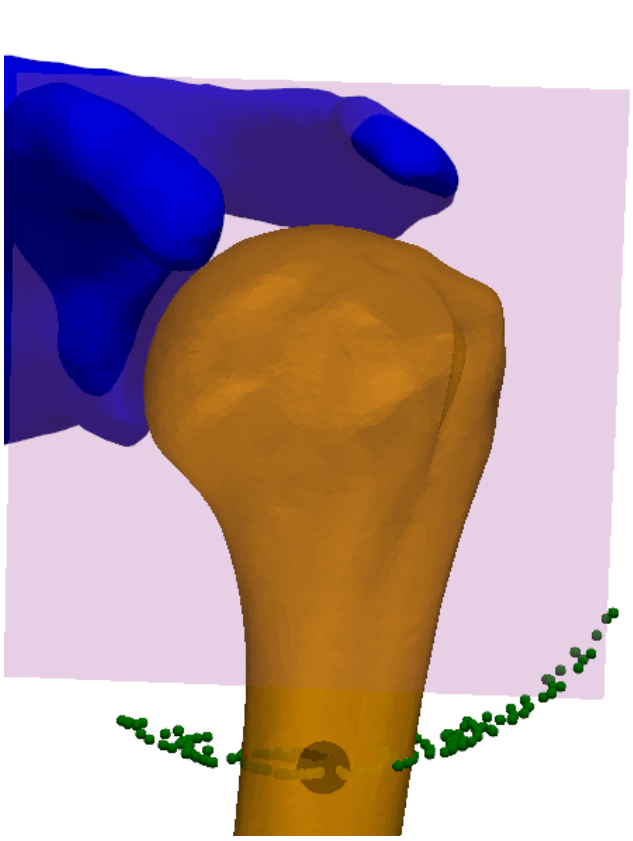

(a) Abduction-adduction solutions

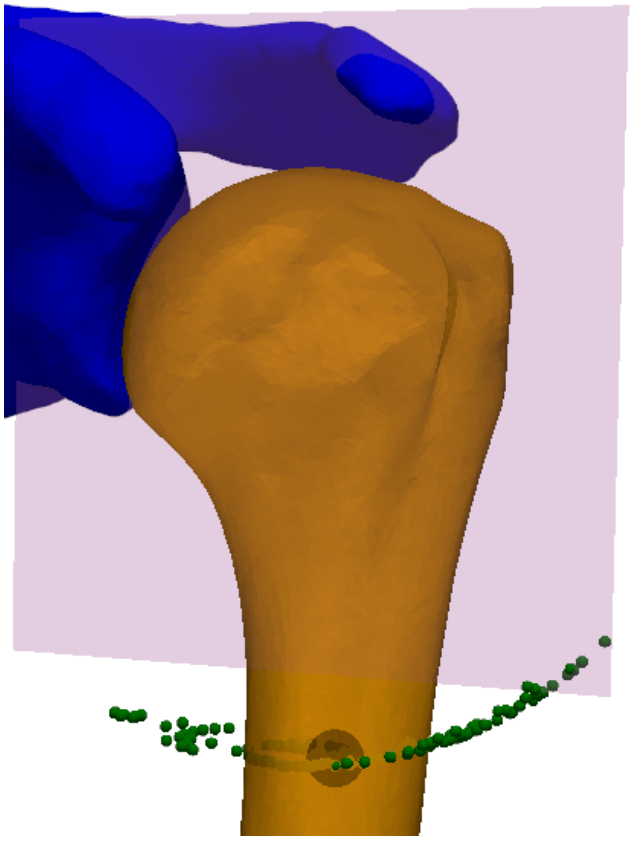

(b) Scapular abduction-adduction solutions

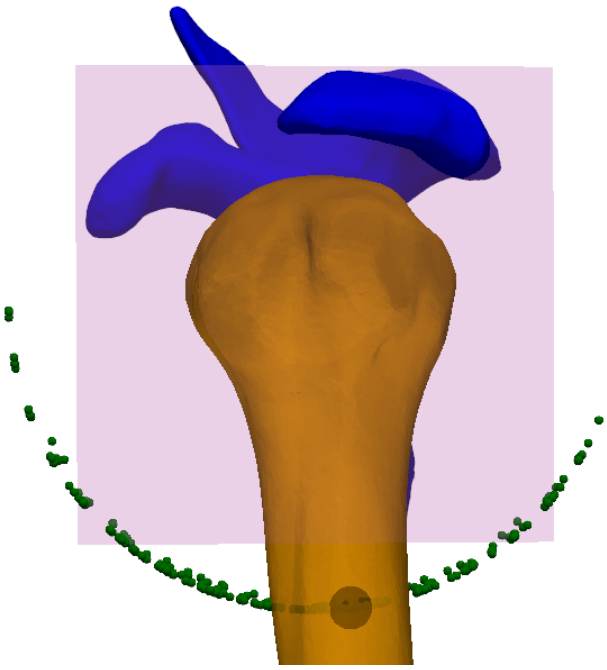

(c) Pure flexion-extension solutions

Figure A.3: Planar motion slices for Patient 2. The purple plane defines the anatomical movement direction. Valid configurations (green) represent achievable positions within the defined slice.

A.2 Patient 3 Results

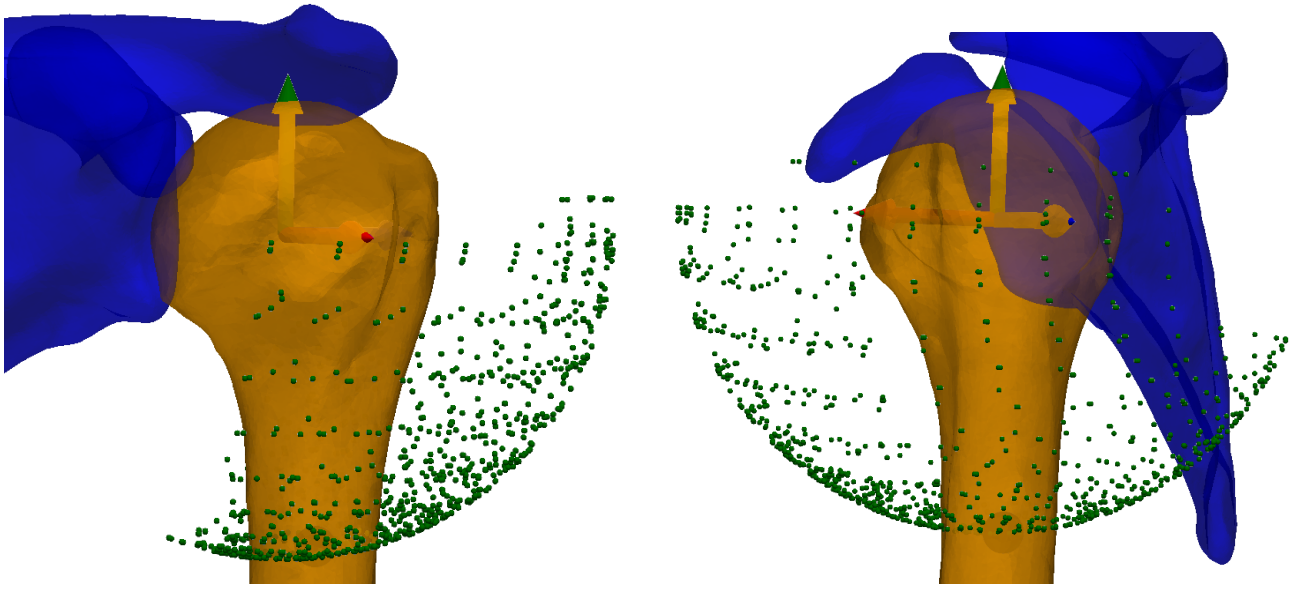

(a) Frontal view (b) Lateral view

Figure A.4: Solution space with two different views. A black line has been added to highlight key geometric features of the solution envelope. (Patient 3)

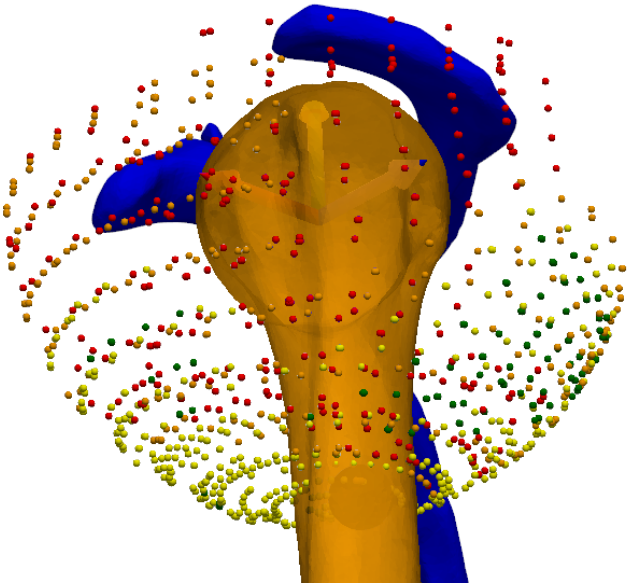

(a) Acromio-humeral distance (AHD) mapping. Red: 4.5–6 mm, orange: 6–7.5 mm, yellow: 7.5–9 mm, green: >9 mm.

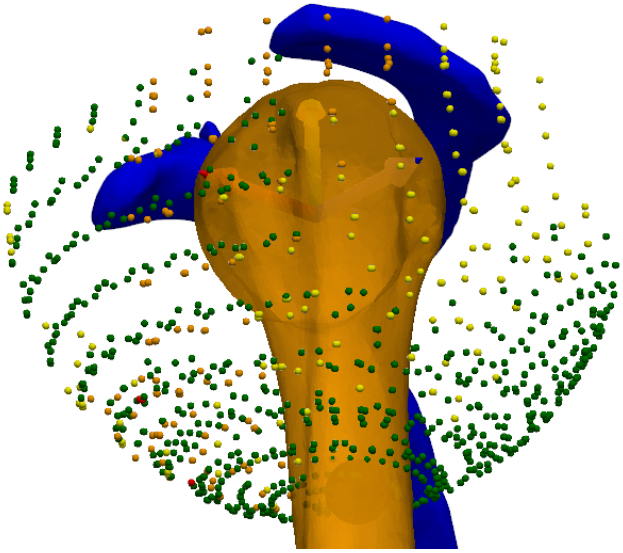

(b) Coraco-humeral distance (CHD) mapping. Red: 8–9.5 mm, orange: 9.5–11 mm, yellow: 11–12.5 mm, green: >12.5 mm.

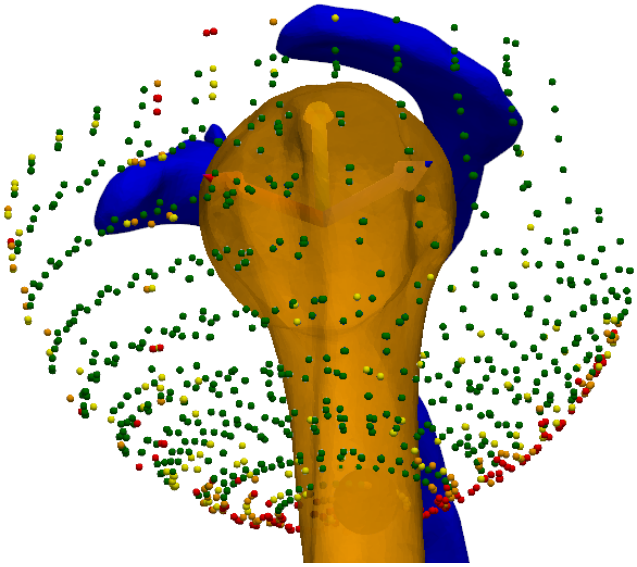

(c) Glenoid coverage mapping. Red: 15–16.5%, orange: 16.5–18%, yellow: 18–19.5%, green: >19.5%.

Figure A.5: Constraint mapping of the solution space for Patient 3. Subfigures show thresholds applied to (a) acromio-humeral distance (AHD), (b) coraco-humeral distance (CHD), and (c) glenoid coverage.

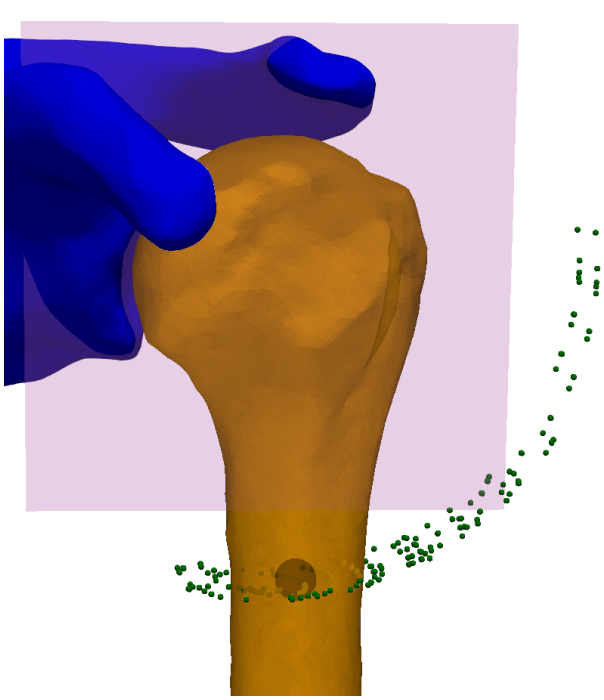

(a) Abduction-adduction solutions

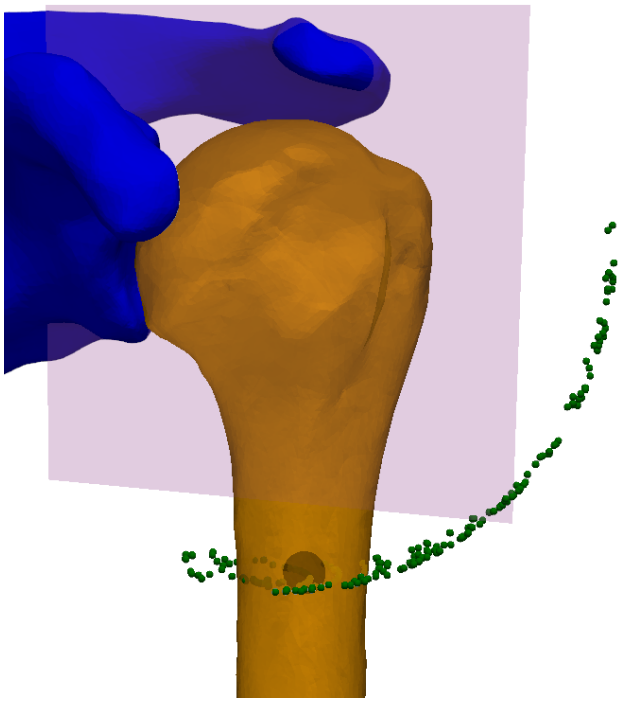

(b) Scapular abduction-adduction solutions

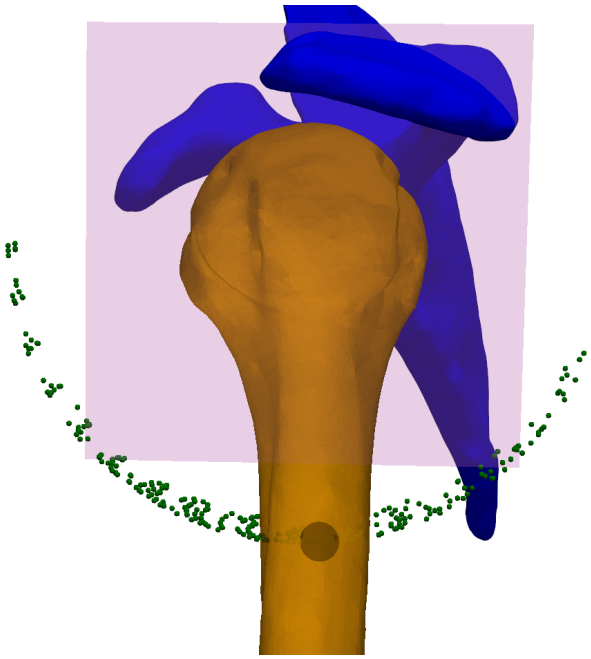

(c) Pure flexion-extension solutions

Figure A.6: Planar motion slices for Patient 3. The purple plane defines the anatomical movement direction. Valid configurations (green) represent achievable positions within the defined slice.

A.3 Patient 4 Results

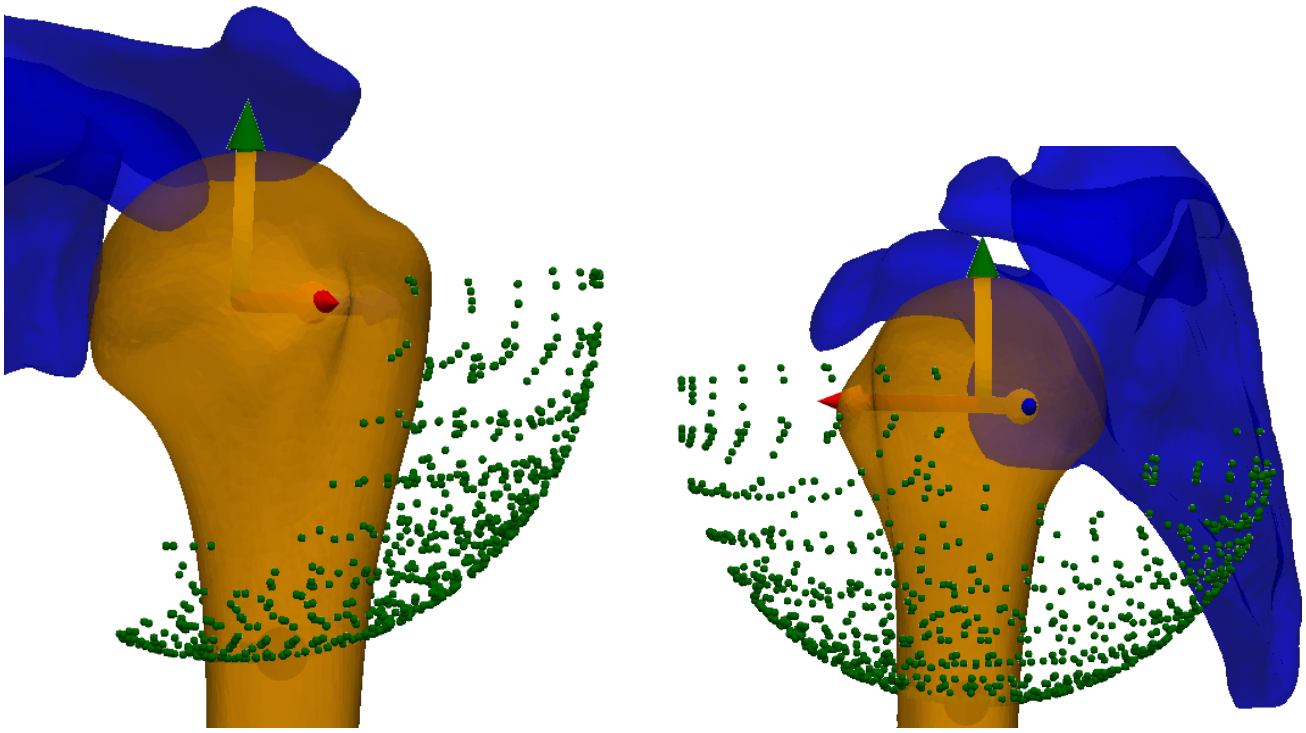

(a) Frontal view

(b) Lateral view

Figure A.7: Solution space with two different views. A black line has been added to highlight key geometric features of the solution envelope. (Patient 4)

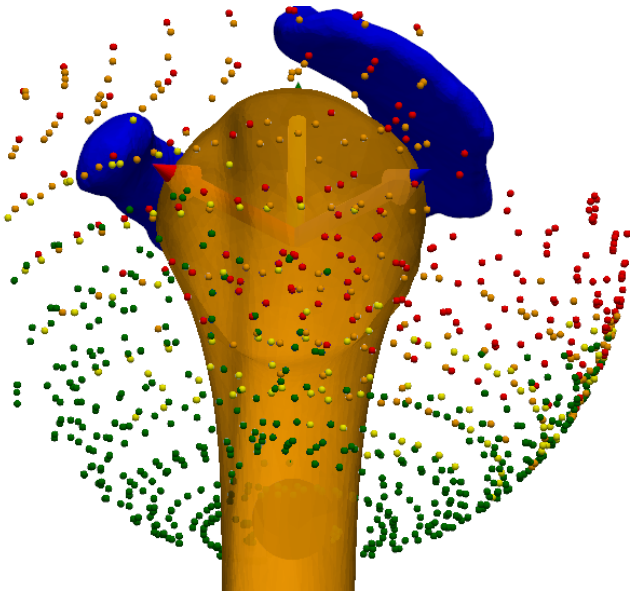

(a) Acromio-humeral distance (AHD) mapping. Red: 4.5–6 mm, orange: 6–7.5 mm, yellow: 7.5–9 mm, green: >9 mm.

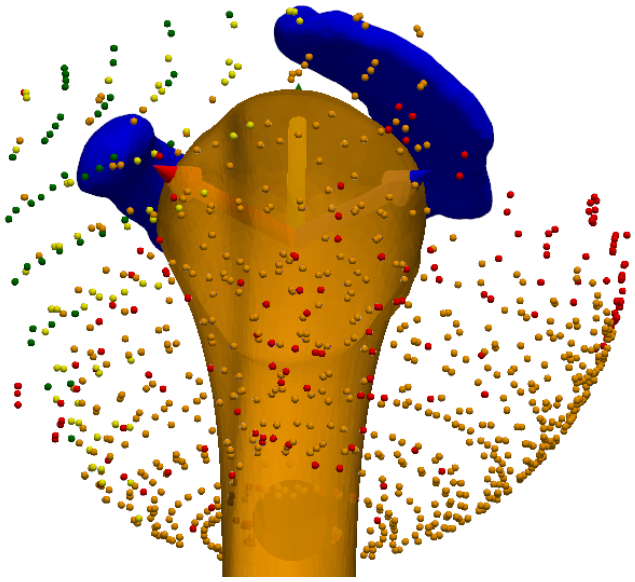

(b) Coraco-humeral distance (CHD) mapping. Red: 7–8.5 mm, orange: 8.5–10 mm, yellow: 10–11.5 mm, green: >11.5 mm.

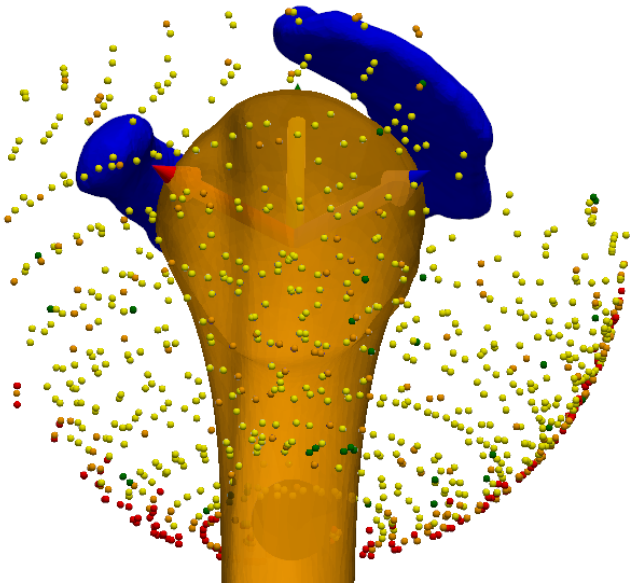

(c) Glenoid coverage mapping. Red: 13.5–15%, orange: 15–16.5%, yellow: 16.5–18%, green: >18%.

Figure A.8: Constraint mapping of the solution space for Patient 4. Subfigures show thresholds applied to (a) acromio-humeral distance (AHD), (b) coraco-humeral distance (CHD), and (c) glenoid coverage.

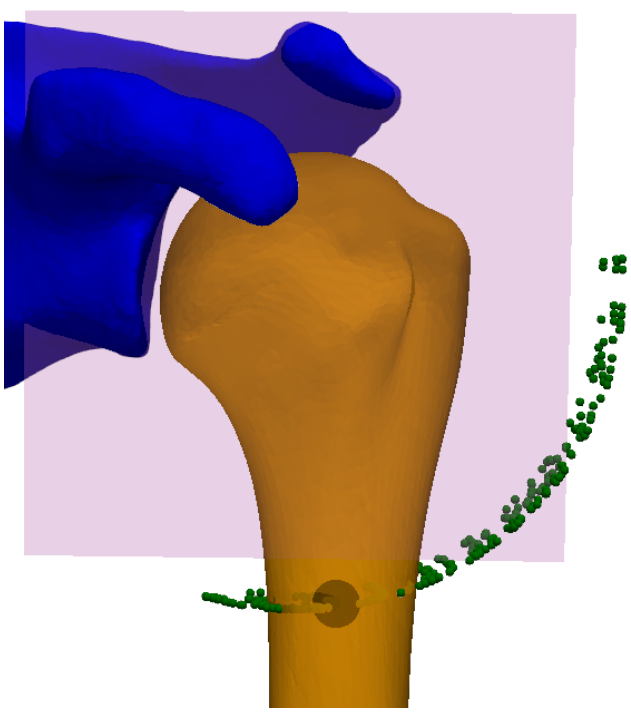

(a) Abduction-adduction solutions

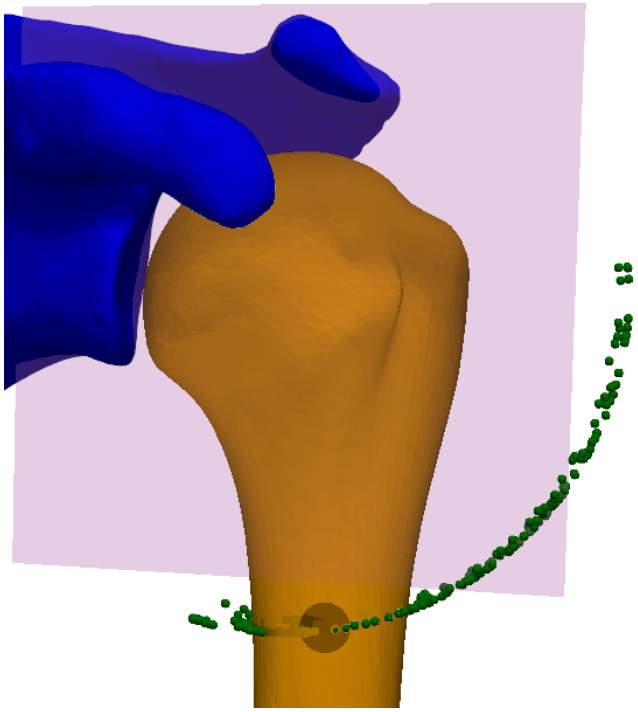

(b) Scapular abduction-adduction solutions

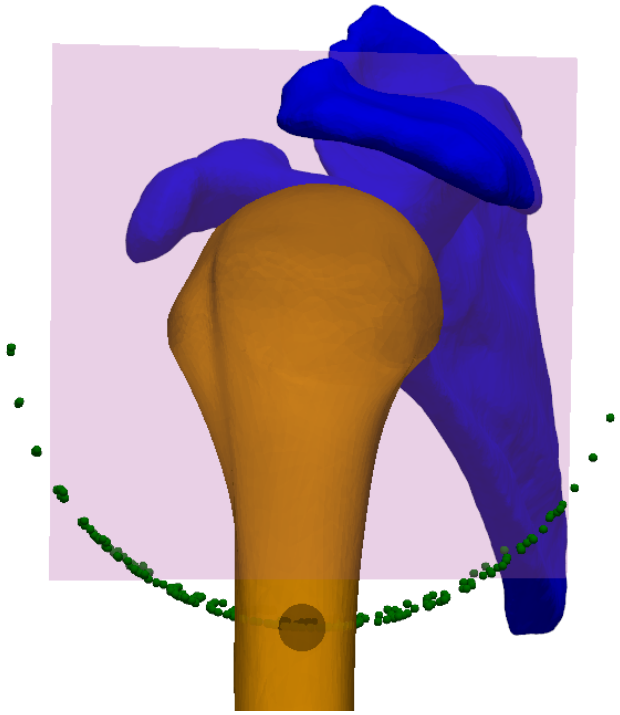

(c) Pure flexion-extension solutions

Figure A.9: Planar motion slices for Patient 4. The purple plane defines the anatomical movement direction. Valid configurations (green) represent achievable positions within the defined slice.

A.4 Patient 5 Results

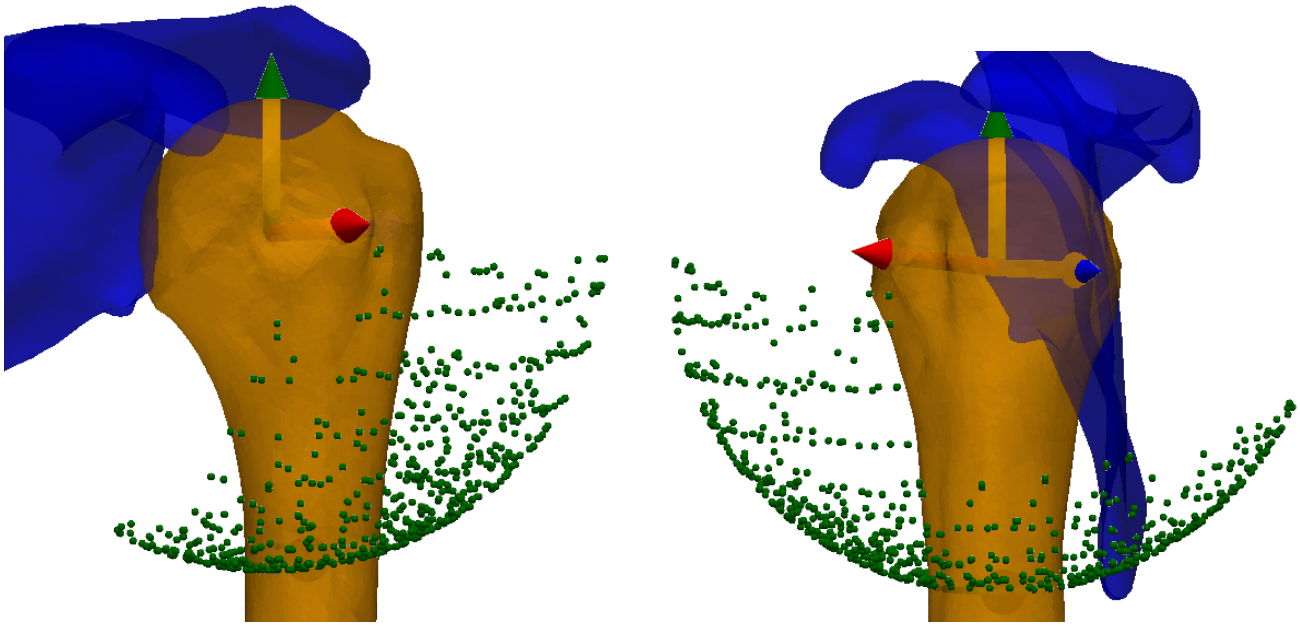

(a) Frontal view

(b) Lateral view

Figure A.10: Solution space with two different views. A black line has been added to highlight key geometric features of the solution envelope. (Patient 5)

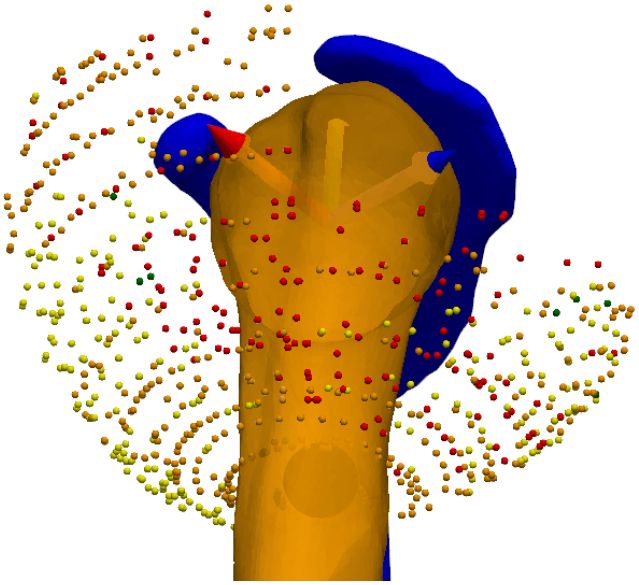

(a) Acromio-humeral distance (AHD) mapping. Red: 4.5–6 mm, orange: 6–7.5 mm, yellow: 7.5–9 mm, green: >9 mm.

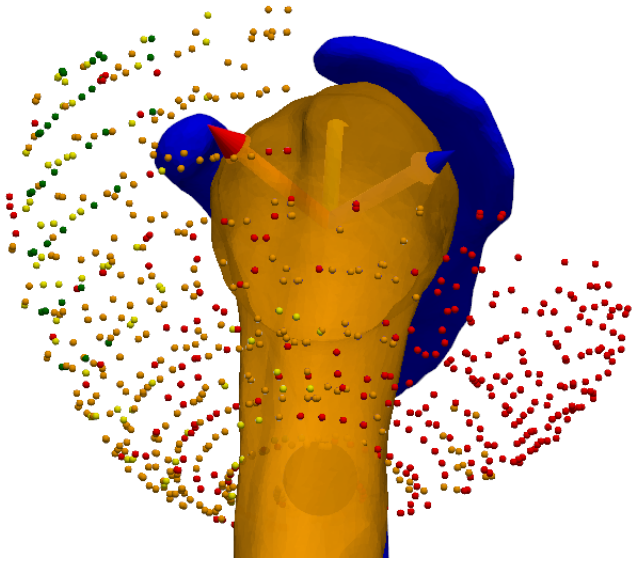

(b) Coraco-humeral distance (CHD) mapping. Red: 7–8.5 mm, orange: 8.5–10 mm, yellow: 10–11.5 mm, green: >11.5 mm.

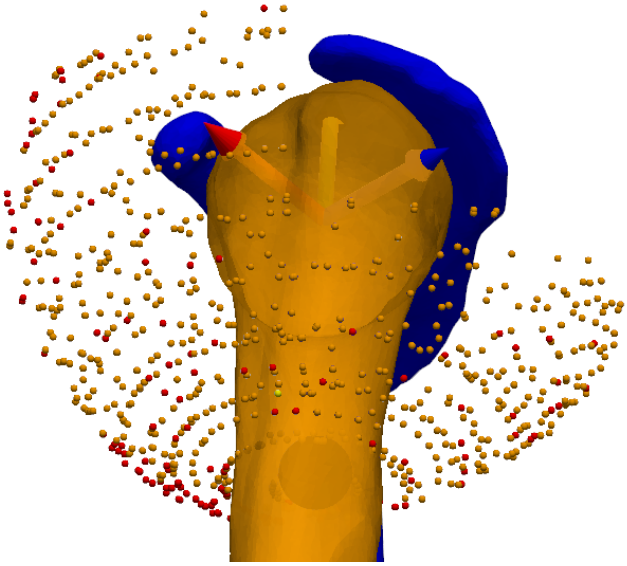

(c) Glenoid coverage mapping. Red: 13.5–15%, orange: 15–16.5%, yellow: 16.5–18%, green: >18%.

Figure A.11: Constraint mapping of the solution space for Patient 5. Subfigures show thresholds applied to (a) acromio-humeral distance (AHD), (b) coraco-humeral distance (CHD), and (c) glenoid coverage.

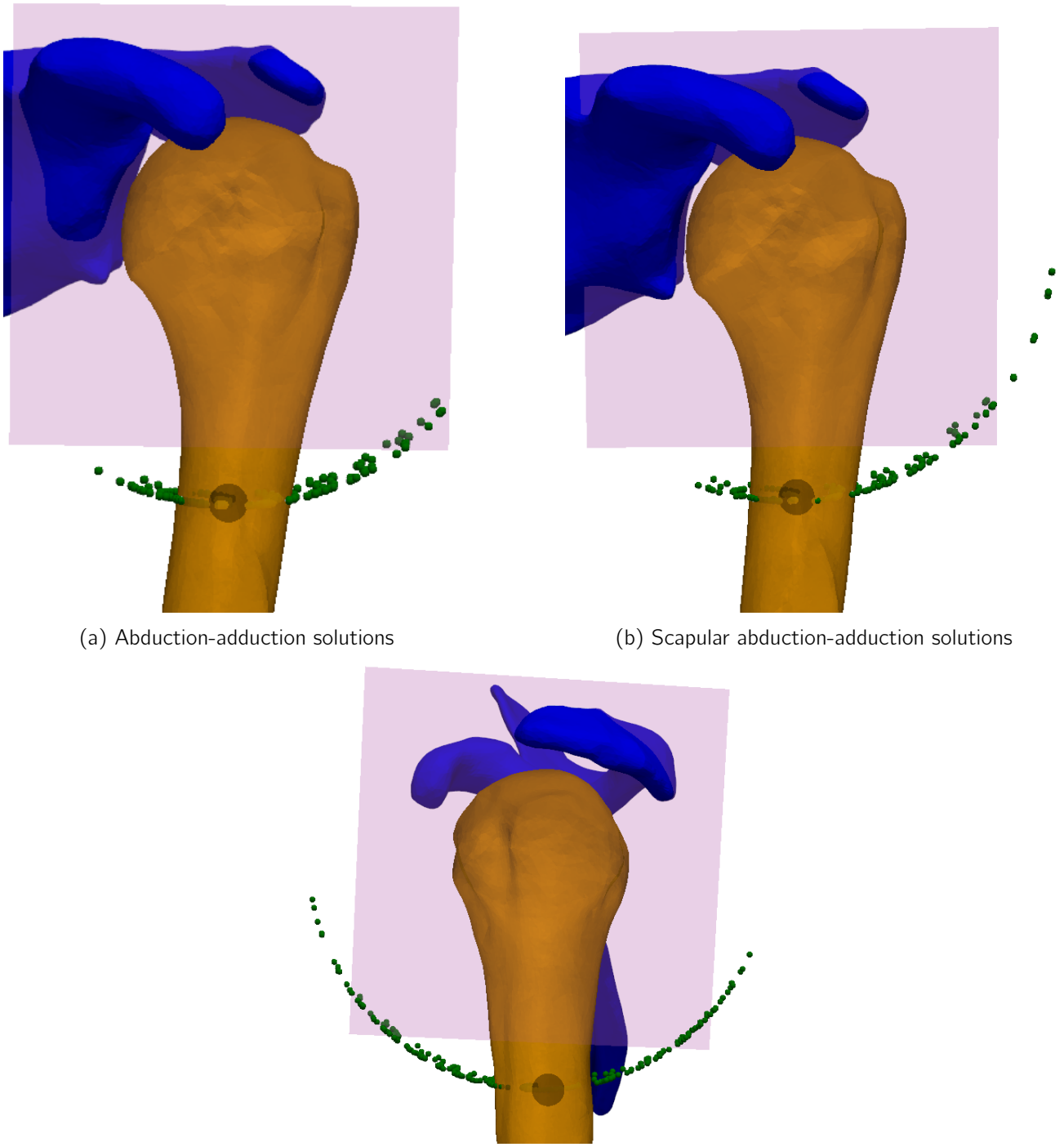

(a) Abduction-adduction solutions

(b) Scapular abduction-adduction solutions

(c) Pure flexion-extension solutions

Figure A.12: Planar motion slices for Patient 5. The purple plane defines the anatomical movement direction. Valid configurations (green) represent achievable positions within the defined slice.

Appendix B

Sex-based Scaling of Humeral Coverage

This appendix provides the mathematical computation to adjust the glenoid coverage constraint based on sex-specific anatomical dimensions. Since average glenoid and humeral head surface areas differ between males and females, a scaling factor is applied to maintain consistent biomechanical interpretation of the coverage ratio. The correction is computed using published anatomical measurements.

Let $\mathcal{G}$ be the glenoid surface area and $\mathcal{H}$ the humeral head surface area. Their respective sex-specific average values are denoted as $\bar{\mathcal{G}}$ and $\bar{\mathcal{H}}$, with the subscripts M and F referring to male and female, respectively.

Glenoid surface area. Assuming an elliptical shape and using values from [26]:

$$\begin{aligned} \bar{\mathcal{G}}_F &= \pi \cdot 23.6 \cdot 32.6 \\ \bar{\mathcal{G}}_M &= \pi \cdot 27.8 \cdot 37.5 \\ \Rightarrow \frac{\bar{\mathcal{G}}_M}{\bar{\mathcal{G}}_F} &= \frac{27.8 \cdot 37.5}{23.6 \cdot 32.6} \approx 1.355 \\ \Rightarrow \bar{\mathcal{G}}_M &\approx 1.36\, \bar{\mathcal{G}}_F \end{aligned}$$

Humeral head surface area. Assuming a spherical shape and using values from [25]:

$$\begin{aligned} \bar{\mathcal{H}}_F &= 4\pi \cdot 20.54^2 \\ \bar{\mathcal{H}}_M &= 4\pi \cdot 22.65^2 \\ \Rightarrow \frac{\bar{\mathcal{H}}_M}{\bar{\mathcal{H}}_F} &= \left(\frac{22.65}{20.54}\right)^2 \approx 1.216 \\ \Rightarrow \bar{\mathcal{H}}_M &\approx 1.22\, \bar{\mathcal{H}}_F \end{aligned}$$

Coverage ratio. Let $\mathcal{C}$ be the glenoid coverage, defined as the ratio $\mathcal{G}/\mathcal{H}$. Then:

$$\mathcal{C}_M = \frac{\bar{\mathcal{G}}_M}{\bar{\mathcal{H}}_M} = \frac{1.36\, \bar{\mathcal{G}}_F}{1.22\, \bar{\mathcal{H}}_F} \approx 1.115 \cdot \mathcal{C}_F$$

Adjusted constraint threshold. Given a threshold of 0.15 for females, the equivalent male threshold becomes:

$$\frac{0.15}{1.115} \approx 0.135$$

Appendix C

Hill-Sachs

This appendix provides additional visualizations related to the engagement analysis of Hill-Sachs defects. For Patients 2, 3, and 5, detailed mappings are shown to illustrate the spatial distribution of joint positions that present engagement during the computed range of motion (ROM). Each case includes two 3D views (one focused on the lesion area and one showing the global engagement envelope) as well as a pie chart summarizing the proportion of configurations falling within defined engagement risk categories.

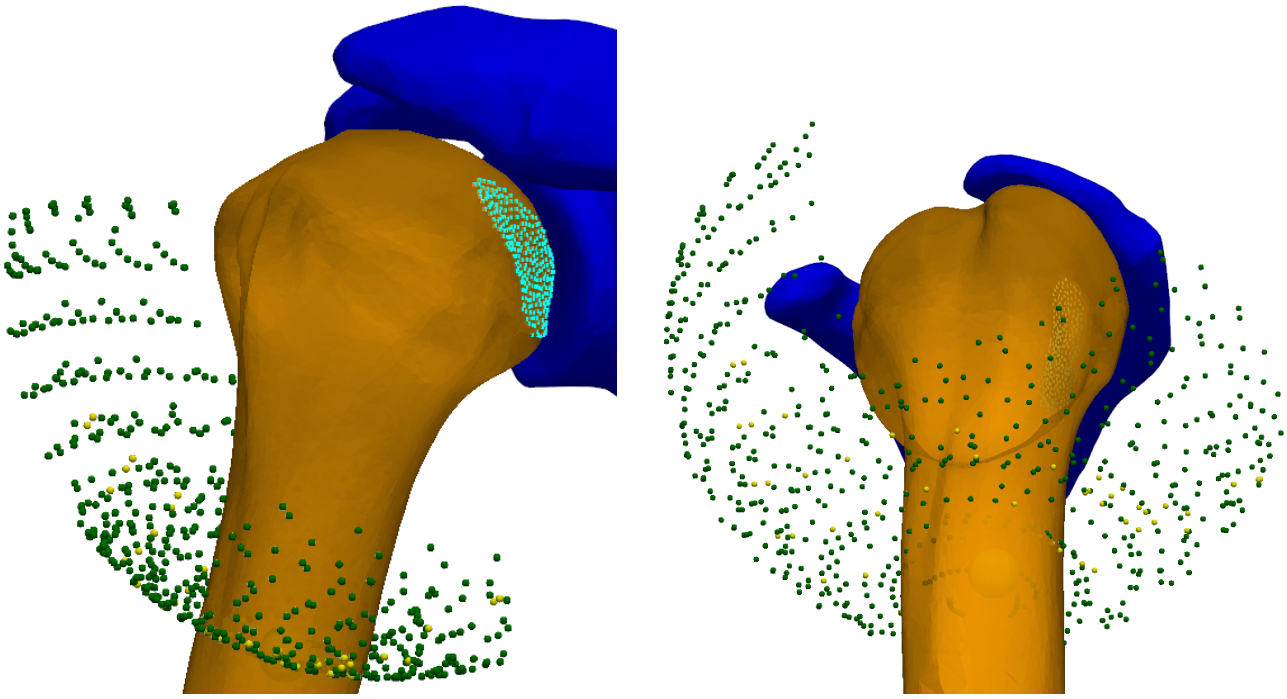

(a) View focused on the defect.

(b) Overview of the full engagement mapping.

Figure C.1: Hill-sachs effect mapping from two perspectives. The Hill-Sachs defect is highlighted in cyan. (Patient 2)

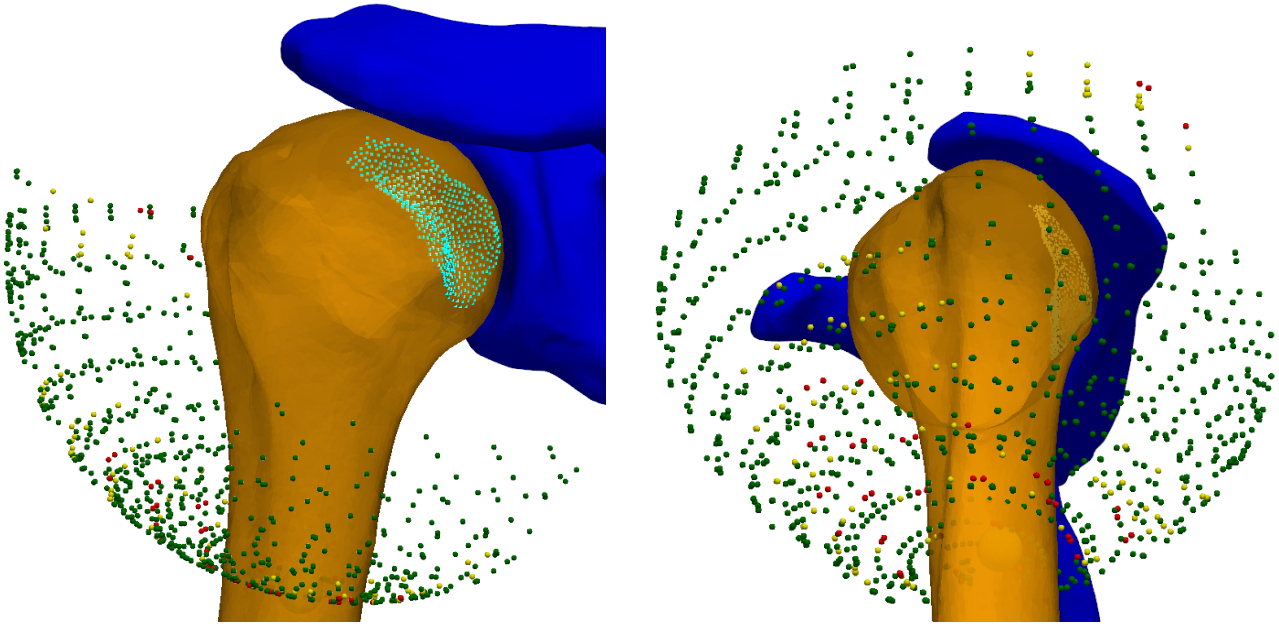

(a) View focused on the defect.

(b) Overview of the full engagement mapping.

Figure C.2: Hill-sachs effect mapping from two perspectives. The Hill-Sachs defect is highlighted in cyan. (Patient 3)

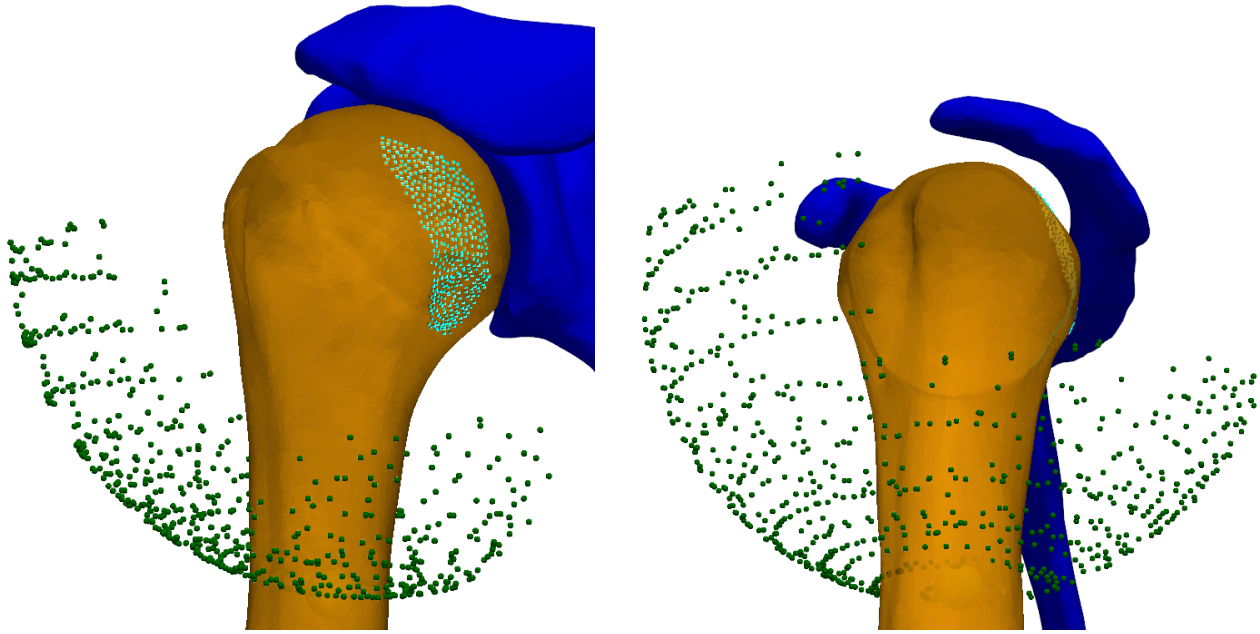

(a) View focused on the defect.

(b) Overview of the full engagement mapping.

Figure C.3: Hill-sachs effect mapping from two perspectives. The Hill-Sachs defect is highlighted in cyan. (Patient 5)

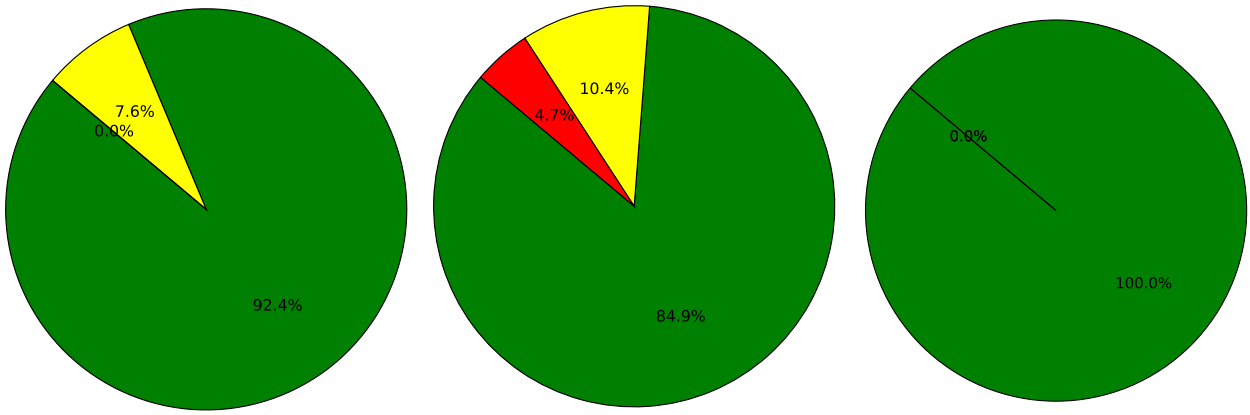

(a) Patient 2 (b) Patient 3 (c) Patient 5

Figure C.4: Distribution of joint positions across HSD risk categories for each patient.

Appendix D

Landmarking Strategies for Acromion and Coracoid

This appendix illustrates the different strategies considered for landmarking the acromion and coracoid processes. Three alternatives are shown for each structure: selection based on surface region, crest region, or representative point sets.

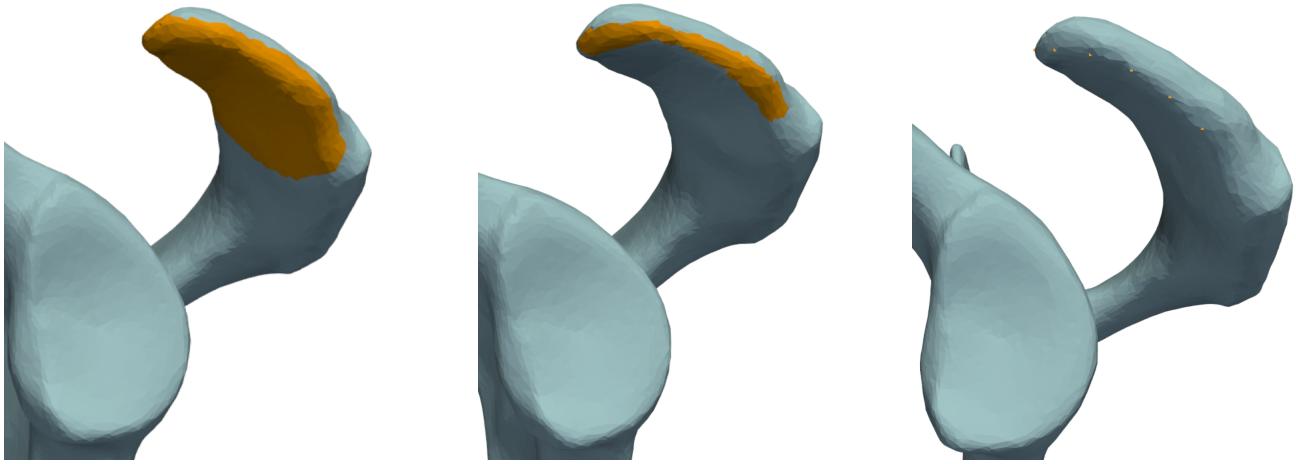

(a) Inferior surface of the acromion

(b) Crest region of the acromion

(c) Representative points

Figure D.1: Three landmarking strategies for the acromion

(a) Posterior surface of the coracoid

(b) Posterior crest of the coracoid

(c) Representative points

Figure D.2: Three landmarking strategies for the coracoid

Appendix E

Collision and Distance Tests Setups

This appendix documents the geometric configurations used to validate the behavior of the collision detection and proximity query components. Simplified mesh setups were constructed, including sphere-to-cube interaction and various cube-to-cube contacts involving faces, edges, and corners. These setups were used to assess the robustness, accuracy, and consistency of the `CollisionManager` and `ProximityQuery` modules under simple conditions.

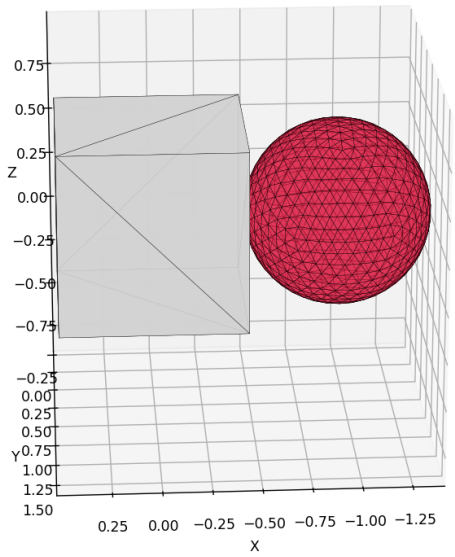

(a) Sphere → Cube

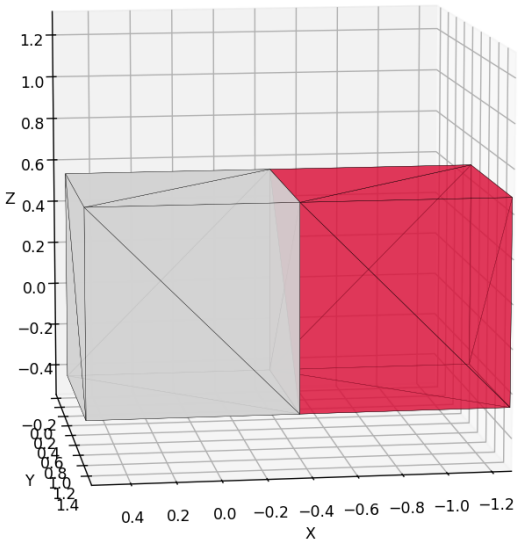

(b) Cube (face) → Cube

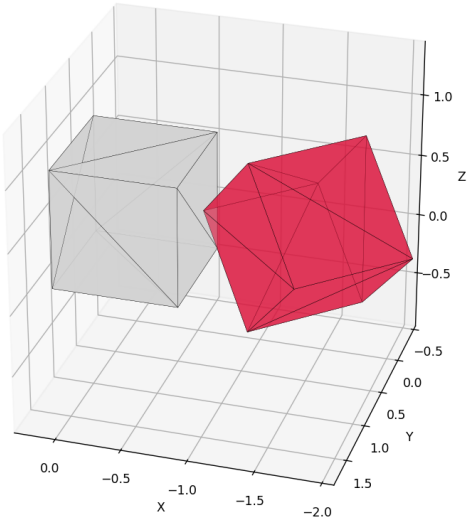

(c) Cube (corner) → Cube

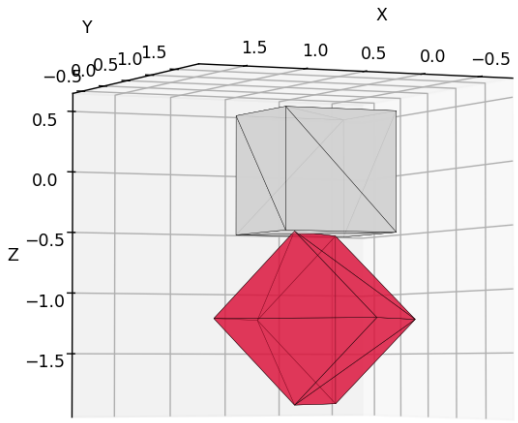

(d) Cube (edge) → Cube

Figure E.1: Meshes setup to test the robustness of the CollisionManager and ProximityQuerry

Appendix F

Use of Artificial Intelligence Tools

Artificial intelligence tools (specifically, OpenAI's ChatGPT and Overleaf's integrated Writefull AI) were used during the redaction of this master thesis for the following purposes:

1. Language verification and text reformulation to improve clarity and fluency of the written content.
2. Assistance with code debugging and generation of plotting scripts to visualize results.

No AI tools were used for the generation of scientific content, data fabrication, or analysis interpretation.